March 2002 • NREL/SR-520-31908

Subcontractor Report

Nanostructure of a-Si:H and Related Alloys by Small-Angle Scattering of Neutrons and X-Rays

Final Technical Progress Report 22 May 1998—15 October 2001

D.L. Williamson
Colorado School of Mines
Golden, Colorado

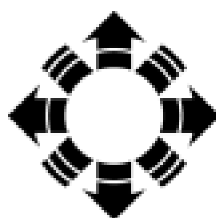

NREL

National Renewable Energy Laboratory

1617 Cole Boulevard
Golden, Colorado 80401-3393

NREL is a U.S. Department of Energy Laboratory
Operated by Midwest Research Institute • Battelle • Bechtel

Contract No. DE-AC36-99-GO10337

March 2002 • NREL/SR-520-31908

Nanostructure of a-Si:H and Related Alloys by Small-Angle Scattering of Neutrons and X-Rays

Final Technical Progress Report
22 May 1998—15 October 2001

D.L. Williamson
Colorado School of Mines
Golden, Colorado

NREL Technical Monitor: Bolko von Roedern

Prepared under Subcontract No. XAK-8-17619-31

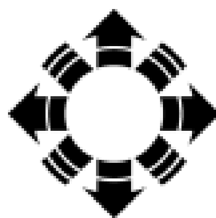

National Renewable Energy Laboratory

1617 Cole Boulevard
Golden, Colorado 80401-3393

NREL is a U.S. Department of Energy Laboratory
Operated by Midwest Research Institute • Battelle • Bechtel

Contract No. DE-AC36-99-GO10337

NOTICE

This report was prepared as an account of work sponsored by the National Renewable Energy Laboratory, a Division of the Midwest Research Institute, in support of its contract number DE-83CH10093 with the United States Department of Energy. Neither the National Renewable Energy Laboratory, the Midwest Research Institute, the United States Government, nor the United States Department of Energy, nor any of their employees, nor any of their contractors, subcontractors, or their employees, makes any warranty, express or implied, or assumes any legal liability or responsibility for the accuracy, completeness or usefulness of any information, apparatus, product or process disclosed or represents that its use would not infringe on privately owned rights.

Available electronically at http://www.osti.gov/bridge

Available for a processing fee to U.S. Department of Energy
and its contractors, in paper, from:
U.S. Department of Energy
Office of Scientific and Technical Information
P.O. Box 62
Oak Ridge, TN 37831-0062
phone: 865.576.8401
fax: 865.576.5728
email: reports@adonis.osti.gov

Available for sale to the public, in paper, from:
U.S. Department of Commerce
National Technical Information Service
5285 Port Royal Road
Springfield, VA 22161
phone: 800.553.6847
fax: 703.605.6900
email: orders@ntis.fedworld.gov
online ordering: http://www.ntis.gov/ordering.htm

Printed on paper containing at least 50% wastepaper, including 20% postconsumer waste

1. EXECUTIVE SUMMARY

1.1 PREFACE

This final report presents results and conclusions of Phases I, II, and III research performed from May 22, 1998 to October 15, 2001 under a cost-reimbursable subcontract from the National Renewable Energy Laboratory (NREL, a national laboratory of the U.S. Department of Energy operated by Midwest Research Institute) to the Colorado School of Mines (subcontract number XAK-8-17619-31 to the prime contract DE-AC36-83CH10093). Due to a contract extension, this report covers the above period of more than three calendar years. The research was carried out under the direction of Don L. Williamson, Professor of Physics. Materials characterization, including small-angle x-ray scattering and x-ray diffraction, was carried out in the Physics Department of the Colorado School of Mines (CSM). In addition, small-angle neutron scattering (SANS) was carried out at the NIST Center for Neutron Research and anomalous small-angle x-ray scattering (ASAXS) was performed by a collaborator (G. Goerigk) at the German synchrotron, DESY. The materials for analyses were supplied by NREL-supported device-making groups as well as by other groups with relevant expertise. The co-P.I., David W.M. Marr, of the Chemical Engineering Department of CSM, contributed to the research project via assistance in the design, execution, and analysis of the SANS experiments at NIST. Graduate students T. Abdel-Monem and D. Charters contributed to the research effort in the x-ray lab at CSM. Various complementary measurements on many of the samples were made at NREL: H. Moutinho - AFM measurements; J. Webb, L. Gedvillas, and B. Keyes - IR measurements; A. Swartzlander-Guest and B. To – EPMA measurements.

1.2 OBJECTIVES/APPROACH

The general objective of this research was to provide detailed microstructural information on the amorphous-silicon-based, thin-film materials under development for improved multijunction solar cells. Correlation of this microstructure with opto-electronic properties and device performance was an integral part of the research. The principal experimental techniques used were small-angle x-ray scattering (SAXS), small-angle neutron scattering (SANS), and conventional x-ray diffraction (XRD). These provide quantitative microstructural data on microvoid fractions, sizes, shapes, preferred orientations, H non-uniformity and clustering, Ge non-uniformity and clustering, microcrystallinity, and medium-range order. An important task was to establish whether

SANS can be used to determine the hydrogen nanostructure and any changes that might occur due to light soaking. Some experiments were conducted using anomalous SAXS (ASAXS) via special facilities in Germany. This method provides information on the Ge uniformity and nanostructure in a-SiGe:H alloys. Several types of material have been investigated in collaboration with the NREL National Team devoted to amorphous silicon solar cell research and development.

1.3 CONCLUSIONS

1.3.1 SANS Studies

a. We have established that statistically significant SANS data can be obtained from device-quality films that are only 1 or 2 µm thick. These data were enabled by the special high-flux neutron beam facility at NIST and by careful sample preparation on high-quality c-Si substrates that were then stacked in multiple layers for the SANS measurements.

b. Four samples were examined in a light-soaked state (AM1, 300 h) and then re-examined after annealing (190°C, 1 h) *in-situ* to look for any change in SANS associated with the Staebler-Wronski effect. The films were deposited by two techniques, plasma-enhanced chemical-vapor deposition (PECVD) and hot-wire chemical-vapor deposition (HWCVD) using conditions that yield high-quality films and devices. No changes were observed in the SANS intensity to a precision that could have readily detected the 25% change reported in 1985 (Chenevas-Paule *et al*).

c. Significant differences are observed in hydrogenated and deuterated films, as well as in the PECVD versus the HWCVD materials. The SANS results for the HWCVD material, when complemented with the SAXS results, can be explained with a 3-phase model that is consistent with NMR evidence of H-rich and H-poor domains, as well an nanovoids, in this type of a-Si:H. The PECVD SANS can be explained by a 3-phase model of small H-rich clusters or H-containing nanovoids in a uniform matrix and a surface roughness contribution.

d. The alloy materials a-$Si_{1-x}Ge_x$:H and a-$Si_{1-x}C_x$:H have been studied for the first time by SANS and, consistent with the prior SAXS results, strong scattering is observed, further confirming the significantly enhanced heterogeneity of these alloys compared to the a-Si:H.

e. The ultra-high-deposition-rate HWCVD material made with and without H dilution yields strong SANS signals, consistent with the high nanovoid fraction indicated by the SAXS results.

f. "Polymorphous" Si:H and Si:H/D films have been examined by SANS and found to have strong heterogeneity in the H distribution. The size-scale of this heterogeneity is dominated by much larger size features than those found in the PECVD and HWCVD materials.

[All the above SANS research was a enabled by collaborations with NIST, NREL, USSC, BP-Solar, and Ecole Polytechnique]

1.3.2 Medium Range Order and Microcrystallinity Studies

a. High-hydrogen-diluted films of a-Si:H, 0.5 μm in thickness and optimized for solar cell efficiency and stability, are found to be partially microcrystalline (μc) if deposited directly on stainless steel (SS) substrates but are fully amorphous if a thin n layer of a-Si:H or μc-Si:H is first deposited on the SS. Partial microcrystallinity develops as such films are grown thicker (1.5-2.5 μm) and this is accompanied by sharp drops in V_{oc}. For the fully amorphous films, x-ray diffraction (XRD) shows improved medium range order (MRO) compared to undiluted films and this correlates with better light stability. Capacitance profiling shows a decrease in deep defect density as growth proceeds further from the substrate, consistent with the XRD evidence of improved order for thicker films. XRD also shows a wide range of MRO exists in the residual amorphous phase of the mixed a/μc material. [collaboration with USSC, U. Oregon, and NREL]

b. There is no detectable change in the nanostructure nor the appearance of microcrystallinity in a-SiGe:H solar-grade material as the thickness is increased from 0.2 to 1.3 μm based on a carefully designed multilayer sample. [collaboration with ECD]

c. The first known XRD studies of protocrystalline ("on-the-edge") SiGe:H in SS/nip solar cells (1500 Å i-layers) provide understanding of the sharp V_{oc} drop with increasing H_2-dilution on the basis of small amounts of microcrystallinity. The Ge composition of the microcrystals matches the average film Ge composition demonstrating no preferential formation of Si-rich or Ge-rich microcrystals. [collaboration with USSC]

d. USSC has discovered a light-induced change in V_{oc} of solar cells with an intrinsic layer made of the mixed amorphous/microcrystalline phase. The V_{oc} is significantly *increased* upon light soaking (Lord, Yan, Yang, Guha, preprint, submitted to APL). A careful search by XRD of one sample has not detected any change in the degree of crystallinity. [collaboration with USSC]

e. PECVD films prepared by USSC under different H dilution conditions have been examined by IR, XRD, and H evolution. The high-H-dilution material is deemed "on-the-edge"

material because of its observed tendency to be near the boundary between amorphous and microcrystalline states. Upon annealing, a low temperature H-evolution peak appears, and film crystallization is observed at temperatures as low as 500°C, which is far below that observed for a-Si:H films grown without H dilution. Although not detected directly by XRD in the as-grown state, very small crystallites are postulated that catalyze the low-temperature crystallization of the films upon annealing. The large spatial inhomogeneity in the H bonding associated with the very small crystallites is suggested to be one of the reasons for the reduced Staebler-Wronski effect observed in solar cells utilizing the "on-the-edge" material. [collaboration with NREL and USSC].

f. Thin film n-i-p solar cells were prepared by USSC using decomposition of disilane-hydrogen mixtures by plasma-enhanced chemical vapor deposition. By increasing either the H dilution ratio or the thickness, the i-layer structure showed a transition from amorphous to microcrystalline silicon characterized by x-ray diffraction at CSM. The electronic states of the i-layer were examined by photoluminescence (PL) spectroscopy at UNC, which showed that: (a) below the onset of microcrystallinity, a blue-shift of the 1.4 eV PL peak energy along with a decrease of the band width occur as the structural order is improved; (b) above the onset of microcrystallinity, the PL efficiency decreases by a factor of 4-5 and the PL peak energy is red-shifted toward 1.2 eV as the μc-Si volume fraction is increased. In addition, the solar cell open circuit voltage shows first an increase and then a decrease, correlating with the PL peak energy position. We conclude that the PL spectroscopy, coupled with XRD, is a sensitive tool for characterizing the gradual amorphous-to-microcrystalline structural transition in thin film solar cells. [collaboration with UNC and USSC]

g. BP-Solar supplied films of their latest device-quality a-$Si_{1-x}Ge_x$:H materials (x= 0 to 0.44) for study by SAXS and XRD. The SAXS shows nanostructures typical of such alloys, increasing strongly with Ge additions. The x=0 material has a somewhat larger volume fraction (0.05%) of nanostructural features than the best PECVD materials prepared by USSC (0.01%). The medium-range order shows a slight decrease with added Ge and all the films show reduced order compared to the best-quality PECVD and HWCVD films prepared by other groups. [collaboration with BP-Solar]

h. Microcrystalline materials prepared by different groups using different methods have been analyzed SAXS and all show extremely heterogeneous nanostructure, probably associated

with low density, H-rich material forming between the dense microcrystals. [collaborations with ECD, Hahn-Meitner Institute, and U. Stuttgart]

1.3.3 RF-PECVD versus VHF-PECVD Comparison at Higher Deposition Rates

A study has been made of the structural, optical and electrical properties of films prepared by ECD at various deposition rates between 1 and 15 Å/s using rf frequencies of 13.56 and 70 MHz. The films were characterized using a number of techniques including SAXS, infrared absorption spectroscopy, and scanning electron microscopy. For the films made using the 70 MHz frequency, the amount of nanovoids with sizes of < 100Å increases systematically as the deposition rate increases beyond 5 Å/s. Accompanying the increase in void fraction in the films are increases in the hydrogen content and the amount of 2070 cm^{-1} mode in the infrared absorption spectra. In addition to an increase in the amount of nanovoids in the films as the deposition rate exceeds 5 Å/s, the films made using the 13.56 MHz and high deposition rates have larger amounts of SAXS related to scattering features with sizes > 200 Å. This scattering is associated with large bulk density fluctuations and/or enhanced surface roughness. None of the films in the study displayed signs of having columnar-like microstructures. The nanovoids are not related to changes in the solar cells with increasing i-layer deposition rate for both fabrication processes, perhaps due to the relatively small volume fractions of less than 0.2% and/or good void-surface passivation. However, the larger-scale structures detected in the films made using the 13.56 MHz technique could cause the observed poorer performance in cells prepared at high growth rates. [collaboration with ECD]

1.3.4 HWCVD a-Si:H Studies

a. SAXS studies of the films grown at NREL in the HWCVD tube reactor reveal a significant increase in the nanovoid volume fraction when altering the deposition conditions to reach the ultra-high deposition rates of up to 1 μm/min. There is a sharp transition in the heterogeneity as the deposition rate is increased above about 2 nm/s as seen by an increase in integrated SAXS of about two orders-of-magnitude, corresponding to about 1-2 vol.% voids. This increased SAXS is independent of deposition rate from about 3 to 13 nm/s. Similarly, x-ray diffraction studies of the medium-range order show no variation in order over this same rate change. The order is not as good as detected in the best quality PECVD and HWCVD films reported earlier. Reasons are proposed to explain why the increase in microvoid density apparently

does not play a role in the Staebler-Wronski effect for this type of material. [collaboration with NREL]

b. A large difference is seen in the nanostructure of PECVD and HWCVD films prepared by MVSystems. The HWCVD sample is dominated by larger scale (>10 nm) structure while the PECVD sample shows only small scale structure (~1 nm). Both have low void contents near 0.1 vol.%. [collaboration with MVSystems]

c. At the request of the UCLA group, two SAXS samples were supplied for a high pressure experiment: NREL-HWCVD a-Si:H films on 10 micron Al foil, folded into 8 layers;

T840 - low substrate temperature, relatively high void fraction (about 2 vol.%)

T905 - high substrate temperature, very low void fraction (about 0.02 vol.%)

A SAXS-reference Al-substrate foil was included in the high pressure treatment of the above samples. Careful SAXS measurements after the high-pressure treatment at 3 kbar show that there is no evidence for a residual microvoid collapse. [collaboration with UCLA]

1.3.5 ASAXS Studies

a. From extended anomalous-SAXS (ASAXS) measurements at numerous x-ray energies, structural and physical properties such as non-uniform Ge-concentrations and – in combination with flotation density results – the densities of Ge-enriched regions in amorphous a-$Si_{1-x}Ge_x$:H alloys were deduced based on a two-phase model. Depending on the preparation technique (with and without H dilution of the source gases), a dense phase with volume fractions of about 90% and with Ge-enrichments only slightly higher with respect to the entire alloy were observed. These denser regions with average sizes between 10 and 23 nm can be interpreted as a phase containing slightly enhanced numbers of homopolar Ge-bonds, surrounded by a small volume fraction phase of low density, H-rich regions containing much less Ge (sometimes none) with averages sizes from 0.6 to 1.6 nm. [collaboration with Forschungszentrum Jülich, Germany]

b. Both HWCVD and PECVD a-$Si_{1-x}Ge_x$:H alloys have been examined and compared by ASAXS to reveal a systematic increase in Ge inhomogeneities with increasing x and to demonstrate the HWCVD material to be more heterogeneous than the PECVD material for a given x. The scale over which the Ge composition fluctuations occur is about 1 nm for these films. A comparison with SAXS data from the same films shows that 30 to 50% of the inhomogeneity is caused by the Ge

composition fluctuations, the balance likely due to microvoids and surface roughness. [collaboration with NREL, USSC, and Forschungszentrum Jülich, Germany]

c. A novel method to search for the Ge inhomogeneity has been attempted. Films were annealed to crystallization and then examined by XRD to search for evidence of different lattice parameters associated with crystals of different composition. For several films, two distinct phases of c-$Si_{1-x}Ge_x$ (Si-rich and Ge-rich) have been observed, but this is attributed to a metallurgical reaction with the Al-foil substrate, details of which are still under study. One film on c-Si substrate showed no such evidence of two phases after crystallization.

1.3.6 Polymorphous Si:H

a. We have completed SAXS measurements from a series of a-Si:H samples that are designated as "polymorphous" to describe a new type of a-Si:H prepared by P. Cabarrocas of the Ecole Polytechnique. The SAXS due to any nanostructural features (< 10 nm) is extremely weak. Three samples show an integrated SAXS only slightly larger than the detection limit corresponding to 0.01 vol.% voids. Thus, it is very interesting that there is little or no x-ray scattering from the "polymorphous" nature of these films. This may be due to a very small electron density contrast between the incorporated nanocrystals that are seen by TEM and the amorphous matrix, and/or due to a very small volume fraction of such nanocrystals (however, Cabarrocas has pointed out that he expects the films to have large volume fractions). XRD on all the polymorphous samples did not detect any evidence of crystalline Si (111), (220), or (311) peaks. It is likely that the material may be “protocrytstalline”, at least for material yielding a high V_{oc}. [collaboration with Ecole Polytechnique, Paris]

b. As noted above, SANS measurements have been completed on polymorphous-Si:H and –Si:H/D samples and compared with that from “standard” PECVD a-Si:H. Strong SANS signals from the polymorphous material compared to the standard a-Si:H and a change upon D substitution can be interpreted as due to a highly inhomogeneous H distribution in the polymorphous material. [collaboration with Ecole Polytechnique, Paris]

1.3.7 PECVD a-Si:H Prepared with Ar dilution

A systematic set of films prepared by PECVD under different amounts of Ar dilution and with different plasma powers has been studied by SAXS and XRD. The formation of

microcrystalline material and increases in void fractions can be clearly correlated with the deposition conditions and the behavior is similar to that with H dilution. The results can be explained on the basis of bombardment of the growth surface by excited Ar atoms from the plasma. [collaboration with IACS, India]

Table of Contents

1. Executive Summary i
    1.1 Preface i
    1.2 Objectives/Approach i
    1.3 Conclusions ii

List of Figures x
List of Tables xi

2. Introduction. 1

3. Results and Discussion 2
    3.1 SANS Experiments and Analyses 2
    3.2 Medium Range Order and Microcrystallinity 28
    3.3 RF-PECVD versus VHF-PECVD Comparison at Higher Deposition Rates 42
    3.4 HWCVD a-Si:H studies 43
    3.5 ASAXS Experiments and Analyses 49
    3.6 Polymorphous Si:H 54
    3.7 PECVD a-Si: Prepared with Ar Dilution 57

4. References 62

List of Figures

Fig. 1. SANS data comparison for PECVD vs HWCVD a-Si:H 9

Fig. 2. SANS data from hydrogenated vs deuterated HWCVD 10

Fig. 3. Comparison of SANS data from H/D pairs of a-Si:H/D and a-SiGe:H/D alloys 11

Fig. 4. SANS from a-SiC:H alloy compared to that from a-Si:H 12

Fig. 5. SANS from polymorphous Si:H/D (PH2 and PD2) and standard a-Si:H (PH1). 13

Fig. 6. Fit of Eq. 1 to the SANS data from a HWCVD a-Si:H film 15

Fig. 7. Fit of Eq. 1 to SANS data from a HWCVD a-SiGe:H alloy 16

Fig. 8. Fit of SANS data from a HWCVD a-Si:H made at ultra-high deposition rate 17

Fig. 9. Fit to SANS data from PECVD a-Si:H 18

Fig. 10. Fit of SANS data from PECVD a-SiGe:D film 19

Fig. 11. Fit of SANS data from PECVD a-Si:H grown with disilane 20

Fig. 12. Experimental values of the incoherent background scattering intensity 22

Fig. 13. AFM image of UH1 (PECVD a-Si:H) 24

Fig. 14. AFM surface roughness distribution of UH1 (PECVD a-Si:H) 24

Fig. 15. AFM image of HWCVD a-Si:H (NH1) 25

Fig. 16. AFM surface roughness distribution of NH1 25

Fig. 17. SAXS data from ECD films and corresponding size distributions XRD. 30

Fig. 18. XRD patterns from USSC ss/nip cell layers with SiGe:H i-layers 32

Fig. 19. a.Band gap and V_{oc} versus Ge content; b. Correlation of V_{oc} with μc-fraction 32

Fig. 20. XRD results from USSC ss/nip cell material in annealed and light-soaked states 34

Fig. 21. SAXS data for a-$Si_{1-x}Ge_x$:H alloy films from BP-Solar 36

Fig. 22. Survey of integrated SAXS results for a-$Si_{1-x}Ge_x$:H alloys. 37

Fig. 23. XRD patterns from BP-Solar a-$Si_{1-x}Ge_x$:H films on (111) c-Si 39

Fig. 24. XRD linewidths of BP-Solar a-$Si_{1-x}Ge_x$:H films on (111) c-Si 39

Fig. 25. SAXS data from ECD gas-jet microcrystalline films made under different gas flows . . 40

Fig. 26. Typical SAXS data from HWCVD films made at low and ultra-high deposition rates . 44

Fig. 27. Summary of the integrated SAXS from nanostuctural features of HWCVD a-Si:H. . . .45

Fig. 28. Summary of average radii obtained from fits to HWCVD a-Si:H SAXS data 45

Fig. 29. SAXS from MVSystems films made by PECVD and HWCVD 46

Fig. 30. SAXS data before and after a 3 kbar high-pressure treatment on two HWCVD films. . .48
Fig. 31. Comparison of SAXS and ASAXS integrated intensities from several alloys 50
Fig. 32. XRD patterns from HWCVD a-SiGe:H alloy before and after crystallization 52
Fig. 33. SAXS data from Ecole-Polytechnique polymorphous (pm)-Si:H. 54
Fig. 34. Tilting data from a polymorphous Si:H film on Al-foil 55
Fig. 35. SAXS from pm-Si:H co-deposited on Al-foil and c-Si 56
Fig. 36. SAXS from a-Si:H prepared at 95% Ar dilution at different plasma powers 59
Fig. 37. SAXS from a-Si:H films prepared with 90% Ar dilution at different plasma powers . . 59
Fig. 38. Comparison of SAXS from Si:H prepared at different Ar dilutions 60
Fig. 39. XRD patterns from several Si:H films prepared by Ar-dilution 60

List of Tables

Table I. List of all SANS samples and their ID numbers 4
Table II. Compositions of SANS samples and actual thicknesses 7
Table III. Quantitative SANS results from all samples 21
Table IV. SAXS results from companions to SANS samples 23
Table V. SAXS results for ECD a-$Si_{1-x}Ge_x$:H films 29
Table VI. V_{oc} and composition of a/μc-$Si_{1-x}Ge_x$:H 31
Table VII. Quantitative SAXS and IR results from BP-Solar films. 38
Table VIII. Quantitative SAXS results from ECD gas-jet μc-Si:H 41
Table IX. Quantitative SAXS results from IPE HWCVD μc-Si:H 41
Table X. SAXS results from MVSystems samples 47
Table XI. a-$Si_{1-x}Ge_x$:H samples for crystallization/XRD study 51
Table XII. Flotation densities of polymorphous, standard, and partially μc Si:H 57
Table XIII. Deposition conditions for IACS Samples 58
Table XIV. Quantitative SAXS and XRD results from Ar-diluted a-Si:H 61

2. INTRODUCTION

Numerous experiments have been completed during this research project in collaboration with NREL and NREL-supported groups, as well as with other groups having expertise in the field of amorphous and microcrystalline silicon-based solar-cell materials. The primary effort has been with the specialized SANS technique through experimental data collection at the NIST Center for Neutron Research in Gaithersburg, Maryland during three days of beam time awarded to us in August 1999 and three days in November, 2000, followed by extensive data reduction, analyses and interpretation. The first section below summarizes these results and analyses and documents the good quality SANS data from device-quality films. Several SAXS measurements were made on companion samples to aid in the SANS interpretation. Of particular help in the SANS interpretation were the IR results on the H and D contents in the SANS samples. Some AFM studies also provided relevant information on the surface roughness. The second section describes the extensive experiments on the evidence for increased order and the transition to microcrystallinity as the H dilution or the film thickness is increased. Also included in this section are SAXS results from microcrystalline materials prepared by various techniques. The third section summarizes systematic SAXS studies of RF-PECVD and VHF-PECVD a-Si:H materials prepared in the quest for higher-than-normal deposition rates. Many samples of HWCVD a-Si:H were studied, particularly a set grown at ultra-high deposition rates up to more than 10 nm/s and these studies are described in section four. Clear evidence for Ge non-uniformity based on the specialized ASAXS technique is presented in section five. Included there is our recent attempt to search for this non-uniformity by a novel crystallization method. The last two sections presents results from materials made by alternate deposition techniques: “polymorphous”-Si:H, and Ar-diluted plasma deposition of a-Si:H.

To present all the experiments, results, and interpretation in a concise yet complete manner, the following approach will be used: studies already presented in the open literature will be only be briefly described (and the appropriate references cited) while any studies not yet published will be described in some detail.

3. RESULTS AND DISCUSSION

3.1 SANS Experiments and Analyses

3.1.1 Introduction

It has long been clear that hydrogenated amorphous silicon (a-Si:H) and related alloys such as a-SiGe:H and a-SiC:H are heterogeneous on the micrometer and nanometer length scales. This information has come from many techniques including electron microscopies, x-ray and neutron diffraction and scattering, scanning-probe microscopies, and nuclear magnetic resonance. The degree of heterogeneity depends strongly on the deposition methods and detailed conditions, and generally one is striving to eliminate, minimize, or control any non-uniformity in the quest for the optimum material for a given application. Our work has focused mainly on x-ray methods in the recent past to study a wide range of a-Si:H-based materials, with particular emphasis on solar-cell-quality material. These studies utilize small-angle x-ray scattering (SAXS) to look for electron density fluctuations [1,2] and x-ray diffraction (XRD) to examine medium-range order and microcrystallinity [3,4]. Due to the controlling influence of hydrogen in this class of materials, techniques which provide special sensitivity to the hydrogen are particularly valuable. Due to the much larger relative cross-section for scattering of neutrons vis-à-vis x-rays from hydrogen atoms, small-angle neutron scattering (SANS) should be much more sensitive to the hydrogen distribution than SAXS. However, only a few experimental SANS studies of a-Si:H have been reported [5-10], primarily due to needs for rather thick samples and special facilities. Also, weak to non-detectable signals were reported for the best quality films [5]. Recent demonstrations of good quality SANS data from very thin polymer films using signal-to-noise-enhancing conditions at the NIST Center for Neutron Research (NCNR) [11,12] encouraged us to attempt new experiments with high-quality a-Si:H. The possibility of separating out the signals due specifically to the hydrogen heterogeneity (from that due, e.g., to microvoids or surface roughness) and reducing the inherently strong incoherent background scattering due to hydrogen is allowed by substituting deuterium for hydrogen [8,13,14], so we have included such samples in our experiments as well.

Of particular interest from previous SANS work was the report of an intriguing experiment related to the Staebler-Wronski effect [9]. Using reactively-sputtered a-Si:H, grown 20 μm thick on a fused silica substrate at 300°C, the material was first checked to show a 30% increase in ESR spin density between the annealed (180°C) and illuminated states (4 h of visible light). No other opto-electronic or structural data were provided for this one sample investigated. The SANS was then

measured in this light-soaked condition (state B), followed by an anneal to return to state A, and the SANS re-measured. A 25% drop in intensity was observed, with no apparent change in the angle dependence. The illumination was then repeated and a 25% increase in intensity was seen. In order to explain this rather dramatic, reversible change in the SANS at all angles, a relatively long-range (~10 nm) reversible motion of H between the two states is required as suggested by applying a model developed earlier [15] to indicate the movement of H to (during illumination) and from (during annealing) the low density boundary regions surrounding the dense matrix regions [16]. Our experiments were designed to include a search for such a light-induced effect.

To our knowledge, there have been no previous SANS studies of a-SiGe:H or a-SiC:H alloys which are of interest for multijunction solar cells. Our experiments have also included a few such alloys.

3.1.2 SANS Experimental Details

A total of 24 samples were prepared for the SANS studies. Most of them were grown at NREL and USSC. Table I lists the samples and important deposition conditions. The ID numbers given in Table I are used throughout the discussion and the "H" and "D" designations conveniently indicate samples containing H or D (The original sample numbers provided by the film growers are available upon request). Note that many of the samples are hydrogenated/deuterated *pairs* (prepared under nominally identical conditions except the gases were fully or partially deuterated rather than hydrogenated) that will prove valuable in separating the H distributions from other heterogeneity such as voids and surface roughness. PECVD and HWCVD samples have been grown under conditions similar to those that yield high efficiency solar cells [17,18]. A comparison of these two materials is of current interest due to evidence of differences in structural features, particularly in the hydrogen distributions [4]. Also included are samples with a so-called "polymorphous" structure as described by the group of P. Cabarrocas of Ecole Polytechnique [19]. To optimize signal-to-noise [11,12], special c-Si substrates were used with the following specifications: float-zone wafers, 500 μm-thick (± 25 μm), undoped (resistivity>1000 Ω-cm), two-side polished with low surface roughness (<0.5 nm rms roughness, confirmed by AFM to be about 0.15 nm), (100) orientation. The wafers were diced into 2.5 cm x 2.5 cm squares to allow films to be grown with at least a 2.4-cm-diameter area to take advantage of the maximum neutron beam diameter available (2.2 cm). To minimize adhesion problems and allow bulk light-soaking, films

for the Staebler-Wronski effect study were grown to thicknesses of 1 or 2 μm. The maximum thickness selected for any of the PECVD or HWCVD films was 3 μm, while the Ecole Poly films reached 10 μm. Multiple films were grown under nominally identical conditions to allow stacking of up to 20 layers. The neutron absorption by the c-Si substrates at a thickness of 1 cm (20 substrates) is only about 3 %.

Table I. List of all SANS samples and their ID numbers. The total nominal film thickness (all layers) is t. All samples grown on same 500 μm c-Si substrate material (PCA material).

Prepared by:	SANS ID #	Film Type	Preparation Conditions	# Layers	t (μm)
USSC	UH1	a-Si:H	PECVD, SiH_4 + high H_2	12	24
USSC	UD1	a-Si:D	PECVD, SiD_4 + high D_2	12	24
USSC	UH2	a-Si:H	PECVD, SiH_4 + no H_2	12	24
USSC	UD2	a-Si:D	PECVD, SiD_4 + no D_2	12	24
USSC	UH3	a-SiGe:H	PECVD, SiH_4+GeH_4 + high H_2	8	14
USSC	UD3	a-SiGe:D	PECVD, SiD_4+GeD_4 + high D_2	8	14
USSC	UH4	a-Si:H	PECVD, Si_2H_6 + high H_2, Ts=225°C	12	24
USSC	UD4	a-Si:H,D	PECVD, Si_2H_6 + high D_2, Ts=225°C	9	22
USSC	UH5	a-Si:H	PECVD, Si_2H_6 + high H_2, Ts=300°C	8	20
USSC	UD5	a-Si:H,D	PECVD, Si_2H_6 + high D_2, Ts=300°C	10	25
NREL	NH1	a-Si:H	HWCVD, SiH_4 , Ts=360°C, 2 filaments	19	19
NREL	ND1	a-Si:D	HWCVD, SiD_4, Ts=360^oC, 2 filaments	19	19
NREL	NH2	a-Si:H	HWCVD, SiH_4, Ts=200^oC, 2 filaments	19	19
NREL	ND2	a-Si:D	HWCVD, SiD_4, Ts=200^oC, 2 filaments	19	19
NREL	NH3	a-Si:H	HWCVD, SiH_4, Ts=380^oC, 1 filament	10	19
NREL	ND3	a-Si:D	HWCVD, SiD_4, Ts=380^oC, 1 filament	6	12
NREL	NH4	a-SiGe:H	HWCVD, SiH_4+GeH_4	10	15
NREL	NH5	a-SiGe:H	HWCVD, SiH_4+GeH_4, Ts=370^oC, 2 filaments	8	16
NREL	NH6	a-Si:H	HWCVD, SiH_4, 100Å/s, Ts=380^oC, 2 filaments	8	22
NREL	NH7	a-Si:H	HWCVD, SiH_4+H_2, 30Å/s, Ts=280^oC, 2 filam.	8	24
BP-Solar	SH1	a-SiC:H	PECVD, SiH_4+CH_4+H_2, Ts=250^oC	16	16
EcolePoly	PH1	a-Si:H	PECVD, SiH_4, Ts=250^oC, standard material	3	15
EcolePoly	PH2	pm-Si:H	PECVD, SiH_4+H_2,Ts=250^oC, polymorphous	2	20
EcolePoly	PD2	pm-SiH,D	PECVD, SiH_4+D_2, Ts=250^oC, polymorphous	2	20

PECVD films were grown with either SiH_4 + H_2 or SiD_4 + D_2 and HWCVD films with SiH_4 or SiD_4. PECVD samples were grown with "high dilution" of $H_2(D_2)$, which yields the best devices [17] and improved medium-range order [3]. HWCVD samples were grown at elevated substrate

temperatures (360°C) which yields lower saturated defect densities, better devices [18], and improved medium range order [4] compared to lower substrate temperatures. The use of two filaments under HWCVD conditions yielded films of reasonably uniform thickness over an area that allowed simultaneous deposition on 4 of the substrates. However, this modification may have led to enhanced heterogeneity due to a higher deposition rate. For the Staebler-Wronski study, prior to the SANS measurements, the four sets of films UH1, UD1, NH1, and ND1 were subjected to 300 h light soaking under AM1.5 conditions.

The SANS measurements were made on the 30 m beam-line NG-3 of the NCNR [20]. Data were collected in an area detector (64 cm x 64 cm, 1 cm resolution) over a momentum transfer range from $q = 0.05\ nm^{-1}$ to $3\ nm^{-1}$ [$q = (4\pi/\lambda)\sin\theta$, where 2θ is the scattering angle and λ is the neutron wavelength] using two detector positions (2 m and 13 m from the sample). The use of these two positions can often be seen in the data by a non-perfect overlap of data. A wavelength of 0.6 nm was selected with a spread of $\Delta\lambda/\lambda = 34\%$, which prevented any double-Bragg diffraction from the c-Si substrates and allowed a high neutron flux at the sample of the order of $10^6\ cm^{-2}s^{-1}$. The samples were mounted in a chamber that allowed multiple (up to 7) sample mounting, a vacuum to reduce background scattering, and *in-situ* sample annealing. The four samples which had been previously light-soaked were measured in this state (Staebler-Wronski state B), then annealed *in-situ* at 190°C for 1 h (Staebler-Wronski state A), then remeasured without disturbing except to shift from one sample to the other via the automatic sample changer. The observed two-dimensional SANS intensities were apparently circularly symmetric for all samples and therefore circularly averaged and converted to absolute cross-section values, $d\Sigma/d\Omega$ ($cm^{-1}str^{-1}$), using standard procedures [20] that included subtracting the incoherent scattering (q-independent) from the substrates. The latter was measured with a stack of c-Si substrates similar in thickness to the stack for a sample and confirmed to be q-independent and of the correct magnitude ($\sim 1\times10^{-4}\ cm^{-1}str^{-1}$) thereby demonstrating that no extra scattering was coming from our carefully selected substrates.

3.1.3 Results and Discussion of SANS Experiments

The analysis of the SANS from the Staebler-Wronski samples (UH1, UD1, NH1, ND1) has been described in detail elsewhere [21]. The important conclusion is that no evidence for the large change in SANS between states A and B was found. No detectable changes were found to a precision as good as ± 3%. This is consistent with the very small structural changes being observed

in association with the Staebler-Wronski effect [22]. Also discussed was the large increase in SANS for sample UD1 compared to UH1 and its association with a partial microcrystallinity in UD1 [21]. We now present results on all the samples in Table I.

a. *Sample compositions and actual thicknesses*

In order to interpret the role of H and D, as well as the role of Ge and C alloying, the composition of each sample is needed. The bonded H and D contents were obtained from FTIR measurements at NREL on one or two of the layers grown on the c-Si wafer material (i.e. from the actual SANS samples). Similarly, one or two of the actual SANS films were used to obtain the Ge and C contents via electron probe microanalysis (EPMA) at NREL. Although nominal thicknesses were provided as shown in Table I, the actual thickness is needed for quantitative analysis of the SANS data in absolute units and for analysis of the transmission FTIR data. Due to some variation of the thickness from layer to layer, a method was developed to measure the thickness of *each* of the layers for a given sample (as many as 19 in some cases – Table I). A few of the films could be measured directly and accurately by profilometry but this was not possible on all layers due to difficulty in producing good, sharp steps. These few films were used as calibration standards for the following x-ray procedure: the height of the first scattering peak from the amorphous film was measured by mounting a film in the XRD system and measuring the count rate at three 2θ values (20°-left side of peak, 27.8^o- on the peak, 38.8^o-right side of peak). The left and right count rates were used to establish the background (sloping) and the peak height was calculated. It was also necessary to develop a thickness correction for x-ray absorption by the different film thicknesses (straightforward based on the known geometry and the known absorption coefficients for a given composition of Si, Ge, C). This was then measured for all layers and a total SANS sample thickness determined as well as the actual thickness for the layers used for the FTIR measurements. The method of using x-rays for this thickness measurement is thought to be quite relevant since it uses a beam which averages over a central area of each film similar in size to the neutron beam. Table II presents the composition and thickness results for all the samples.

Table II. Compositions of SANS samples and actual thicknesses. The actual layer thickness of the IR sample is t_{IR} and that of the SANS sample is t_{SANS}.

Sample	[Ge] % Ge/(Si+Ge)	[H] % H/(5E22 cm^{-3})	[D] % D/(5E22 cm^{-3})	t_{IR} µm	t_{SANS} µm
UH1	0	11	0	2.1	24.2
UD1	0	~0.5	13	1.7	20.4
UH2	0	13	0	2.1	24.8
UD2	0	< 0.5	13	1.8	21.0
UH3	40	10	0	2.3	18.3
UD3	56	<0.5	8	1.6	13.1
UH4	0	15	0	1.8	22.6
UD4	0	8.5	6	2.9	23.0
UH5	0	12.5	0	2.0	17.2
UD5	0	7.5	5	2.7	28.9
NH1	0	4	0	0.8	17.2
ND1	0	<0.5	3	0.8	18.6
NH2	0	11	0	0.8	16.3
ND2	0	<0.5	7	0.9	19.2
NH3	0	6.5	0	2.0	20.5
ND3	0	~1	5	1.6	10.1
NH4	10	9	0	1.7	16.2
NH5	15	3	0	2.2	18.6
NH6	0	7	0	3.3	28.3
NH7	0	3	0	3.1	23.6
SH1	[~1 % C]	25	0	0.5	8.2
PH1	0	11	0	4.8	14.6
PH2	0	19	0	10.0	20.4
PD2	0	6	12	10.0	19.9

One can compare the nominal thicknesses (Table I) and the actual thicknesses (Table II) to see that significant differences exist. It is interesting that fully deuterated PECVD samples UD1, UD2, and UD3 are all 15-30% thinner than the hydrogenated companions despite the nominal goal of equal thicknesses, while an opposite trend is seen for the HWCVD ND1/NH1 and ND2/NH2 samples. Note also that the partially deuterated films UD4 and UD5 tended to be thicker than the design values. Some of the HWCVD samples were significantly thicker than expected (NH5 and NH6). The a-SiC:H sample turned out to be only about 50% as thick as expected.

To analyze the FTIR data, the following calibration factors and assumptions were implemented by NREL:

IR Mode	Calibration factor	Comments
640 cm^{-1}	2.3e19 cm^{-2}	this was determined for a-Si:H with calibrated samples in the NREL lab and is in general agreement with the Langford et al [23] value of 2.1e19 cm^{-2}
640 cm^{-1}	2.5e19 cm^{-2}	this was determined for a-SiGe:H with calibrated samples in the NREL lab. The calibration set looked good for all but one sample that was mostly Ge
1450 cm^{-1}	1.6e20 cm^{-2}	this is for deuterium in a-Si:D and is from ref [24]. It is = sqrt(2) * 2000cm^{-1} factor
1450 cm^{-1}	3.0e20 cm^{-2}	this is for deuterium in a-SiGe:D and is derived from NREL calibration samples. It is = sqrt(2) * 2000cm^{-1} factor
2000 cm^{-1}	1.1e20 cm^{-2}	this is for a-Si:H and is from ref. [24] and is in general agreement with the Langford et al [23] value of 0.9e20 cm^{-2} for the 2000 cm^{-1} line.
2000 cm^{-1}	2.1e20 cm^{-2}	this was determined for a-SiGe:H with calibrated samples in the NREL lab. The calibration set looked good for all but one sample that was mostly Ge.
2100 cm^{-1}	2.2e20 cm^{-2}	this is for a-Si:H and is the Langford et al [23] value for the 2100 cm^{-1} line. Here it is used for the a-SiC:H data

From Table II one can compare the H and D concentrations for the fully deuterated samples versus those only partially deuterated. Since the presence of even small amounts of H can cause significant incoherent (background) scattering in the SANS, the FTIR data were examined carefully for small amounts and upper limits were estimated as indicated in the table. For the H/D pairs, the total H+D content tends to be close to that in the H-only samples, except for the NH2/ND2 pair.

Finally, regarding the alloy compositions, it is interesting that the same nominal conditions for UH3 and UD3 yielded quite different Ge contents, 40 vs 56 at.%. This and the tendency for microcrystallite formation with deuterated gases [21] shows an inherent difficulty in producing films with nominally identical microstructure except for the replacement of H by D. This needs to be kept in mind as we analyze and interpret the SANS data.

b. *SANS data examples*

Several sets of SANS data sets will now be presented to illustrate the quality and wide range of behaviors for the different types of samples. Figure 1 compares data from high-hydrogen dilution PECVD a-Si:H (UH1) and elevated-substrate temperature HWCVD a-Si:H (NH3). The growth conditions are those used to generate the highest efficiency solar cells by the respective techniques [17,18]. Note the significant differences in the shape and magnitude of the SANS. The data of UH1 tend to drop more steeply and level off sooner indicating some larger scale features (>20 nm) and very few if any smaller scale features (< 5 nm).

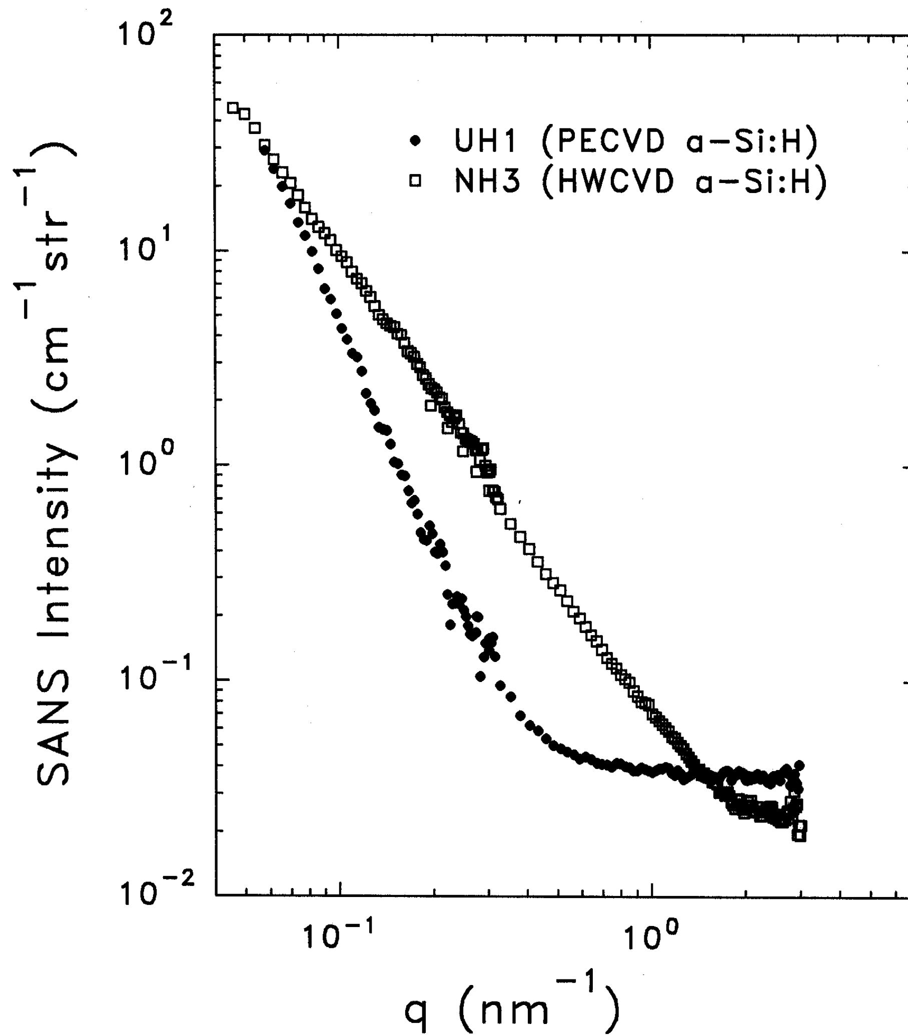

Fig. 1. SANS data comparison for PECVD vs HWCVD a-Si:H

The near constant slope of the NH3 up to the highest q's indicates a rather broad distribution of scattering centers from large to quite small. Results of quantitative fitting with a distribution of spheres will be presented in a later section. The approach to constant levels of scattering at the highest q's for both samples is due to the incoherent scattering from the H. Si (or any O) contributes insignificantly to this background due to a very small incoherent cross section compared to that of H (0.025 vs 80.3 barns). The higher level for UH1 is consistent with the higher H content as listed in Table II. Quantitative analysis of this incoherent scattering for all samples will be presented in a later section and compared to theory.

Figure 2 compares one of the H/D pairs, NH3/ND3, to illustrate the effect of deuteration. The shapes of the SANS curve are quite similar indicating similar nanostructures but is clear that the ND3 has little or no H due to its lower level of background scattering at high q. The incoherent cross section for D is a factor of about 40 less than that of H (2.05 vs 80.3 barns).

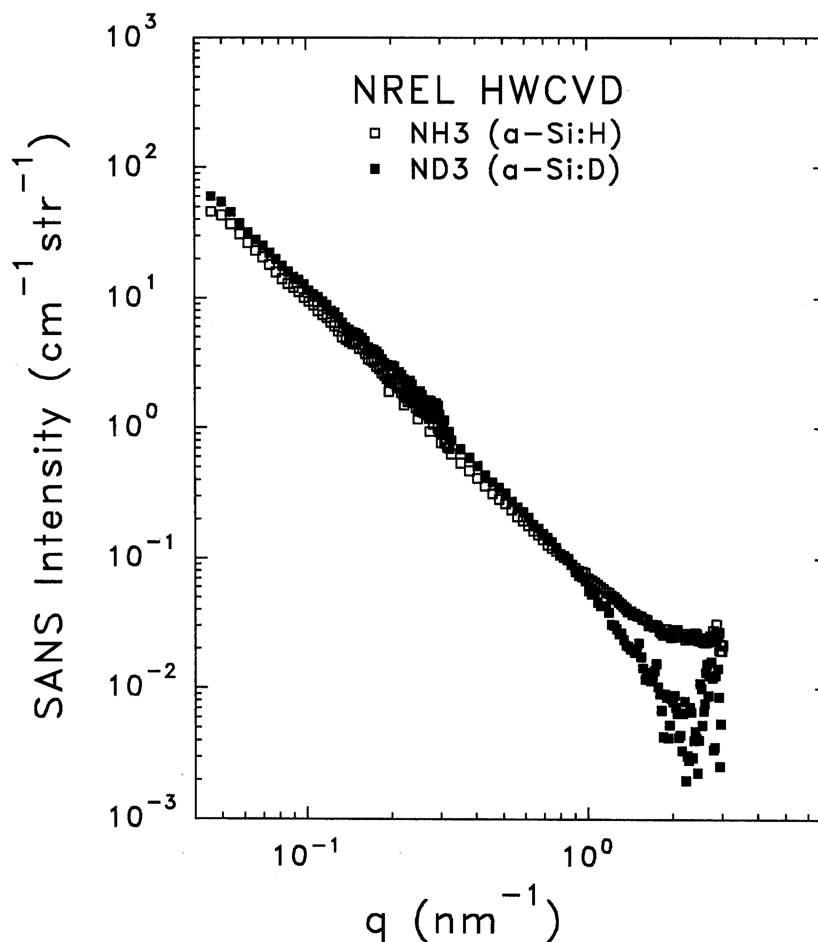

Fig. 2. SANS data from hydrogenated vs deuterated HWCVD material.

Figure 3 compares both H/D pairs of PECVD a-Si grown with partial deuteration (only the H_2 diluting gas replaced by D_2) and H/D pairs of a-SiGe alloys. Several features are of interest: (i) the much stronger SANS from the Si-Ge alloys; (ii) the similar shape of the curves for H/D pairs; (iii) the expected drop in background scattering for the fully deuterated alloy (UD3); only a modest drop in background scattering as expected from the *partially* deuterated UD4 (from Table II – 8.5% H and 6% D vs 15% H in UH4); (iv) a significant drop in the SANS above about 0.3 nm^{-1} for UD4 compared to UH4. The latter is good evidence for H-rich scattering features on the nanometer scale. Quantitative analysis will be presented in a later section.

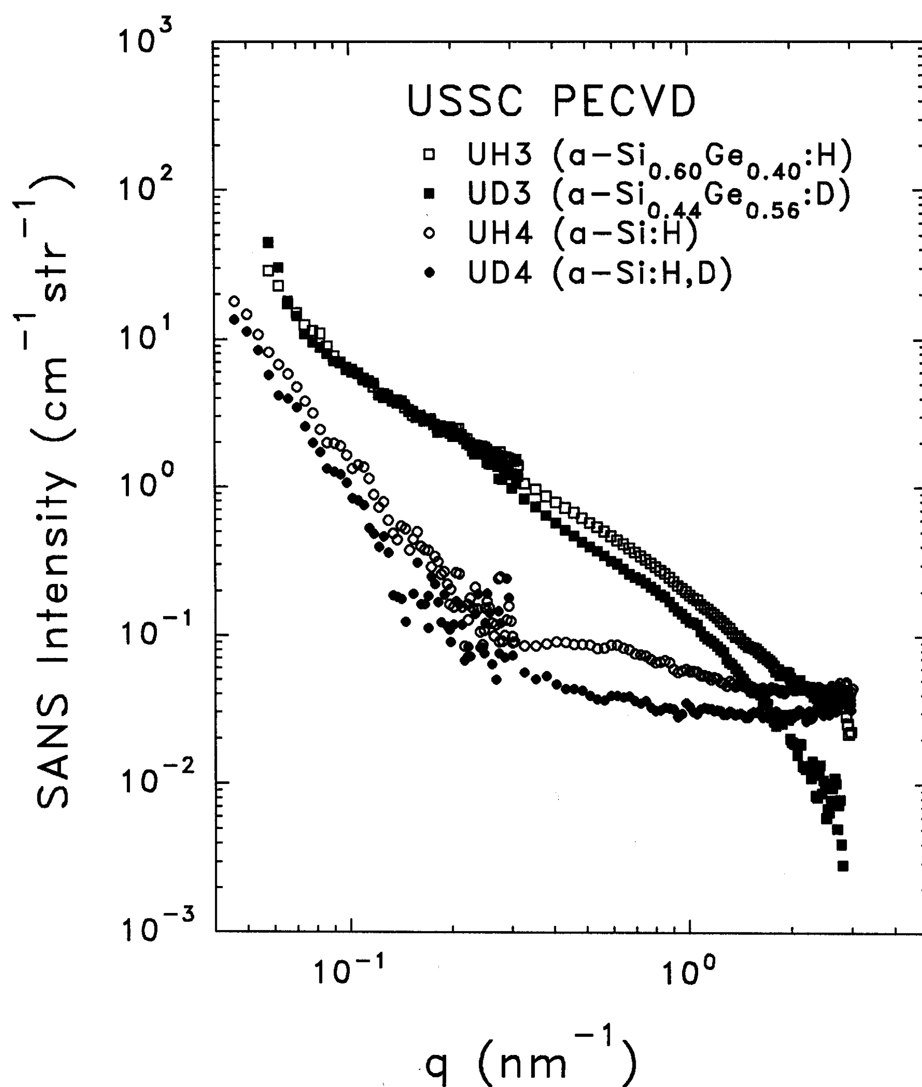

Fig. 3. Comparison of SANS data from H/D pairs of a-Si:H/D and a-SiGe:H/D alloys.

The SANS from the a-SiC:H alloy (SH1) is compared with that from a-Si:H (UH1) in Fig. 4. The shape appears quite similar but the level of scattering is significantly enhanced from the alloy. The rather high H content of 25 at.% (Table II) is not enough to explain (on the basis of incoherent scattering) the high level of scattering above about 1 nm^{-1}. An explanation will be presented later based on known SAXS data from such alloys.

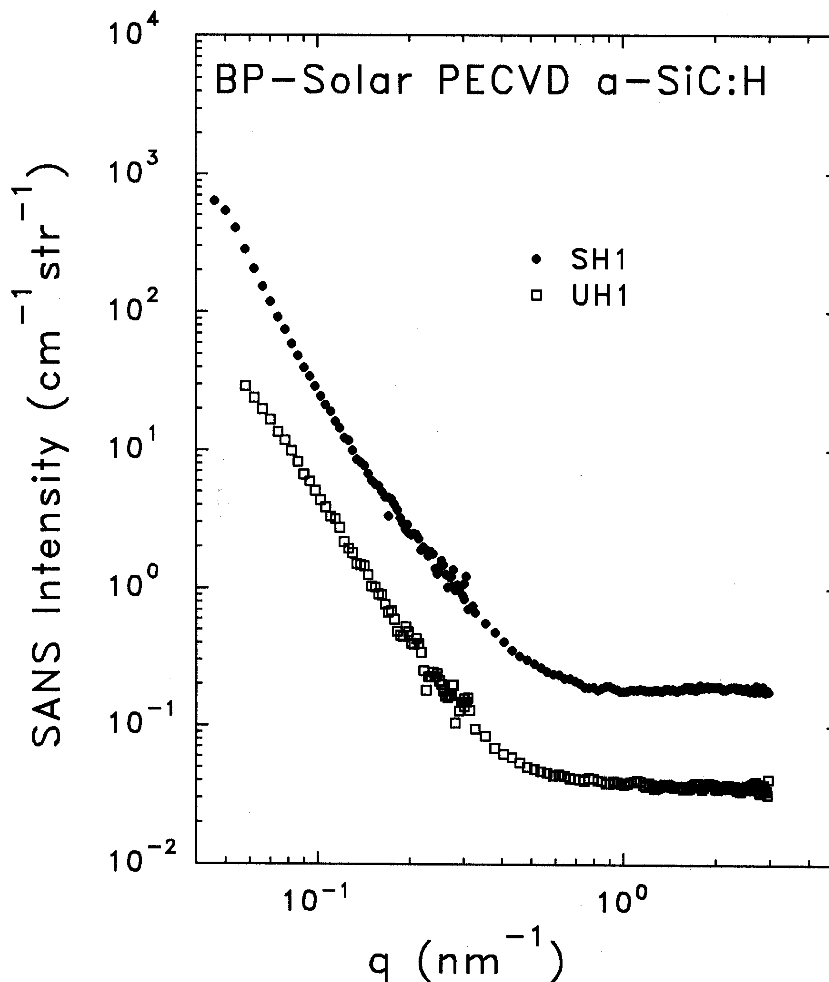

Fig. 4. SANS from a-SiC:H alloy compared to that from a-Si:H.

As a last example, Fig. 5 shows the SANS data from the polymorphous Si:H/D films compared to a standard PECVD a-Si:H film, all prepared at Ecole Polytechnique. Note that the shapes of the SANS curves from the two pm-Si:H/D films are similar to each other (and quite different from any of the data shown in Figs. 1-4) but the partially deuterated sample yields

significantly weaker signals. The standard a-Si:H (PH1) yields the weakest SANS. The background levels at high q scale nicely with the H contents listed in Table II.

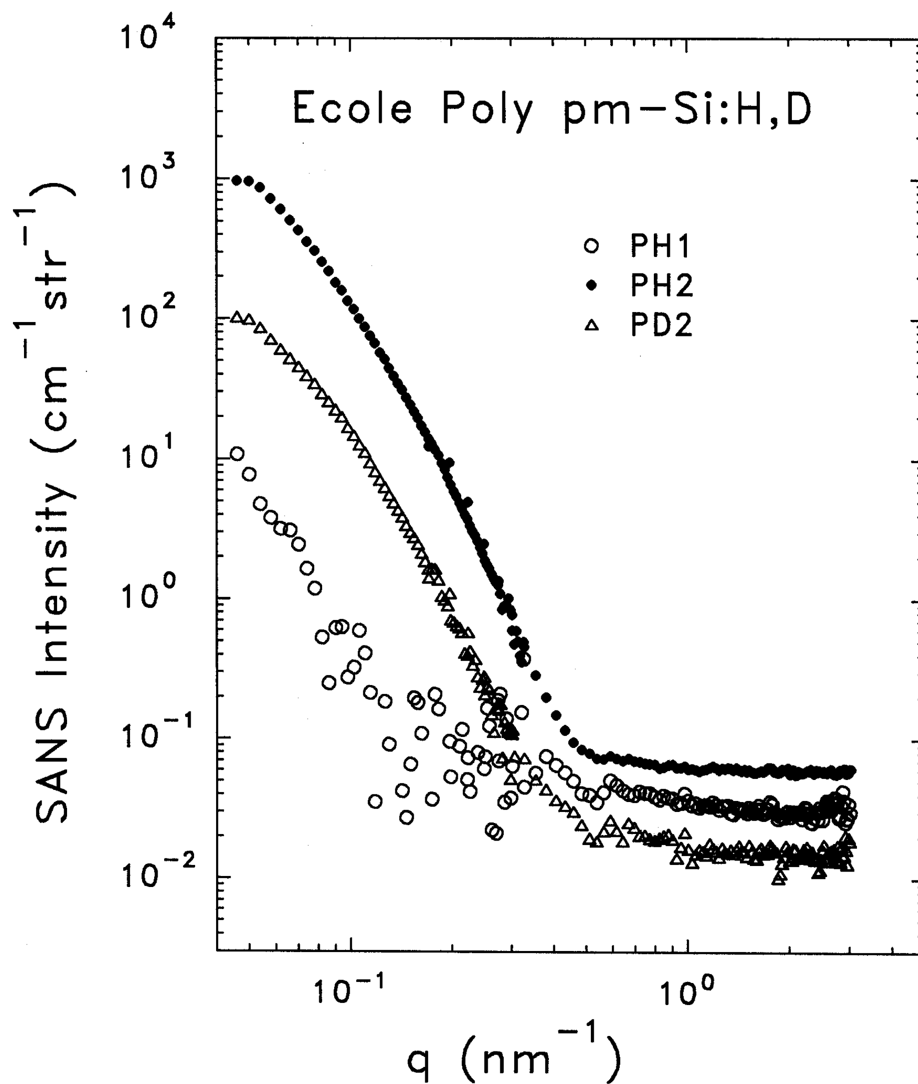

Fig. 5. SANS from polymorphous Si:H/D (PH2 and PD2) and standard a-Si:H (PH1).

c. *Quantitative analysis of SANS data*

Each of the experimental SANS data sets of intensity I versus q was fitted with the following function:

$$I = A\Sigma\,[F_iV_i^2P(qR_i)] + B/q^4 + I_{inc} \qquad (1)$$

The first term is scattering from a distribution of spherical objects each of radius R_i, with volume fraction F_i, volume V_i, and form factor $P(qR_i)$. The latter is a well-known Bessel function [13]. The constant A yields the absolute units of $cm^{-1}str^{-1}$ for the SANS intensity shown in the figures. The size range for R_i in the fitting program extends from 0.5 to 50 nm. The second term is known as Porod scattering [13] and is due to larger-scale features such that their q^4 scattering tail shows up at low q and cannot be accounted for by the first term. The last term is due to incoherent neutron scattering, is q-independent, and can be predicted from the sample composition and the known incoherent scattering cross sections of the elements. Here, this term is dominated by any H in the sample. The quantitative results from the fit include the volume fraction distribution F_i and the average diameter, $\langle D \rangle = 2\Sigma\ [F_iR_i]$. Another important quantity obtained from the fit is the integrated SANS intensity:

$$Q_{SANS} = 4\pi\int q^2 I_N dq \qquad (2)$$

Where I_N is the contribution from the first term in Eq. 1 (i.e. from the nanostructural features) and the integration is over the experimental range of q. The Q_{SANS} can be used to develop two or three phase models to account for this absolute magnitude of the scattering. The neutron scattering length density ρ_j of a given phase ρ_j can be calculated from an assumed composition, the known coherent cross sections, and a mass density [13]. One can then predict Q_{SANS} on the basis of phase volume fraction f_i as follows:

Two phase model

$$Q_{SANS} = (2\pi)^3 f_1(1-f_1)(\rho_1-\rho_2)^2 \qquad (3)$$

Three phase model

$$Q_{SANS} = (2\pi)^3[f_1f_2(\rho_1-\rho_2)^2 + f_2f_3(\rho_2-\rho_3)^2 + f_1f_3(\rho_1-\rho_3)^2] \qquad (4)$$

Note that $\Sigma f_j = 1$. Such models will be used below to interpret some of the results.

The following series of six figures show examples of the use of Eq. 1 in fitting the data and illustrates the wide variety in size distributions (see the inset in each figure). NH1 (Fig. 6) requires a rather wide distribution of diameters from 1 to 100 nm, with an average of 14 nm as shown in the inset. One can also see in Fig. 6 the non-perfect overlap of the data acquired at the two positions of the detector to cover the indicated q range.

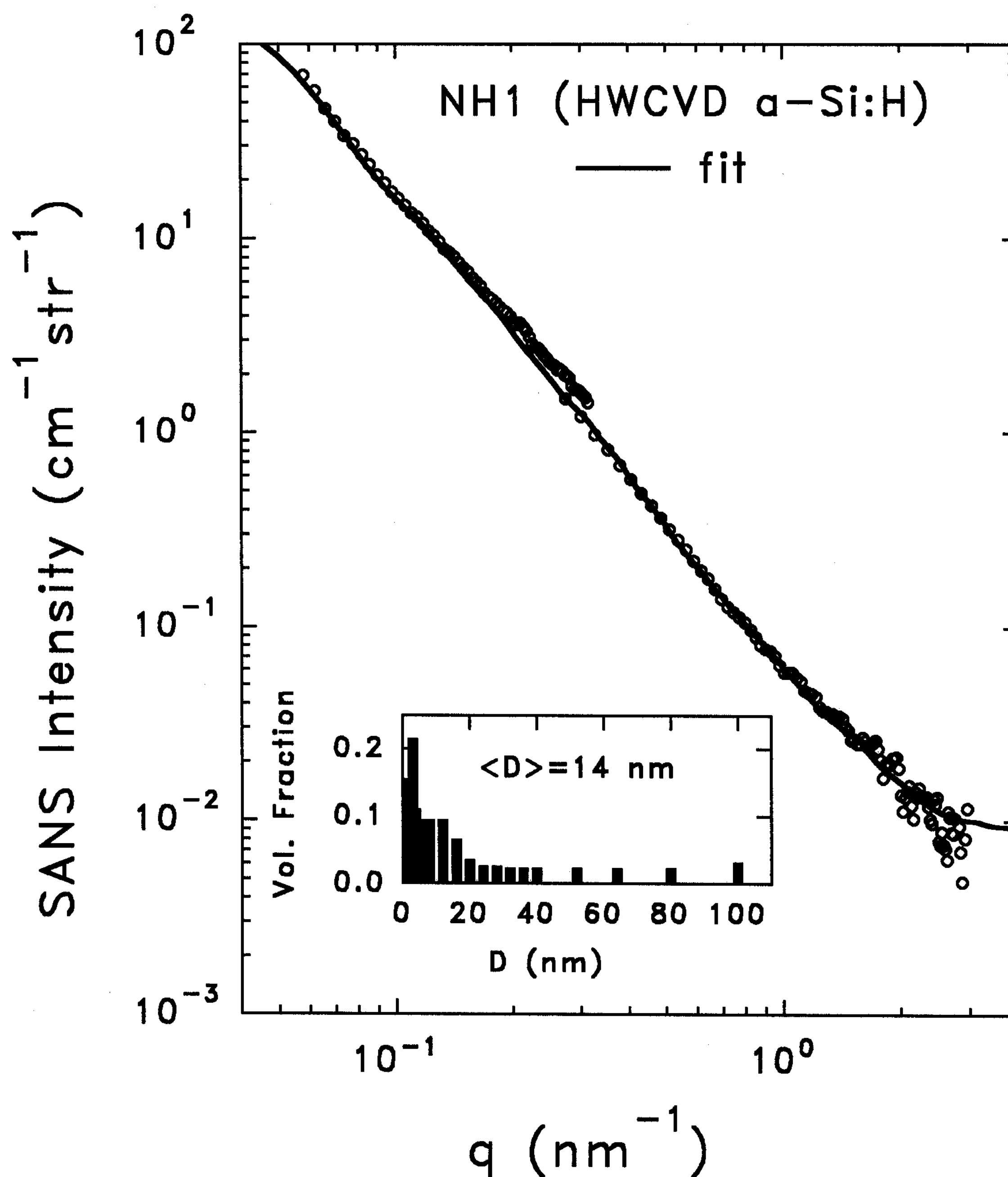

Fig. 6. Fit of Eq. 1 to the SANS data from a HWCVD a-Si:H film. Inset provides the diameter size distribution used in the fit.

NH5 (Fig. 7) shows a clear bimodal size distribution with sizes differing by an order-of-magnitude. The larger size fractions have been multiplied by a factor of 10 in the inset. Note from Eq. 1 that

each term in the distribution is weighted by the square of the sphere volume so larger spheres require only small volume fractions to contribute significantly to the SANS. One can see that the average diameter is strongly dominated by the smaller features.

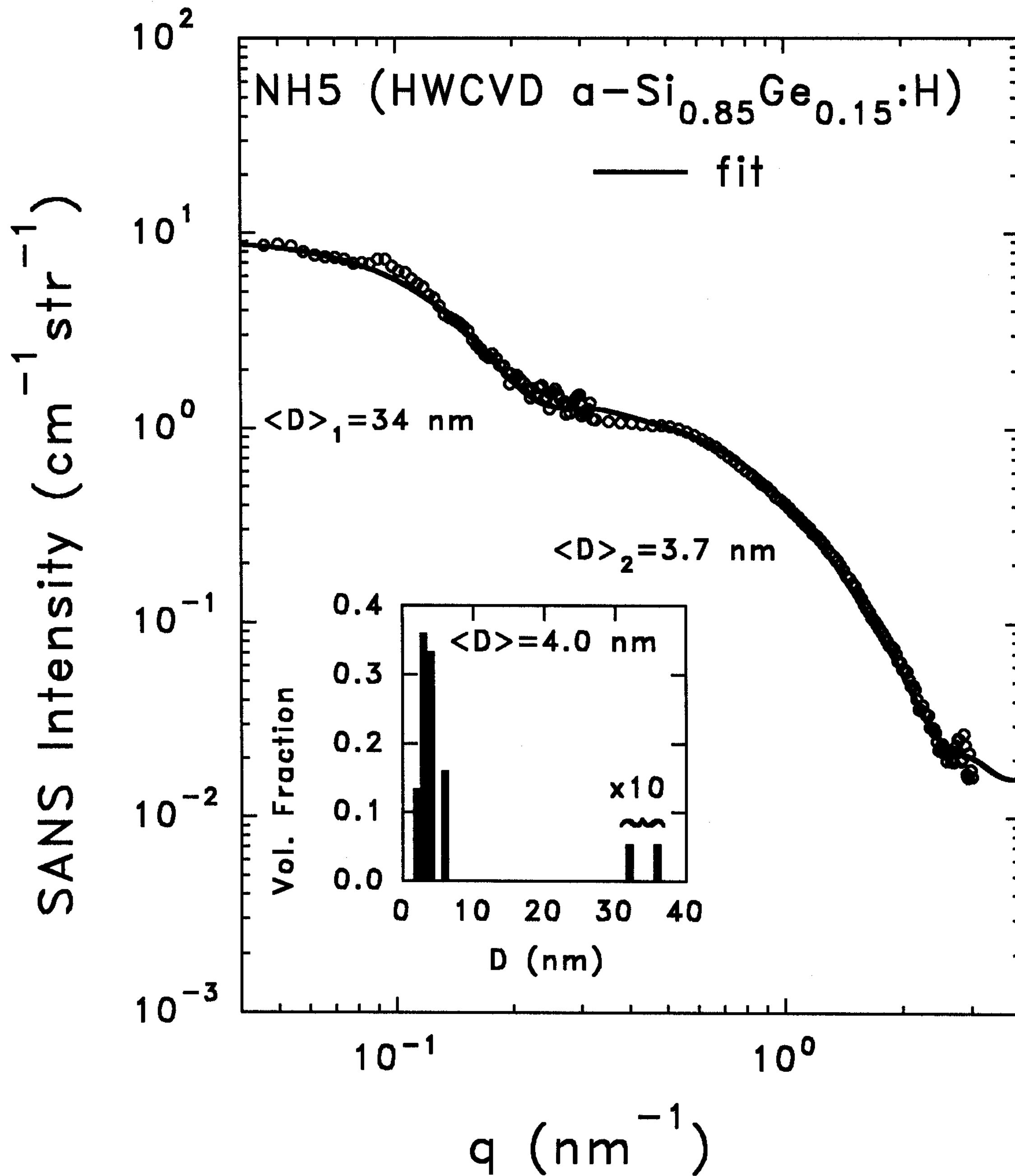

Fig. 7. Fit of Eq. 1 to SANS data from a HWCVD a-SiGe:H alloy.

Figure 8 shows the fit results for a HWCVD film grown at the ultra-high deposition rate of 10 nm/s. In this case the size distribution has a well-defined upper limit as seen by the flattening of the curve at low q. There is also no evidence of objects smaller than 4 nm since the curve again flattens at high q to yield a well-defined value of I_{inc} near 0.02 $cm^{-1}str^{-1}$.

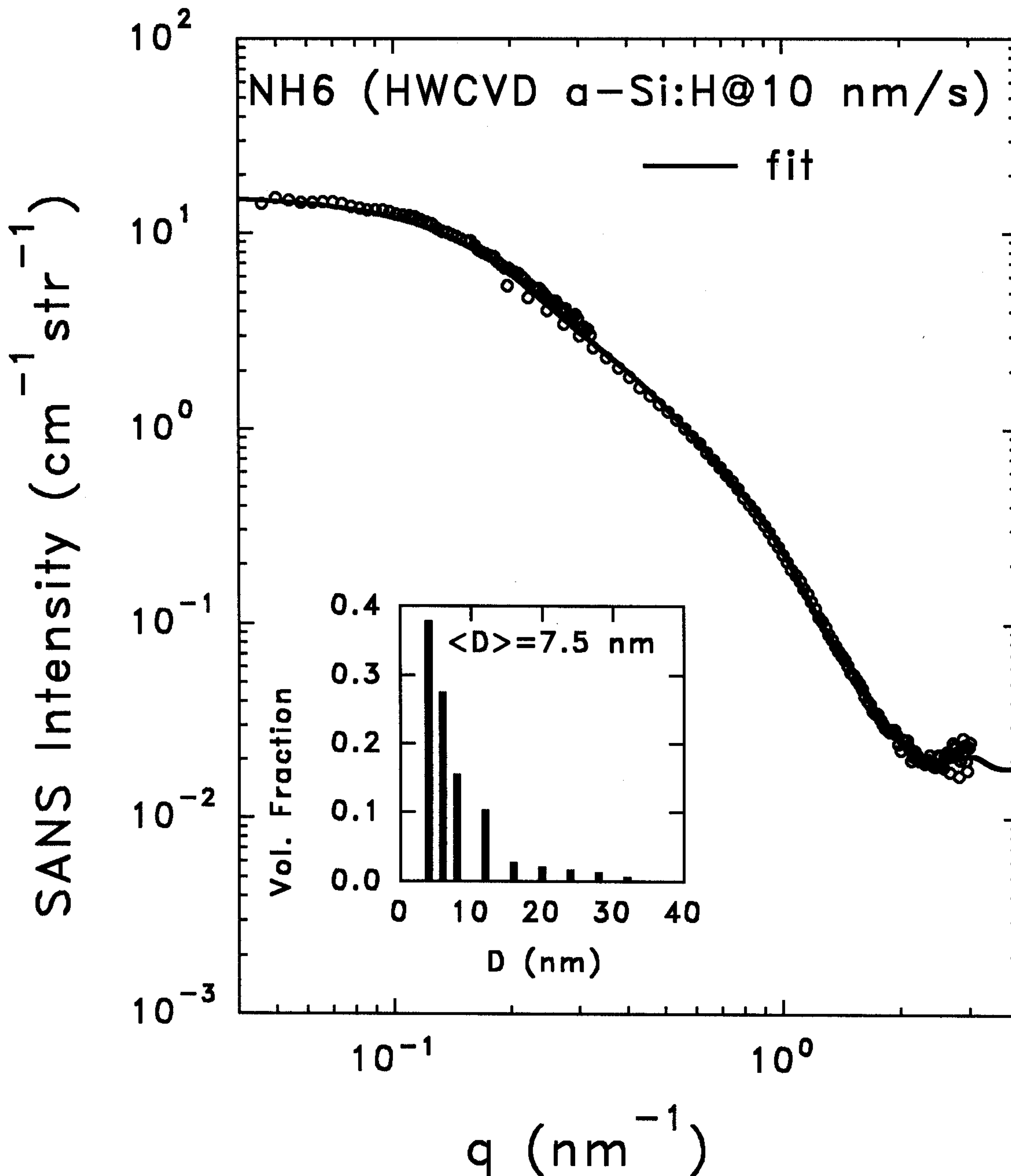

Fig. 8. Fit of SANS data from a HWCVD a-Si:H made at ultra-high deposition rate.

We now switch to the PECVD materials. Figure 9 shows the fit to the SANS data from the high-H_2-dilution a-Si:H sample (UH1). The dashed curve illustrates how close the data can be fitted using only the last two terms in Eq. 1. Only a very small contribution of 1 to 80 nm diameter scattering features are needed to fit the extra scattering above the dashed line. The corresponding size distribution is quite uncertain due to its weak contribution.

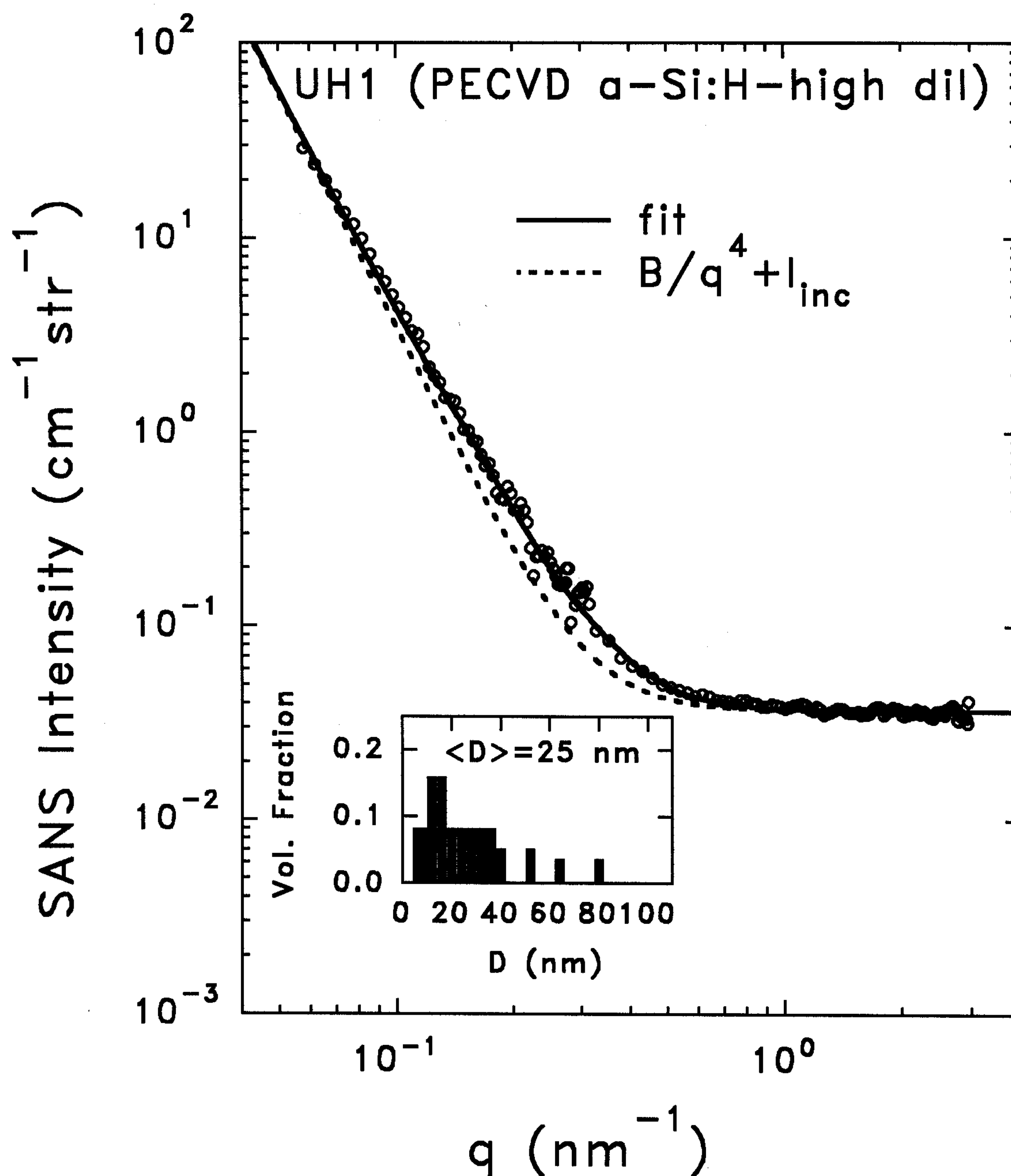

Fig. 9. Fit to SANS data from PECVD a-Si:H. Note that most of the signal can be fitted with just the Porod and incoherent contributions in Eq. 1 (the dashed line).

The PECVD a-SiGe:D alloy, UD3, is well-fitted in Fig. 10 with spheres mainly below 10 nm in diameter. Note the much different shape of this curve compared to the PECVD film without Ge in Fig. 9. These differences are quite similar to those observed in our previous SAXS studies of PECVD samples of a-Si:H and a-SiGe:H prepared by USSC [1].

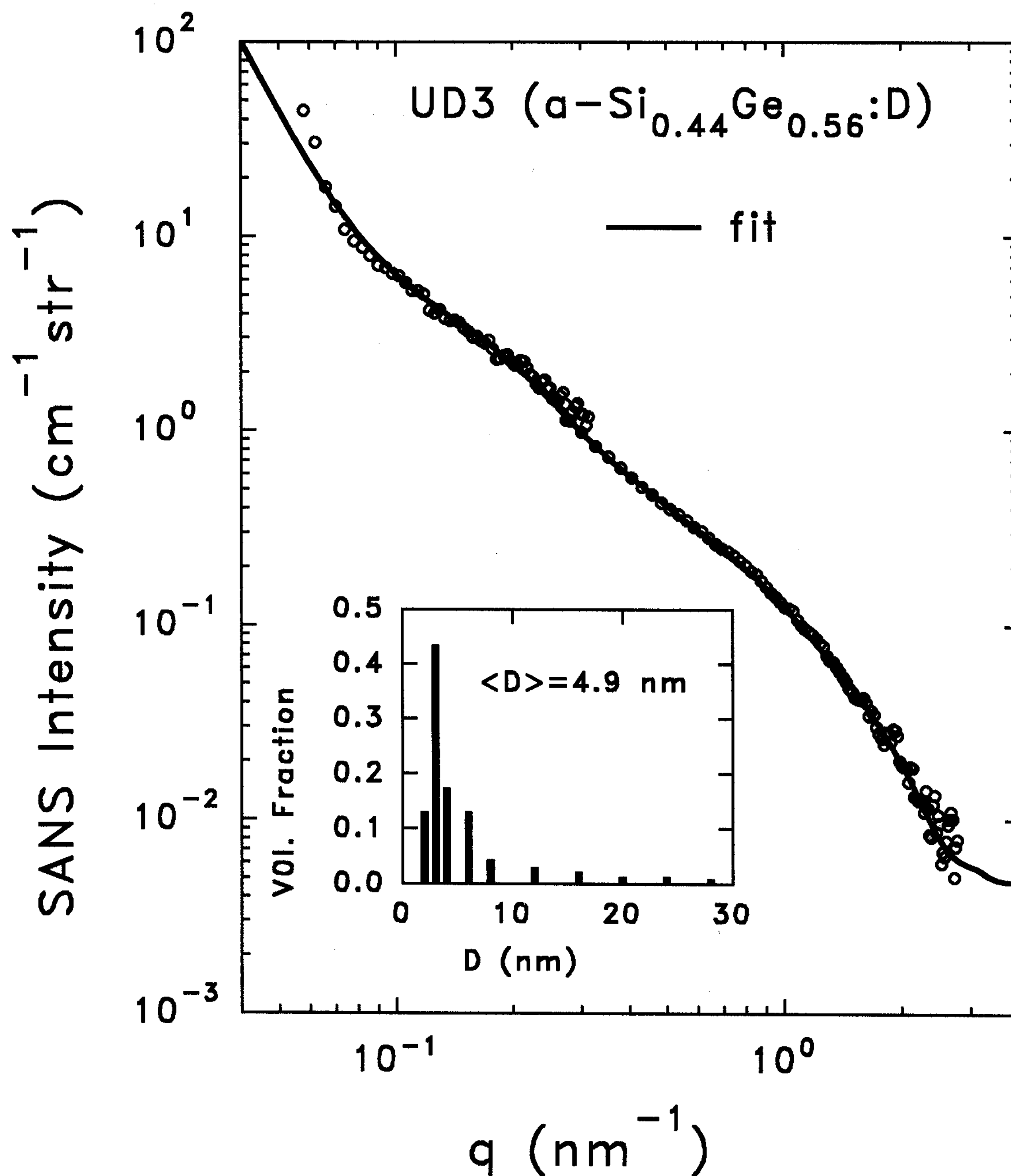

Fig. 10. Fit of SANS data from PECVD a-SiGe:D film.

Figure 11 shows evidence of another bimodal distribution of scattering features. Again, only very small fractions of the larger spheres are needed to account for the low-q rise of the intensity. It is interesting that there is extra scattering at high q compared to the PECVD material grown with silane (UH1) compared to this film grown with disilane (UH4). The extra scattering is due to features about 5 nm in diameter.

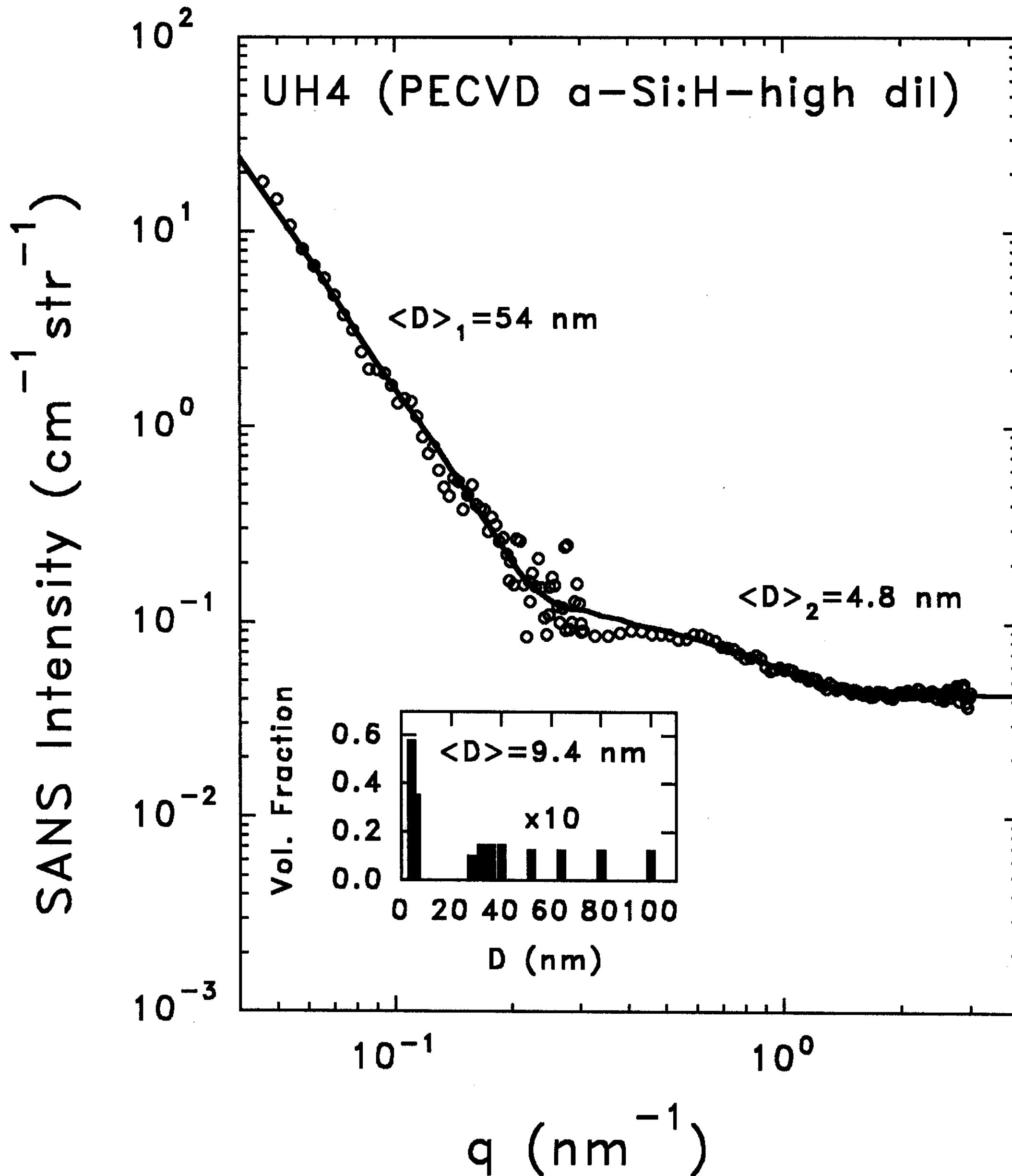

Fig. 11. Fit of SANS data from PECVD a-Si:H grown with disilane.

A summary of the integrated SANS intensities, the B, I_{inc}, and <D> parameters obtained from the fits for all the SANS samples is presented in Table III.

Table III. Quantitative SANS results from all samples.

Sample	Q_{SANS} (10^{21} cm^{-4})	B ($cm^{-1}str^{-1}nm^{-4}$)	I_{inc} ($cm^{-1}str^{-1}$)	<D> (nm)
UH1	0.037	0.00035	0.037	24
UD1	2.96	0	0.006	30
UH2	0.42	0	0.027	6.8
UD2	0.35	0	0.009	12
UH3	3.51	0.0003	0.034	4.9
UD3	2.94	0.00025	0.004	4.9
UH4	0.26	0.00004	0.043	9.4
UD4	0.050	0.00006	0.029	12
UH5	0.17	0	0.040	32
UD5	0.037	0	0.023	44
NH1	1.92	0	0.009	14
ND1	1.30	0	0.008	20
NH2	7.89	0	0.050	10
ND2	4.91	0	0.015	14
NH3	1.21	0	0.023	14
ND3	1.48	0	0.005	14
NH4	4.61	0	0.030	4.2
NH5	8.34	0	0.014	4.0
NH6	4.87	0	0.018	7.5
NH7	8.31	0	0.020	5.6
SH1	~15	0.0027	~0.10	~1
PH1	0.069	0.00004	0.031	~5
PH2	~2.5	0	0.060	~50
PD2	~0.32	0	0.016	~50

The items in the table with approximation signs are rather uncertain due to poor quality fits to the data. Further analysis is necessary to improve these fits.

We comment on the some features of the Table III results. In most cases of the H/D pairs, the deuterated sample shows smaller Q_{SANS}. For the UD1 sample we know the cause of its unusually large SANS – partial microcrystallinity [21]. This leaves only the NH3/ND3 pair as an exception. Note the wide range of Q's, from 0.037 to 8.3, a factor of more than 200. Also, the average sizes span a wide range from about 1 nm to about 50 nm. Keep in mind that some of the size distributions are bimodal in nature as shown in Figs. 7 and 11. The Si-Ge alloys (UH3/UD3,

NH4, NH5) all show relatively large Q's, with the HWCVD values significantly larger than the PECVD values, even though the latter have much higher Ge contents (Table II).

Before developing models based on two or three phases, we first demonstrate that the absolute intensities of the data yield good agreement with a theoretical treatment of the incoherent background. Since only the H and D in the films should contribute to I_{inc}, the theoretical expression will be:

$$I_{inc} = (\sigma_H[H] + \sigma_D[D])n/4\pi \,, \quad (5)$$

where σ_H and σ_D are the incoherent neutron scattering cross sections of H and D (80.26×10^{-24} cm^2 and 2.05×10^{-24} cm^2 [25]), respectively, [H] and [D] are the atomic fractions of H and D in the film, and n is the average atomic concentration in the film. Since the D cross section is a factor of 40 smaller, we correct the experimental values using σ_D and the D contents in Table II and calculate $I_{inc} - I_D$, where $I_D = \sigma_D[D]n/4\pi$. We then plot this in Fig.12 versus the H contents from Table II, taking $n = 5 \times 10^{22}$ cm^{-3}, the same atomic density as c-Si. From Eq. 5, the theoretical slope of this plot should be $\sigma_H n/4\pi$ = 0.319 and this is shown as the solid line in the plot. This excellent agreement gives us confidence in the experimental absolute magnitudes of Q_{SANS} from Eq. 2 for comparison to the models, Eqs. 3 or 4.

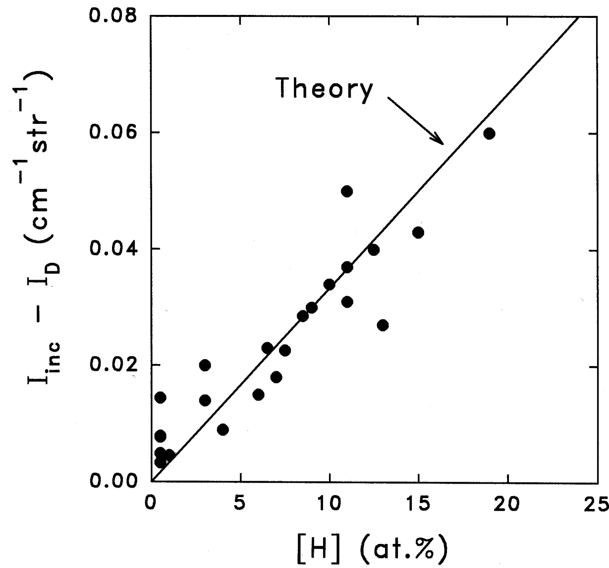

Fig. 12. Experimental values of the incoherent background scattering intensity (corrected for the D scattering) versus the H content from Table II compared with the theoretical prediction.

d. *Complementary structural data (SAXS and AFM)*

To help with model development, several of the SANS samples were supplied with companion films deposited under nominally identical conditions on Al-foil for SAXS measurements. Such complementary data can prove valuable since they are not sensitive to H or D but are sensitive to nanovoids (whether they contain H/D or not). Differences in size distributions of scattering features using SAXS versus SANS should be valuable in the interpretation. However, we must keep in mind the possible effect of differences in structure induced by Al-foil versus c-Si substrates. Hopefully this is not an important issue due to the relatively thick nature of all films (≥ 1 μm). One sample (NH1) was deposited on both Al-foil and thin c-Si and the results are similar. Table IV summarizes the results of the companion SAXS samples.

Table IV. SAXS results from companions to SANS samples. Q_T is the total integrated SAXS intensity (including the Porod scattering, A/q^3); Q_N is the integrated scattering from the nanostructural features (leaving out the Porod scattering), $<D>_N$ is the volume fraction average diameter of the scattering features based on spherical objects, $V_f(Q_N)$ is the volume fraction of voids based on Q_N and $V_f(Q_T)$ is the void fraction based on Q_T [see ref.1 for details on SAXS].

SANS Sample	Q_T (10^{22}eu/cm^3)	Q_N (10^{22}eu/cm^3)	A (eu/nm^3)	I_D (eu)	$<D>_N$ (nm)	$V_f(Q_N)$ (%)	$V_f(Q_T)$ (%)
UH1	14	≤ 2	4.5	12	NA	≤0.01	0.09
UD1	98	≤ 2	28	13	NA	≤0.01	0.6
UH2	7.5	~2	1.8	16	~2.5	~0.01	0.04
UD2	5.2	≤ 2	1.2	16	NA	≤0.01	0.03
UH3	202	189	4.0	73	3.0	0.6	0.7
UD3	462	446	5.0	76	3.4	1.1	1.2
NH1	207	203	1.2	6	3.1	1.2	1.2
(on c-Si)	164	162	0.8	6	3.1	1.0	1.0
NH3	7.3	5.7	0.5	5.5	~4	0.03	0.04
ND3	49	23	8	9	4.0	0.1	0.3
NH4	95	88	2.5	32	3.6	0.4	0.5
NH5	969	941	9	36	3.3	4.7	4.8
NH6	191	159	10	9	3.6	0.9	1.1
NH7	439	427	4	7	4.2	2.5	2.6
PH1	3	< 1	0.2	7	NA	< 0.01	0.02
PH2	107	22.7	27	14	3.0	0.1	0.6
PD2	234	109	40	12	3.7	0.2	1.4

Finally, to further aid the interpretation, a representative PECVD sample (UH1) and a representative HWCVD sample (NH1) were studied by AFM at NREL to investigate the surface features. Figures 13-16 shows AFM images and surface roughness maps.

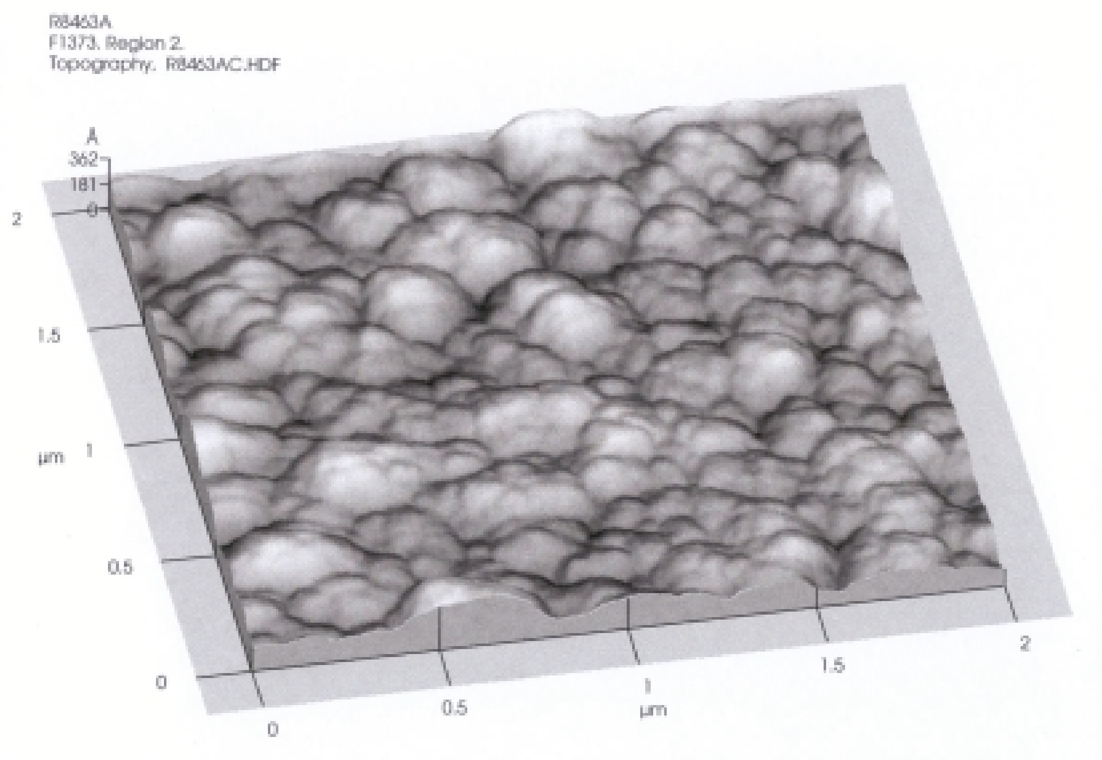

Fig. 13. AFM image of UH1 (PECVD a-Si:H).

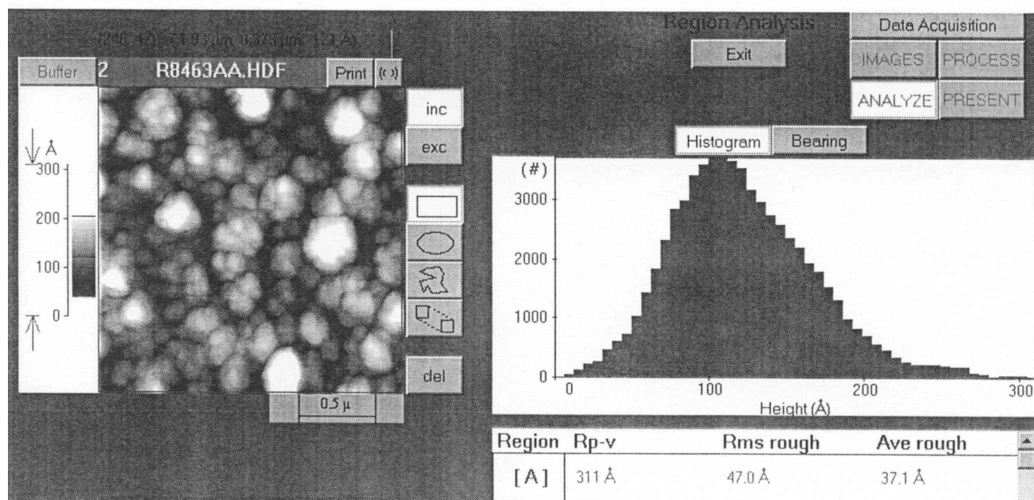

Fig. 14. AFM surface roughness distribution of UH1 (PECVD a-Si:H)

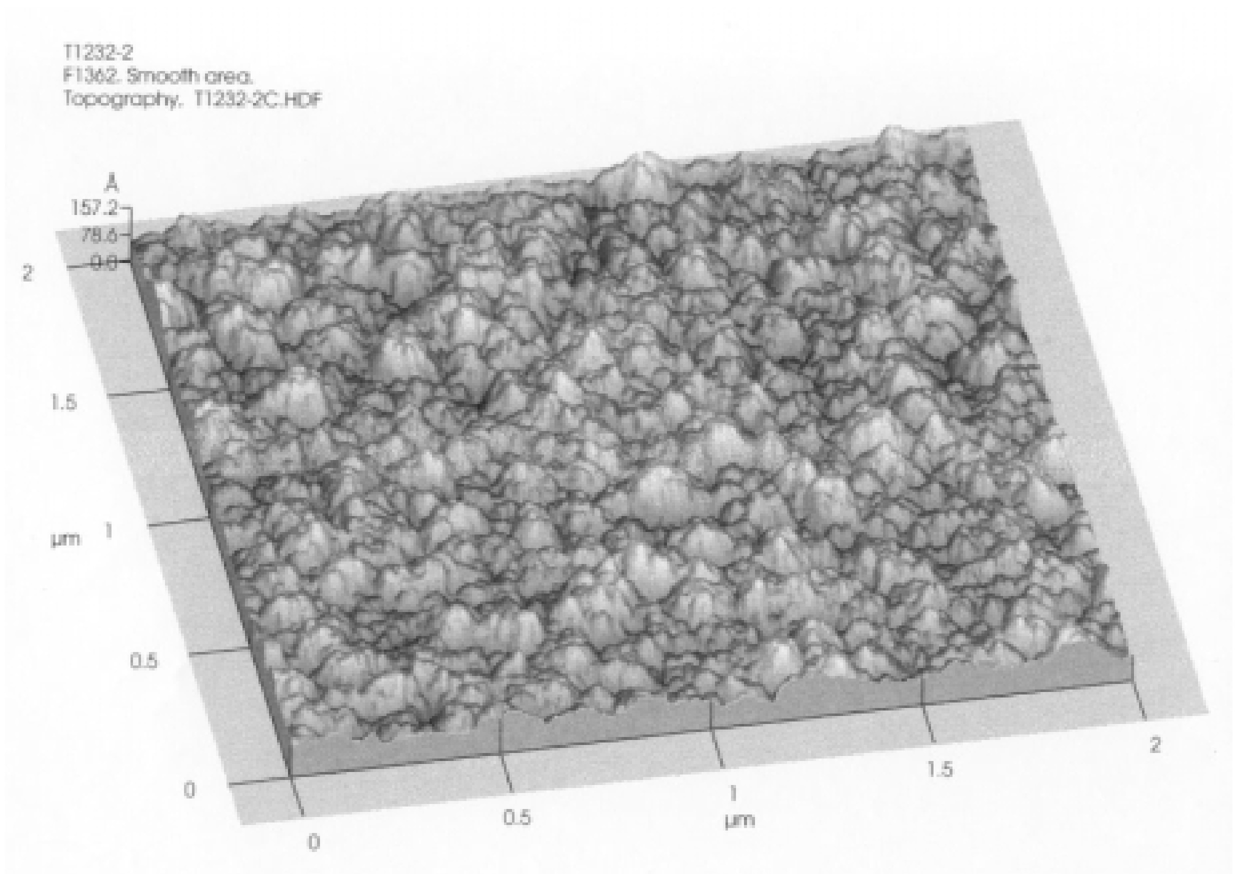

Fig. 15. AFM image of HWCVD a-Si:H (NH1).

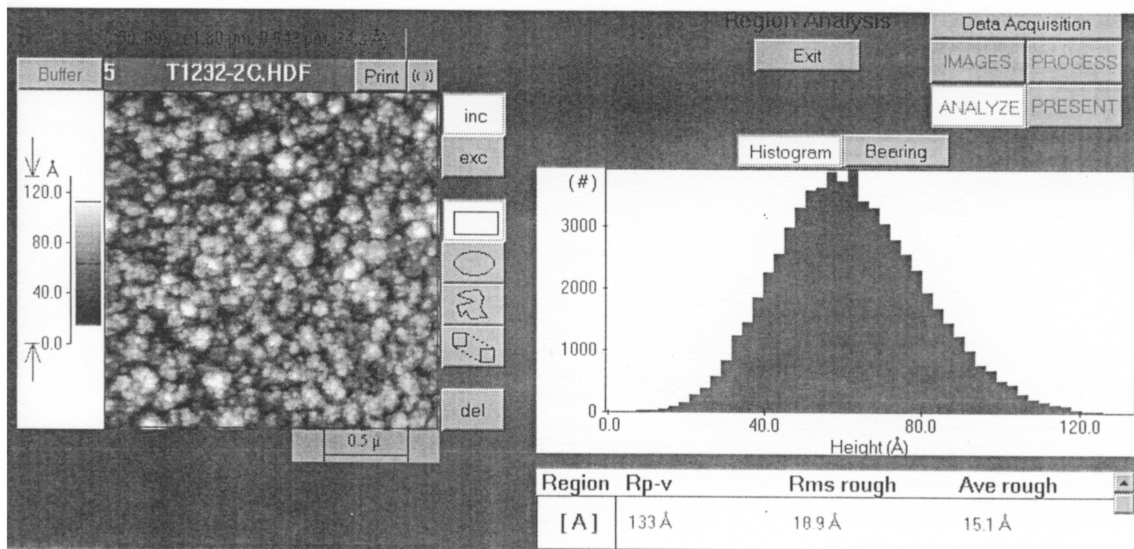

Fig. 16. AFM surface roughness distribution of NH1.

From these AFM data one can see that the PECVD a-Si:H has a larger vertical roughness (Rms = 4.7 nm) compared to the HWCVD a-Si:H (Rms = 1.9 nm). Also, the lateral dimensions of the roughness are larger for the PECVD material.

e. *Models under development*

Based on all the experimental data presented above we are developing the following interpretations depending on the different type of films studied. The PECVD films UH1, UH2/UD2, UH4/UD4, and UH5/UD5 and PH1 (UD1 is not included due to its partial microcrystallinity) all show similar SANS behavior with a steep low-q region followed by a weakly-q-dependent high-q region. This indicates a bimodal distribution of relatively large (> 20 nm) and relatively small (< 10 nm) scattering objects. A three phase model will be used with the dense, H-alloyed amorphous matrix being phase 1, internal, low-density, H/D-rich regions being phase 2, and the surface roughness being phase 3. The surface roughness can be modeled as voids with a volume fraction equal to the ratio of the Rms surface roughness to the film thickness (here the film thickness will be that of an individual layer rather than that of the SANS multilayer stack). For example, this ratio taken from UH1 AFM data (Fig. 14) and film thickness data in Table II is 4.7 nm/2000 nm = 0.002 or 0.2 vol.%. The phase 1 is modeled with a composition equal to that in Table II and with a typical mass density, d, based on the H/D content. The correlation d (g/cm^3) = 2.291 – 0.0068[H] will be used as developed from flotation density measurements in our lab ([H] is the atomic % H listed in Table II). The low-density, H/D-rich regions will be modeled with adjustable volume fraction, composition, and mass density to fit the SANS and SAXS data. The composition and mass density are directly related to the scattering length density ρ shown in Eq. 4.

The HWCVD films NH1/ND1, NH2/ND2, NH3/ND3, NH6, and NH7 will require another level of internal inhomogeneity based on preliminary calculations. The amorphous matrix must contain H/D-rich and H/D-poor regions in addition to nanovoids. This is made clear by the upper limit on nanovoids from the SAXS results. Such inhomogeneity would be consistent with the NMR results from HWCVD a-Si:H [26] and with a recent interpretation by Baugh and Han [27]. Application of this model to the NH3/ND3 pair is able to yield the quantitative Q_{SANS} with a 30% volume fraction of H/D-rich phase (about 20 at.%), 70 vol.% with no H/D and about 0.3% nanovoids. The ultra-high deposition rate films NH6 and NH7 will require signifcantly more nanovoids, about 1 to 2 vol.% according to the SAXS.

The a-SiGe:H/D alloys, UH3/UD3, NH4, and NH5 will be modeled with a more complex phase distribution based on the ASAXS results presented below. In addition to nanovoids, this class of material has significant Ge inhomogeniety, particularly the HWCVD films, which is consistent with the larger Q_{SANS} values in Table III.

The polymorphous films are clearly inhomogenous compared the standard PECVD a-Si:H. The SAXS shows a small concentration of nanovoids and a significantly larger Q for the deuterated sample, while the Q_{SANS} is smaller for the deuterated film. The SANS shows quite large scattering objects that cannot be well fitted with our current distribution program. More polymorphous samples have been studied by SAXS and discussed in a later section. Further work is needed to understand this material.

Finally, the SANS from the one a-SiC:H alloy is also difficult to interpret. The data shown in Fig. 4 suggest a high incoherent background around 0.2 $cm^{-1}str^{-1}$, but this is not expected on the basis of the measured H content of 25 at.% (Table II). Even though this is quite high, the theoretical value is 0.08 $cm^{-1}str^{-1}$ from Eq. 5. We interpret the extra scattering at high q to a high density of very small scattering features about 1 nm in diameter as indicated in Table III. This is typical for a-SiC:H alloys as found earlier [1], and attributed to nanovoids induced by incorporated CH_3 groups. However, the EPMA found only about 1 at.% C in this sample (Table II). There is also strong low-q scattering, indicating significant larger-scale features as well.

3.2 Medium Range Order and Microcrystallinity Studies

3.2.1 Materials near the boundary between amorphous and microcrystalline

Medium range order (MRO) and the formation of microcrystallites in a-Si:H prepared by PECVD and HWCVD have been probed by systematic x-ray diffraction studies with films as thin as those used in solar cells. Effects of substrate temperature, hydrogen dilution, film thickness, and type of substrate have been examined. High-hydrogen-diluted films of 0.5 μm thickness, grown using optimized deposition parameters for solar cell efficiency and stability, are found tp be partially microcrystalline (μc) if deposited directly on stainless steel substrates, but are fully amorphous provided a thin (20 nm) n-layer of a-Si:H or μc-Si:H is first deposited on the stainless steel. The latter predeposition does not prevent partial microcrystallinity if the films are grown thicker (1.5 to 2.5 μm) and this is consistent with recently proposed phase diagrams delineating boundaries between amorphous and microcrystalline phases depending on hydrogen dilution and film thickness. The formation of partial μc material is accompanied by sharp drops in V_{oc}.

Analysis of the first (lowest angle) scattering peak of the a-Si:H phase demonstrates that its width, directly related to MRO, is reduced by heavier H dilution in PECVD growth or by increased substrate temperature in HWCVD growth. The narrowest width of fully amorphous material correlates with better solar cell stability and this is not likely related to bonded H content since it is quite different in the optimized PECVD (~10-12 at.%) and HWCVD a-Si:H (~2-5 at.%). Capacitance profiling shows a decrease in deep defect density as growth proceeds further from the substrate, consistent with the XRD evidence of improved order for thicker films. A wide range of MRO apparently exists in the residual amorphous phase of the mixed a/μc material. Details of this research can be found in refs. 3 and 4.

3.2.2 Search for thickness effect on structure of a-SiGe:H

Three films were prepared by PECVD at ECD for study by SAXS. Sample L3165 was a standard device-quality a-Si:H film of total thickness 0.9 μm, sample L3166 was a standard device-quality a-SiGe:H film of total thickness 1.3 μm, and sample L3167 was a multilayer film consisting of five alternating layers of a-Si:H (0.05 μm each) and a-SiGe:H (0.20 μm each), prepared under the same conditions used for the individual films L3165 and L3166, respectively. A comparison of the nanostructure would address the question of whether there is a change in the a-SiGe:H as the film is grown thicker than 0.2 μm. Figure 17 shows plots of the SAXS results from the 3 samples

and the associated size distributions obtained assuming spherical scattering objects. Since the SAXS intensities are presented in absolute units, thickness effects have been removed and a direct comparison is possible. Qualitatively, there appears to be only a small difference between the a-SiGe:H sample and the a-SiGe:H/a-Si:H multilayer. The slight difference at lower q may be due to the a-Si:H contribution. Indeed, the size distribution of the multilayer seems to be a composite of the two individual layers. Any formation of microcrystalline material would be readily obvious by an increased SAXS signal (as documented below for μc-Si:H). Quantitatively, all the results are as follows:

Table V. SAXS results for ECD a-$Si_{1-x}Ge_x$:H films.

Sample	Thickness (μm)	x (via EPMA)	Q_N (10^{24}eu/cm^3)	I_D (eu)	A (eu/nm^3)	<D> (nm)
L3165	0.9	--	0.05	10	0.7	2.9
L3166	1.3	0.36	1.80	64	2.4	1.55
L3167	1.4	0.37	1.66	73	4.3	1.83

It is surprising that the EPMA result for the multilayer (L3167) is higher than for the pure a-SiGe:H (L3166). An expected value would be (based on the relative thicknesses) an average of 80% x 0.36 + 20% x 0.00 = 0.29. However, the larger I_D for L3167 is consistent with the larger average x via EPMA. The thicknesses shown in Table V are from the x-ray absorption and are slightly different than expected from the designed preparation conditions for the a-SiGe. The smaller Q_N for the L3167 is not obvious in the figure but the slightly larger sizes shift the data to smaller q and therefore the integrated SAXS is smaller. (The Q_N does not include the A/q^3 term). It is interesting that these values for Q_N are somewhat smaller than those summarized in a previous comparison of several samples and techniques [28]. The conclusion from this study is that there is no obvious change in the nanostructure of device-quality, PECVD a-SiGe:H when the thickness is increased from 0.2 to 1.3 μm.

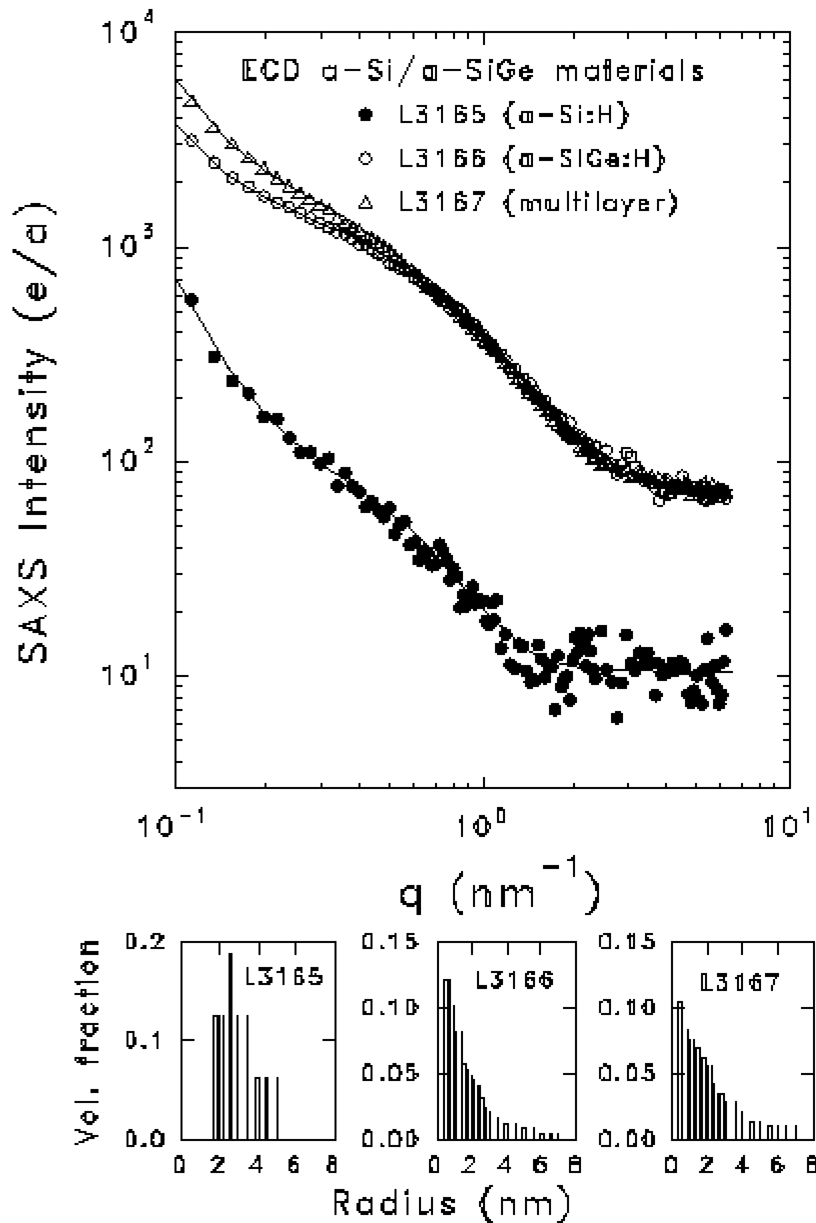

Fig. 17. SAXS data from ECD films and corresponding size distributions used to generate the solid lines through the SAXS data.

3.2.3 a-SiGe:H microcrystallinity and V_{oc}

USSC prepared a series of solar-cell film structures, ss/nip, based on a-$Si_{1-x}Ge_x$:H as the i-layer. The i layers were only about 150 nm thick but good quality XRD patterns were obtained by making long scans. The signal-to-background is also improved due to the higher Z of Ge. Figure 18 shows the XRD patterns from the set of samples after subtraction of the ss substrate signals. The lower series of four samples shows a systematic increase in microcrystallinity and this can be

correlated with decreases in V_{oc} as shown in Fig. 19. Fig. 19a shows the typical behavior of both the energy gap (E_g, Tauc) and the V_{oc} with Ge content, x. The V_{oc} line is based on ref [29], which finds a constant offset of 0.78 V versus x compared to E_g/e. Also shown are the four V_{oc} values from the USSC samples which fall away from this line quite sharply. We suggest that this can be explained by the increases in microcrystallinity as shown in Fig. 19b. We were also able to extract the Ge content in the microcrystals by comparing the lattice constant obtained from the XRD peak position with those known for c- $Si_{1-x}Ge_x$. These results are given in the table below and compared to the x values obtained at USSC by EDS, which will be the average Ge content in the film. The agreement is very good indicating that there is no preferred formation of Si-rich or Ge-rich microcrystals during the deposition.

Table VI. V_{oc} and composition of a/μc-$Si_{1-x}Ge_x$:H

Sample	V_{oc} (V)	x via EDS (film average)	x via XRD of microcrystals
L12860	0.619	0.402	0.4±0.1
L12882	0.584	0.416	0.41 ± 0.06
L12883	0.493	0.455	0.45 ± 0.03
L12884	0.327	0.527	0.53 ± 0.02

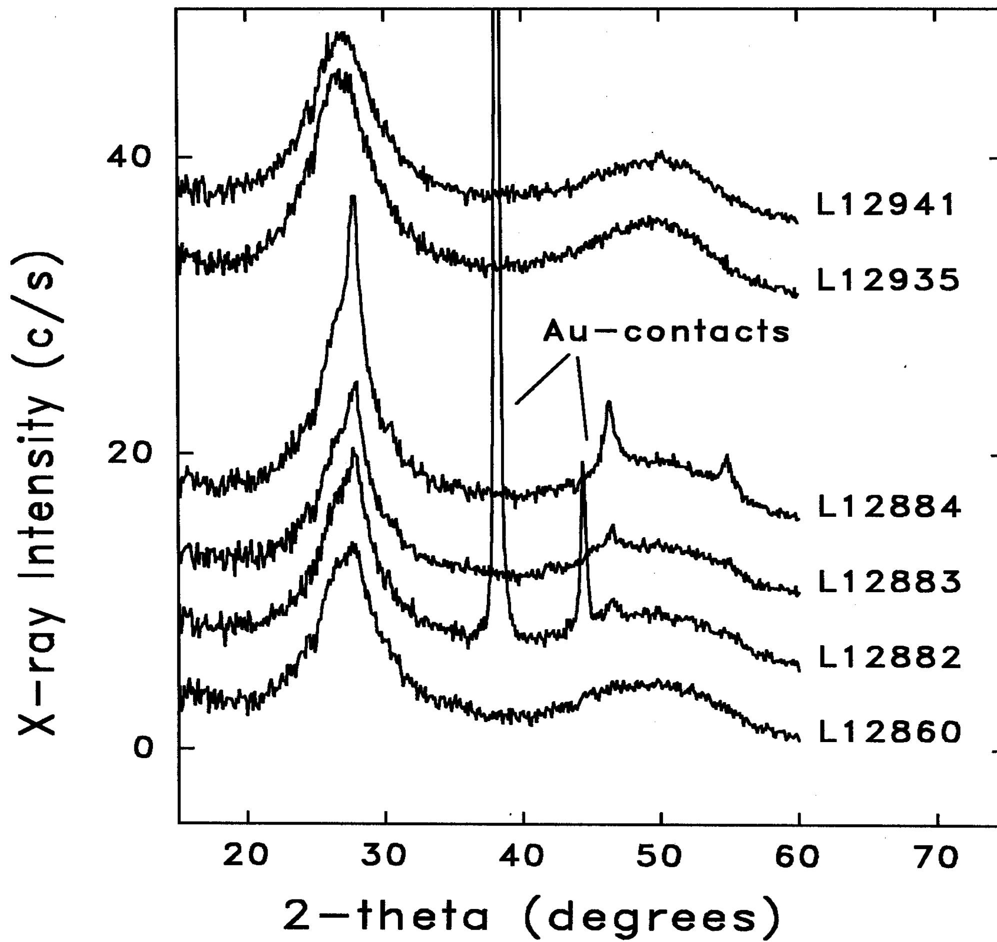

Fig. 18. XRD patterns from USSC ss/nip cell layers with SiGe:H i-layers.

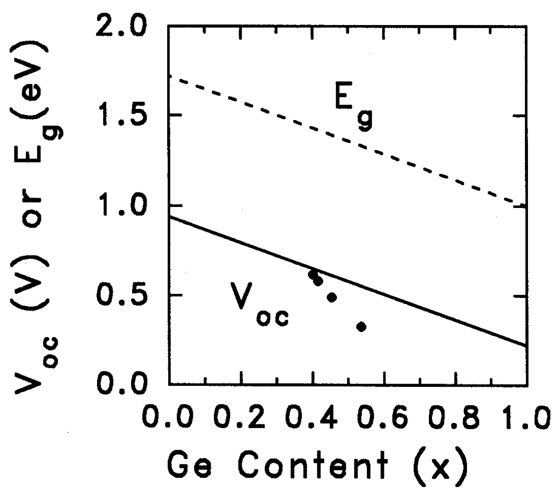

Fig.19a. Band gap and V_{oc} versus Ge content. Solid line based on ref. 29.

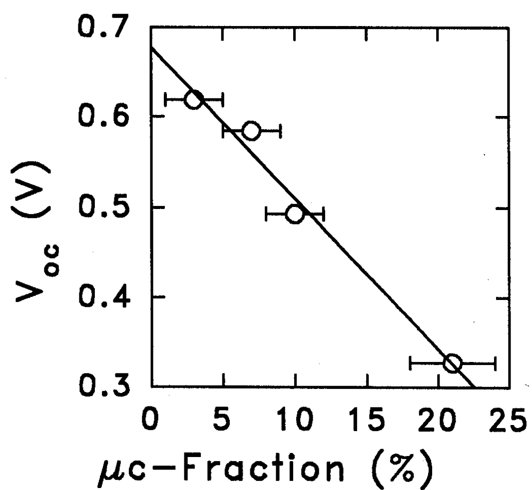

Fig. 19b. Correlation of V_{oc} with microcrystalline fraction.

3.2.4 Search for change in microcrystallinity upon light-soaking

USSC has discovered a light-induced change in V_{oc} of solar cells with an intrinsic layer made of the mixed amorphous/microcrystalline phase. The V_{oc} is significantly *increased* upon light soaking [30]. A first search by XRD of one sample (L13089, ss/nip cell structure) has not detected any change in the degree of crystallinity as summarized below.

Exceptionally long scans were made with the sample carefully mounted in the same place in the XRD system for both states. Figure 20 shows the results of XRD measurements in the light-soaked state and after annealing. The upper graph compares the raw XRD data from the two states (without any subtraction of the ss substrate). One can see clearly the c-Si (111), (220), and (311) peaks. There is no apparent difference between the two states. To look at this more carefully, the lower right graph shows a subset of the same data shown in the top plot, but focussing on the (220) peak. Error bars are included. These data indicates that the light-soaked state peak looks very slightly weaker (but barely outside of the error bars). The sample was also run with twice the density of data points and for a longer time only between 46 and 48 degrees over this (220) peak as shown in the lower left graph. However, these data suggest a slightly stronger light-soaked state peak (again, hardly outside of error). Thus, on average, there is no detectable change between the two states.

In addition, the data in the upper plot was analyzed by subtracting the ss substrate (which causes all the other narrow peaks in the upper graph), and fitting to extract the microcrystalline fraction in the two states (as done in our earlier studies). The results are:

Light-soaked state μc fraction = 8.9 ± 0.9 %

Annealed state μc fraction = 9.3 ± 0.9 %

The width (FWHM) of the a-Si:H first scattering peak was also fitted in the two states:

Light-soaked state FWHM = 4.99 ± 0.05 degrees

Annealed state FWHM = 5.02 ± 0.05 degrees

Thus, there is no evidence for a difference in μc-Si:H fraction in the two states and there is no evidence of a difference in MRO. These values of FWHM are like those of the highest stability cell material reported earlier [3,4]. Recent photoluminesence data from D. Han of the UNC group

suggest evidence of microcrystallinity. Perhaps the changes are localized near the interface, causing significant changes in V_{oc} but undetectable changes in XRD, which samples the entire volume.

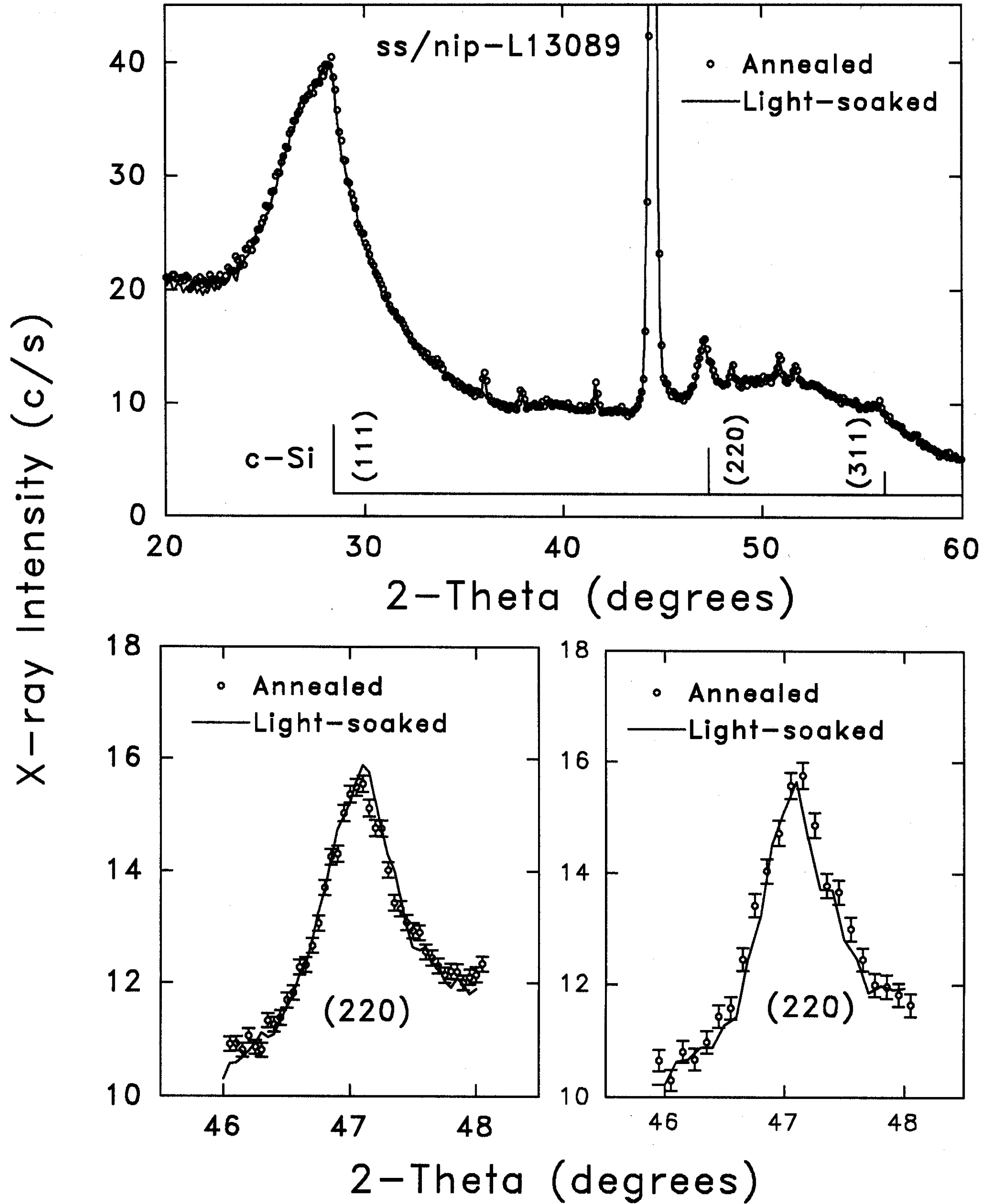

Fig. 20. XRD results from study of USSC L13089 ss/nip cell material in annealed and light-soaked states.

3.2.5 Structural changes in a-Si:H film crystallinity with high H dilution

PECVD films prepared by USSC under different H dilution conditions have been examined by IR, XRD, and H evolution. The high-H-dilution material is deemed "on-the-edge" material because of its observed tendency to be near the boundary between amorphous and microcrystalline states. XRD data show no evidence of microcrystallites in the as-grown state. Upon annealing, a low temperature H-evolution peak appears, and film crystallization is observed at temperatures as low as 500°C, which is far below that observed for a-Si:H films grown without H dilution. Although not detected directly by XRD in the as-grown state, very small crystallites are postulated that catalyze the low-temperature crystallization of the films upon annealing. The large spatial inhomogeneity in the H bonding associated with the very small crystallites is suggested to be one of the reasons for the reduced Staebler-Wronski effect observed in solar cells utilizing the "on-the-edge" material. Details of this research can be found in refs. 31 and 32.

3.2.6 Electronic States/XRD study of high-H-dilution a-Si:H

Thin film n-i-p solar cells were prepared by USSC using decomposition of disilane-hydrogen mixtures by plasma-enhanced chemical vapor deposition. By increasing either the H dilution ratio or the thickness, the i-layer structure showed a transition from amorphous to microcrystalline silicon characterized by XRD. The electronic states of the i-layer were also examined by photoluminescence (PL) spectroscopy, which showed that: (a) below the onset of microcrystallinity, a blueshift of the 1.4 eV PL peak energy along with a decrease of the band width occur as the structural order is improved; (b) above the onset of microcrystallinity, the PL efficiency decreases by a factor of 4-5 and the PL peak energy is redshifted toward 1.2 eV as the μc-Si volume fraction is increased. In addition, the solar cell V_{oc} shows first an increase and then a decrease, correlating with the PL peak energy position. We conclude that the PL spectroscopy, coupled with XRD, is a sensitive tool for characterizing the gradual amorphous-to-microcrystalline structural transition in thin film solar cells. Details of this study are in ref. 33.

3.2.7 SAXS/MRO study of a-SiGe:H alloys

Four samples, one a-Si:H and three a-$Si_{1-x}Ge_x$:H alloys, were supplied by BP-Solar. SAXS and XRD measurements were supplemented by IR (for H content) and EPMA (for x). Figure 21 shows the SAXS data and fits for the 4 samples. There is a systematic increase as Ge is added,

consistent with our typical observations. This trend is also shown in Figure 22 where the integrated SAXS, Q_N, due to nanostructural features, is compared with results from many other Si-Ge alloys. A line has been added to show the trend in the BP-Solar samples. The a-Si:H sample is somewhat higher than the usual value of ~$2x10^{22}$ eu/cm^3 for device-quality material, but the three Ge alloys lie at the low side of the data shown (except for the two USSC microwave alloys which were prepared under high bias).

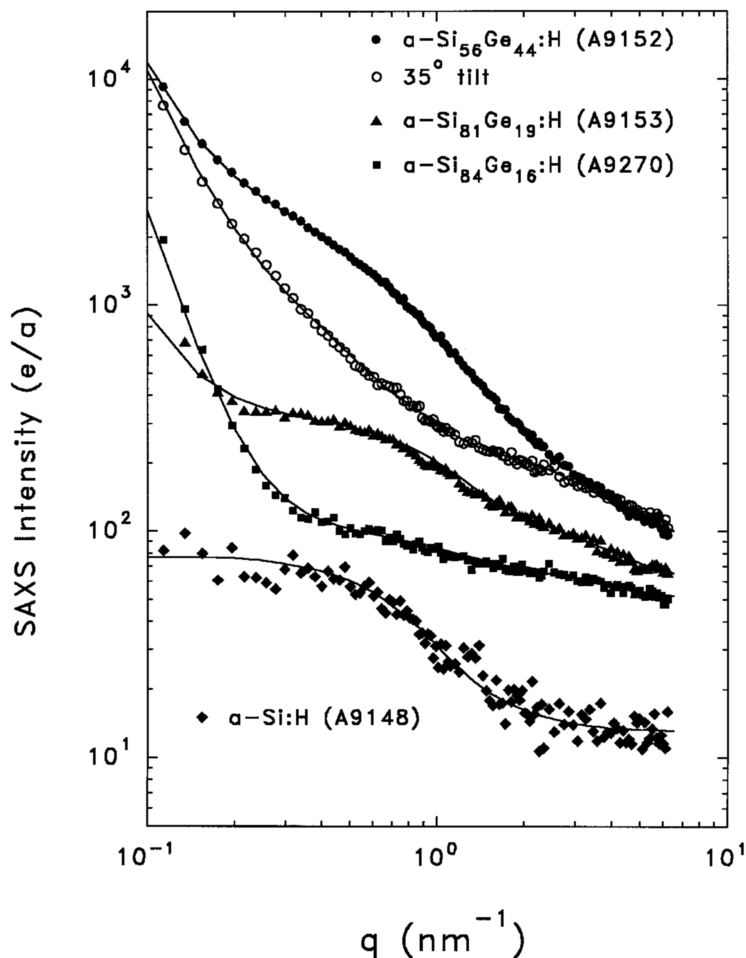

Fig. 21. SAXS data for a-$Si_{1-x}Ge_x$:H alloy films from BP-Solar. Solid lines are fits based on distribution of spherical objects. Tilting data included for one sample.

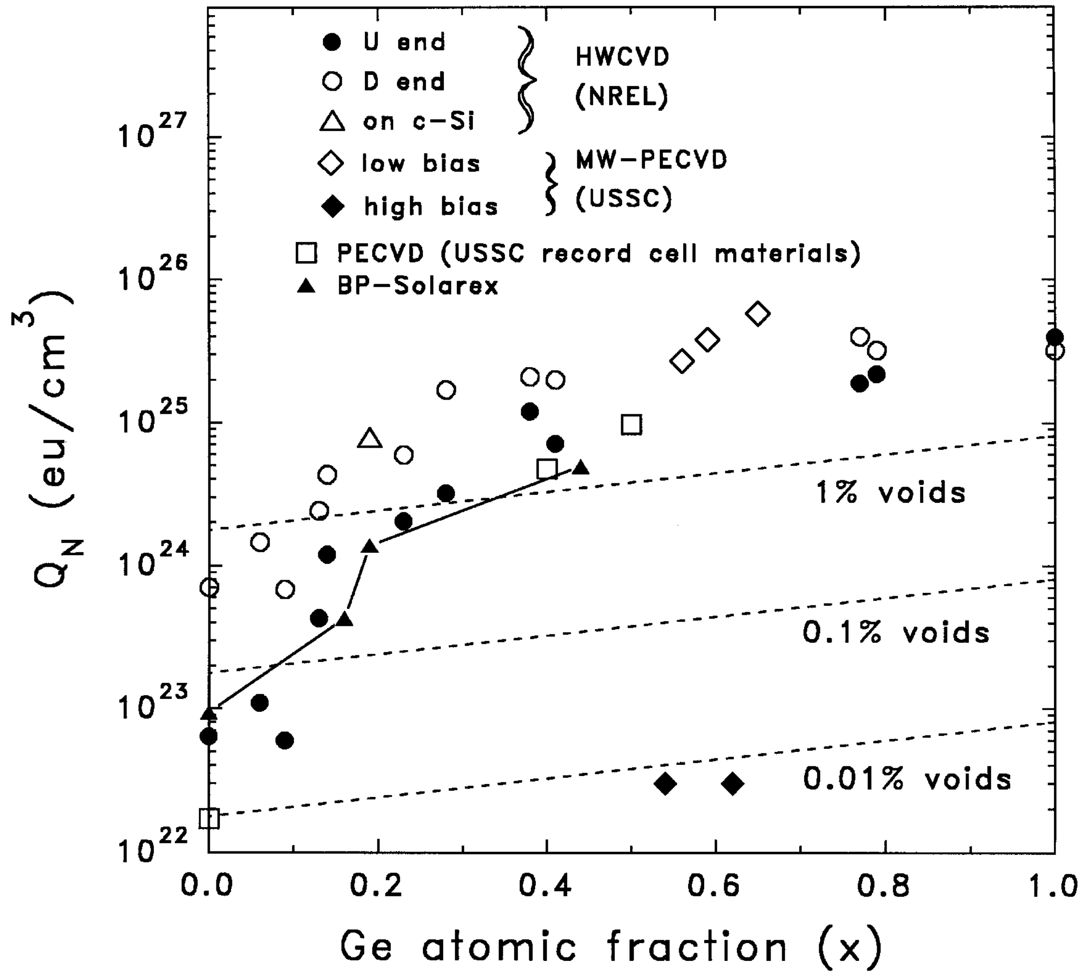

Fig. 22. Survey of integrated SAXS results for a-$Si_{1-x}Ge_x$:H alloys prepared by different groups and methods, highlighting the BP-Solar results.

Table VII summarizes the quantitative information from these samples. The hydrogen content was based on the 640 cm^{-1} IR line. The SAXS data were fitted with a sum of the 3 contributions discussed in reference 1. The large increase in diffuse scattering, I_D, is consistent with the atomic-scale scattering from Si-Ge-H alloys with increasing Ge content. <D> represents the average diameter of spherical objects used to fit the data. These may be nanovoids or Ge composition fluctuations as demonstrated in our ASAXS studies [29,30]. Figure 21 includes SAXS data from a tilting experiment and this clearly demonstrates that the scattering features are non-spherical and oriented with longer axes parallel to the growth direction, a typical observation for Si-Ge alloys [1].

The flotation density of the a-Si:H sample was measured and found to be 2.18 g/cm^3, which is consistent with the 15 at.% H content and a small void fraction.

Table VII. Quantitative SAXS and IR results from BP-Solar films.

Sample	Thickness (µm-via x-ray)	x	$[H]_{IR}$ (at.%)	Q_N (eu/cm^3)	A (eu/nm^3)	I_D (e/a)	<D> (nm)
A9148	2.08	0	15.1	0.09E24	0	13	3.2
A9270	2.56	0.16	14.1	0.43E24	0.4	50	0.6
A9153	1.80	0.19	12.1	1.38E24	0.6	60	1.4
A9152	2.10	0.44	13.0	4.92E24	9.2	87	2.1

(eu = electron units = electrons/atom = e/a)

The same samples that were used for the IR measurements (on c-Si substrates) were examined by x-ray diffraction to look at the medium-range order (MRO). This is our first study of MRO with a-SiGe:H alloys. Since the c-Si substrates used had the (111) orientation (previous work utilized (100) orientation [4]), there was a strong interference of the (111) peak with the first scattering peak (FSP) of the a-SiGe:H. This problem has been minimized by using an asymmetric x-ray diffraction mode to collect the data. The sample is kept at a fixed angle of six degrees relative to the incident beam and the 2-theta scattering angle is scanned. Figure 23 shows data from the 4 samples and the substrate. There is only a small residual contribution from the c-Si (111) peak. The intensities have been corrected with ratios of the thicknesses relative to that of the a-Si:H sample (2.08 µm) One can see the systematic increase in the scattered intensity with x (the higher-Z Ge atoms scatter x-rays more strongly) and even slight shifts downward in peak positions as the average interatomic distances decrease (the dashed lines are included to help see these shifts). Figure 24 shows the results of the analysis of the width W of the first sharp diffraction peak [4] versus Ge content and compares them to the previous ranges of W for a-Si:H materials made by other groups [4]. The MRO seems to be not quite as optimized as in the USSC high-dilution material or the HWCVD high-substrate-temperature material. Figure 24 includes a more recent sample provided by BP-Solar (#A42-1) and a reduced W is found suggesting slightly improved MRO in this sample.

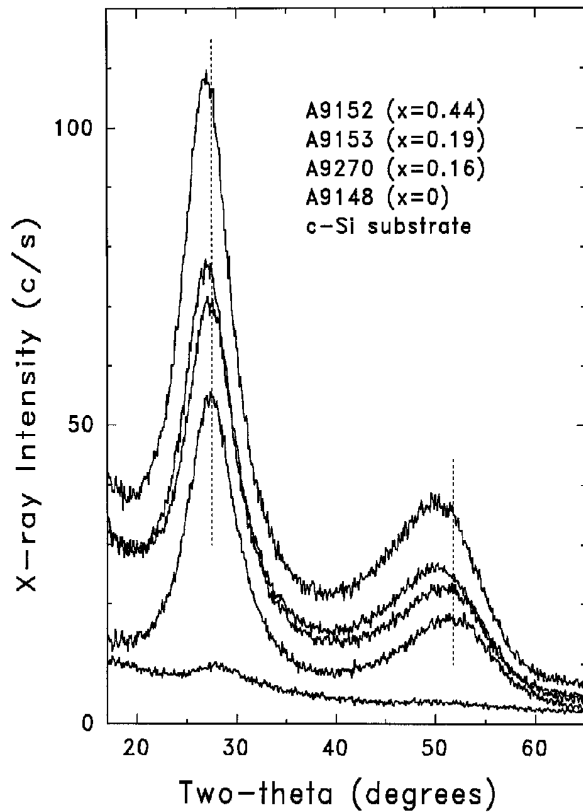

Fig. 23. XRD patterns from BP-Solar a-$Si_{1-x}Ge_x$:H films on (111) c-Si

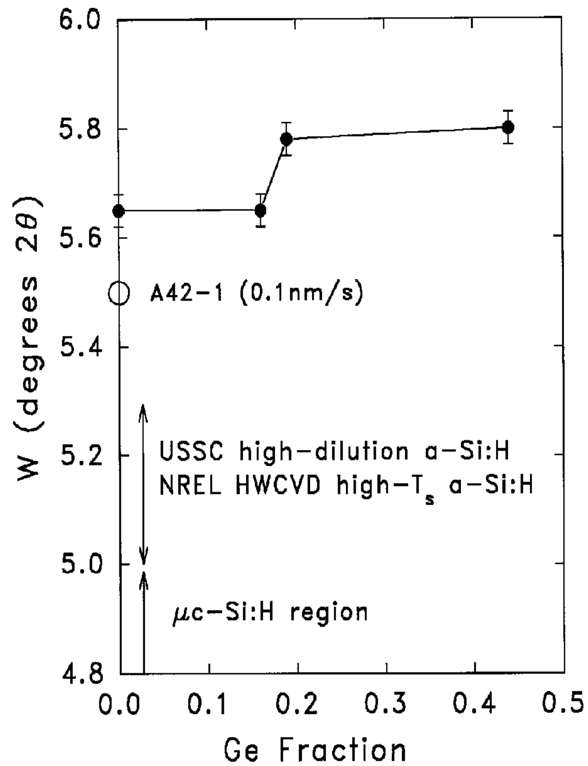

Fig. 24. XRD linewidths of BP-Solar a-$Si_{1-x}Ge_x$:H films on (111) c-Si

3.2.8 Microcrystalline Si:H

Due to increased interest in microcrystalline Si for possible solar cell applications, three sets of such material from different groups were examined by SAXS, XRD, and flotation density

a. *Tailoring the structure of microcrystalline films by biasing the substrate*

Biasing the substrate during deposition and the substrate's surface morphology may both have major effects on the structural properties of thin films. Combined structural investigations (Raman, FTIR, XRD, and SAXS) were made of films prepared at low temperature (325°C) by electron-cyclotron resonance (ECR) CVD. The films were prepared at the Hahn-Meitner Institute (HMI). The bias of the substrate ranged from 0 to +45 V. For stainless steel substrates with an artificially enlarged surface roughness (smart substrates), an increase of crystallinity was observed with Raman spectroscopy. Films prepared under a substrate bias of +15 V exhibited a texture inversion of preferential (220)- to (111)-oriented grains, which was accompanied by an increase in

grain size from 18 to 42 nm. SAXS revealed the films to exhibit significant microvoid fractions. The ability of tailoring the structure of thin Si films by applying a bias is discussed in terms of controlling the energy and intensity of ion flux to the surface of the growing film. This can efficiently be achieved in an ECR system, where the average mean free path of the gas particles exceeds the thickness of the plasma sheath. Details of this study are given in ref. 34.

b. *Microcrystalline Si:H by the Gas Jet Technique*

Four samples of μc-Si:H prepared by the gas-jet technique developed at ECD [35] were examined by SAXS. The silane flow was increased from 15 to 45 sccm for the series of samples and the integrated SAXS was found to decrease systematically from a high value corresponding to about 11% voids to a value for about 1.5% voids. This is consistent with an expected trend of decreasing amounts of microcrystalline material with increasing gas flows [35]. This was confirmed by XRD. The scattering features are only about 2 nm in diameter and show a relatively weak tilting effect. Table VIII provides the quantitative SAXS results. We find that the integrated SAXS from the lowest flow sample is comparable to the large values from the HMI μc-Si:H.

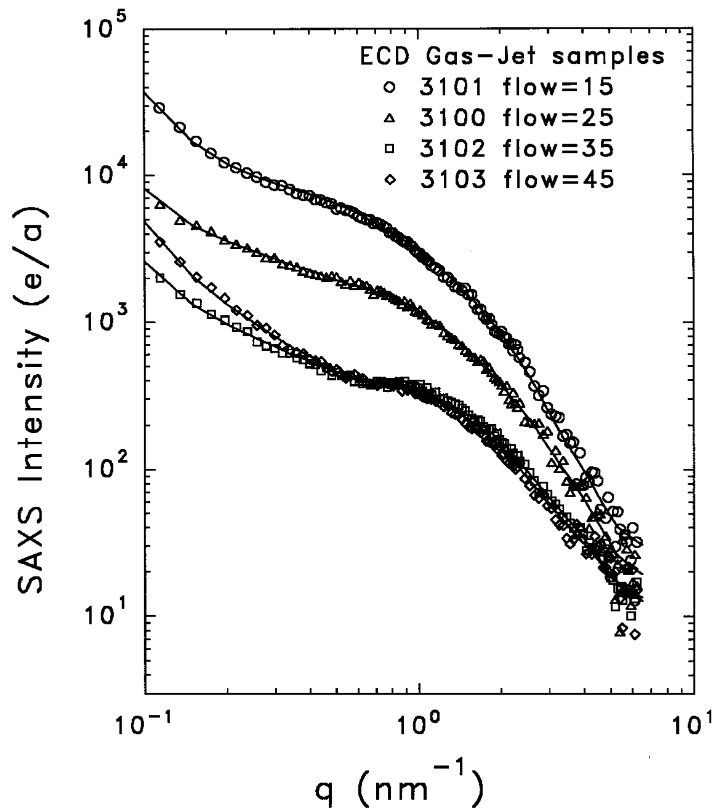

Fig. 25. SAXS data from ECD gas-jet microcrystalline films made under different gas flows.

Table VIII. Quantitative SAXS results from ECD gas-jet μc-Si:H.

Sample	flow	Thickness (μm)	Q_T(eu/cm^3)	Q_N(eu/cm^3)	A(eu/nm^3)	I_D(eu)	<D>(nm)
GJ3101	15	0.21	17.3E24	16.4E24	28	10	2.8
GJ3100	25	0.35	7.20E24	7.04E24	5.0	11	2.3
GJ3102	35	0.63	2.60E24	2.54E24	1.8	8	1.8
GJ3103	45	0.70	2.44E24	2.31E24	4.0	10	1.9

(eu = electron units = electrons/atom = e/a)

Other details of this study, including device properties, can be found in ref. 36.

c. *Microcrystalline Si:H prepared by HWCVD*

Four films of μc-Si:H prepared by the HWCVD method at the Institute of Physical Electronics (IPE) of the University of Stuttgart have been examined by SAXS. Quantitative results are listed in Table IX. This series was made as a function of deposition pressure and yielded a minimum in the integrated SAXS at the intermediate value of 40 mTorr. The corresponding void volume fractions range from 11 to 6 %, again very high and apparently typical of microcrystalline material (compare with Table VIII). The sizes of the scattering features range from 6 to 9 nm and clear, but relatively weak, tilting effects are observed. X-ray diffraction patterns were also measured from the same films used for the SAXS and the preferred orientation (PO) is included in Table IX.

Table IX. Quantitative SAXS results from IPE HWCVD μc-Si:H

Sample	Pressure(mTorr)	t (μm)	Q_N (eu/cm^3)	A (eu/nm^3)	I_D (eu)	<D> (nm)	XRD (PO)
M002162	400	2.1	1.67E25	60	9	9.4	(220)
M002171	100	2.2	1.23E25	30	7	6.8	(111)
M002182	40	2.4	1.00E25	30	4	5.7	(111)
M002172	10	2.5	1.36E25	60	5	5.7	(220)

M002162 tilt ratio $Q(0^o)/Q(35^o) = 2.3$
M002182 tilt ratio $Q(0^o)/Q(35^o) = 2.3$

The I_D parameter is related to the amount of H dispersed on the atomic scale in the samples. The values in the table are consistent with rather low H contents typically seen in HWCVD samples grown at the typical elevated temperatures of about 360° or higher (< 7 at.%). There also seems to be a trend of decreasing I_D with increasing sample number as listed in the table. However, these

values are quite uncertain since it is based on the data at high q where there is more scatter in the data.

3.3 RF-PECVD versus VHF-PECVD Comparison at Higher Deposition Rates

The advantage of using very high frequencies for preparation of a-Si:H materials at high rates (above 5 Å/s) for intrinsic layers (i-layer) of solar cells has been well documented. In an effort to identify film properties which may be related to this superior device performance, a study of the structural, optical and electrical properties of films made at various deposition rates between 1 and 15 Å/s using rf frequencies of 13.56 and 70 MHz has been made. The films were characterized using a number of techniques including SAXS, infrared absorption spectroscopy, and scanning electron microscopy. For the films made using the 70 MHz frequency, the amount of nanovoids with sizes of < 100Å increases systematically as the deposition rates increases beyond 5 Å/s. Accompanying the increase in void fraction in the films are increases in the hydrogen content and the amount of 2070 cm^{-1} mode in the infrared absorption spectra. In addition to an increase in the amount of nanovoids in the films as the deposition rate exceeds 5 Å/s, the films made using the 13.56 MHz and high deposition rates have large amounts of SAXS related to scattering features with sizes > 200 Å. This scattering is associated with large bulk density fluctuations and/or enhanced surface roughness. None of the films in the study displayed signs of having columnar-like microstructures. The nanovoids are not related to changes in the solar cells with increasing i-layer deposition rate for both fabrication processes, perhaps due to the relatively small volume fractions of less than 0.2% and/or good void-surface passivation. However, the larger-scale structures detected in the films made using the 13.56 MHz technique could cause poorer performance in cells prepared at high growth rates. Details of this study are presented in ref. 37.

3.4 HWCVD a-Si:H

3.4.1 NREL ultra-high-rate HWCVD a-Si:H

NREL has developed modifications of a HWCVD processing system to allow extremely high deposition rates of up to 1 μm/min (17 nm/s) [38]. This material maintains a photoconductivity-to-dark-conductivity ratio of 10^5 up to 13 nm/s. Numerous samples have been prepared by NREL for SAXS and XRD studies. Figure 26 shows typical SAXS results from the two extremes of deposition rates from samples made in the "L" system. The integrated SAXS due to nanostructural features (whose size distribution is shown in the inset) from the 13 nm/s sample is about two orders-of-magnitude larger than that from the 1.5 nm/s sample. Figure 27 summarizes the integrated SAXS values from all the HWCVD samples examined. Predicted signals due to various void volume fractions are also indicated. Note the sharp increase in SAXS between 1.5 and 3 nm/s. This dramatic change is not associated with a change from the use of 1 to 2 filaments but rather from simply the increased rate. Note from Fig. 27 that the variation of substrate temperature can induce significant changes in the SAXS at a fixed deposition rate (11 nm/s here). We point out that the data for the ECD samples deposited at higher-than-normal rates described above all fall into the range below $Q=6x10^{23}$ eu/cm^3 at the far left (below 1.5 nm/s) in Fig. 27.

Figure 28 summarizes the average radius of the scattering features, typically in the range of 2 to 4 nm. We emphasize that this radius actually represents the smaller dimension of elongated scattering centers since the tilting experiments with these films all show relatively strong tilting effects. The latter are consistent with ellipsoids with long dimensions about 3 to 10 times the size shown in Fig. 28. This indicates a residual columnar-like microstucture, with elongated microvoids likely along the column boundaries.

The x-ray linewidth of the first scattering peak is remarkably constant and indicates little change in MRO between 1.5 and 14 nm/s. The widths observed are somewhat higher than the narrowest values reported earlier [4] suggesting some deterioration in MRO compared to the best quality PECVD and HWCVD films. However, Raman measurements also indicate no change in the short range order (SRO) as the rate is increased. Detailed discussion of the ultra-high-rate HWCVD data has recently been published along with possible reasons for the invariance in MRO and SRO with increased deposition rate in terms of growth models, as well as a possible explanation why the clear increase in microvoid density found by SAXS apparently does not play any role in the Staebler-Wronski effect for this type of material [39,40].

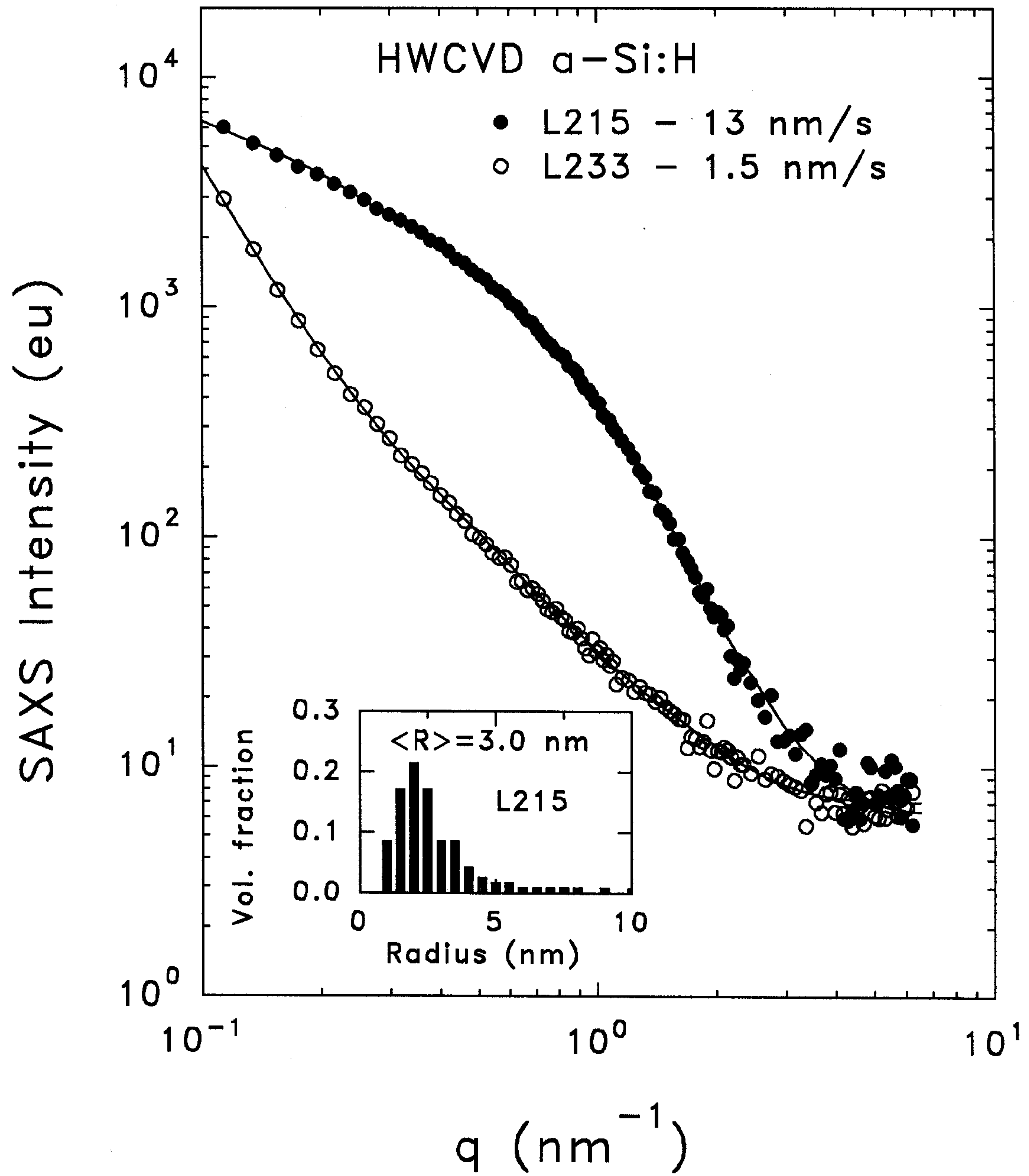

Fig. 26. Typical SAXS data from HWCVD films made at low and ultra-high deposition rates. Inset shows size distribution of spherical objects yielding the solid-line fit to the L215 SAXS data.

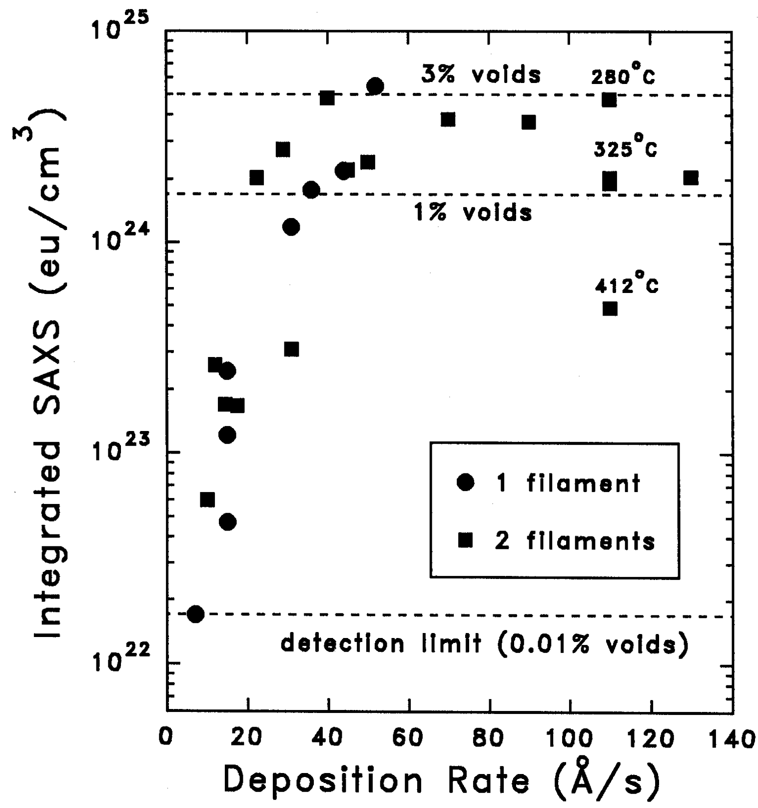

Fig. 27. Summary of the integrated SAXS from nanostuctural features (Q_N) of HWCVD a-Si:H grown up to ultra-high deposition rates. Q_N's due to various void volume fraction are indicated.

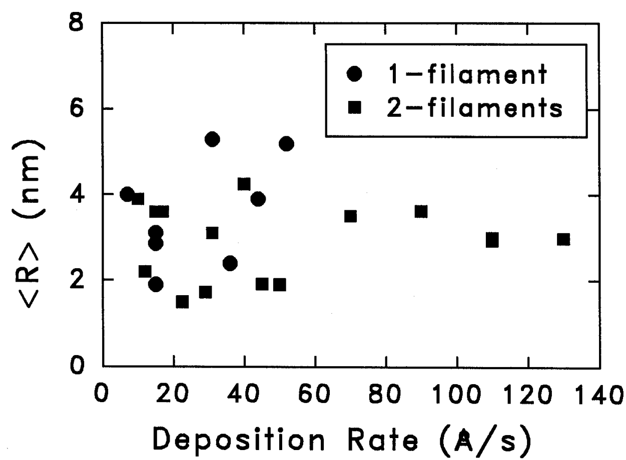

Fig. 28. Summary of average radii obtained from fits of spherical size distributions to HWCVD a-Si:H SAXS data.

3.4.2 PECVD vs HWCVD films prepared by MVSystems

Figure 29 compares SAXS from the two MVSystems (MVS) films prepared by PECVD and HWCVD and one can see dramatic differences. The solid lines are fits to the data based on the sum of contributions $I_L + I_N + I_D$, as described in a review paper [1] due to larger scale structure, nanoscale structure, and atomic-scale composition fluctuations, resp. Qualitatively, the HWCVD sample is dominated by larger-scale structure as seen by the continuously rising signal as q becomes smaller, while the PECVD sample has no detectable larger-scale structure since the signal seems to saturate at smaller q. The background diffuse signal (I_D) is larger for the PECVD and this is attributed to a much higher bonded H content is this sample. In fact the very low I_D for the

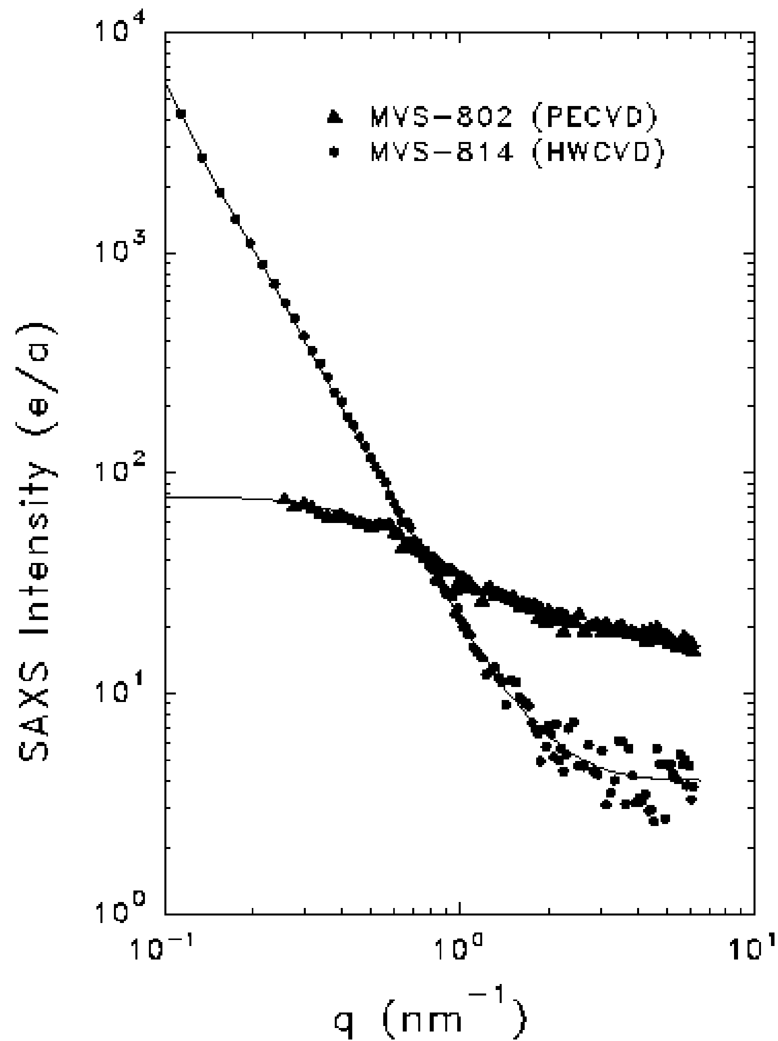

Fig. 29. SAXS from MVSystems films made by PECVD and HWCVD.

HWCVD sample indicates quite a low H content and therefore a high substrate temperature. This is consistent with the fact that we detected weak microcrystallinity in the HWCVD film via X-ray diffraction measurements. This was likely induced by interdiffusion-induced crystallization caused by the Al substrate. We have established that substrate temperatures near or above 450°C can cause this effect. Table X presents a summary of the quantitative results from fitting the SAXS data. The volume fractions of nanovoids are quite small but significantly larger than our detection limit of 0.01%.

Table X. SAXS results from MVSystems samples

Sample	Dep. Method	t_p (μm)	t_x (μm)	Q_N (10^{23}eu/cm^3)	f (vol.%)	<D> (nm)	A (eu/nm^3)	I_D (eu)
MVS802	PECVD	1.9	3.61	2.4	0.14	1.2	0	15
MVS814	HWCVD	2.1	3.55	1.1	0.06	8.6	5.5	4

t_p = thickness provided by MVS;
t_x = thickness determined by x-ray absorption;

3.4.3 High-pressure experiment

At the request of the UCLA group, two SAXS samples were supplied for a high pressure experiment. These were HWCVD a-Si:H films on 10 micron Al foil, folded into 8 layers:

T840 - low substrate temperature, relatively high void fraction (about 2 vol.%)

T905 - high substrate temperature, very low void fraction (about 0.02 vol.%)

A SAXS-reference Al-substrate foil was included in the high pressure treatment of the above samples. Figure 30 is a plot of the SAXS data comparing the intensities before and after the high pressure treatment (subjected to 3 kbar and released, repeated four times). The lower plot shows the ratios of the after/before intensities. It appears that there is no detectable effect. Quantitatively, the average ratio for T840 (the one with a high void density) is 1.005. The average for T905 is 0.939 but this includes many data points at high q which have large error bars due to the very weak signal. Averaging the first 45 points ($q < 1.0$ nm^{-1}), then the average is 0.983. Since both of these samples show a significant tilting effect, such small changes (difference from unity) are readily explained by not having the sample in exactly the same position in the SAXS system before and

after the treatment. Thus, there appears to be no evidence for a residual microvoid collapse after pressure treatment at 3 kbar. The UCLA group had postulated such a collapse to explain some irreversible electronic behavior after such a treatment.

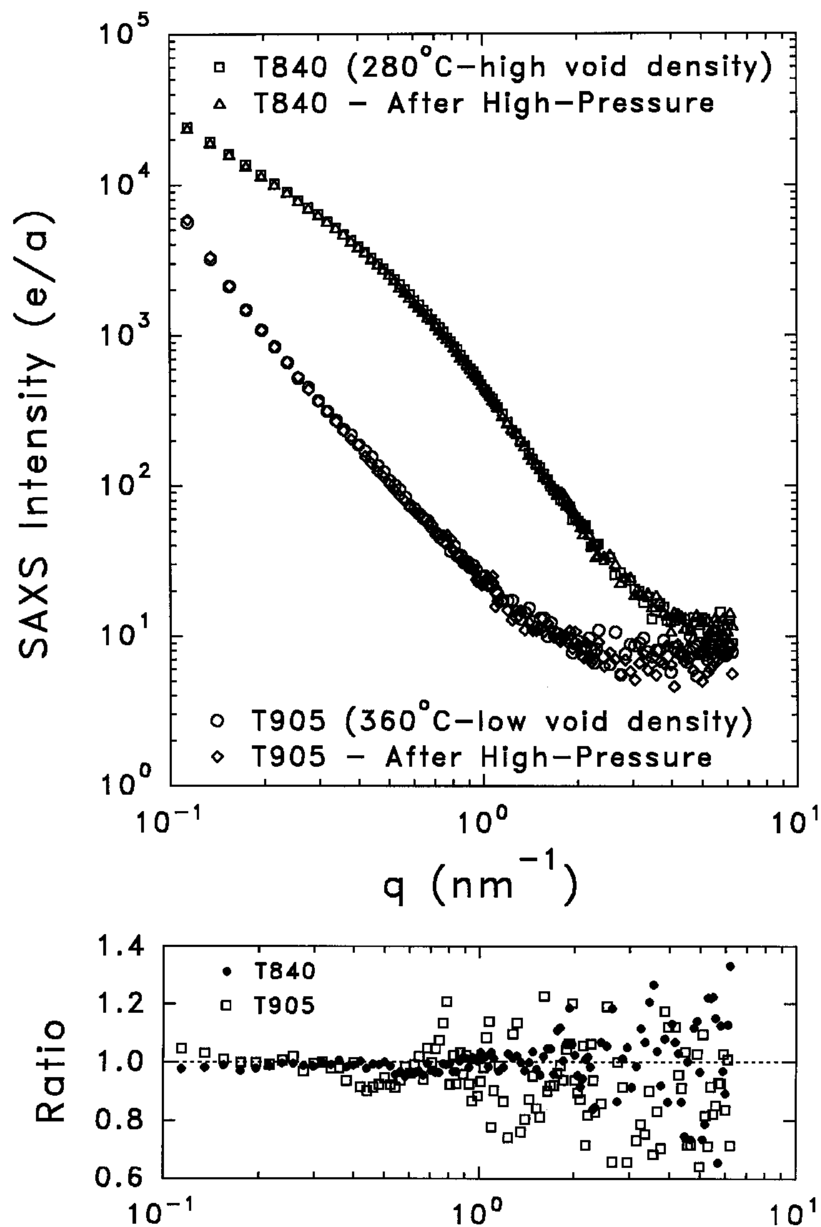

Fig. 30. (upper) SAXS data before and after a 3 kbar high-pressure treatment on two HWCVD films with different void content. (lower) Ratios of after/before intensities.

3.5 ASAXS Experiments and Analyses

From extended anomalous-SAXS (ASAXS) measurements at numerous x-ray energies, structural and physical properties such as non-uniform Ge-concentrations and – in combination with flotation density results – the densities of Ge-enriched regions in amorphous a-$Si_{1-x}Ge_x$:H alloys were deduced based on a two-phase model [41]. This extends our first study of these alloys by ASAXS [42]. Depending on the preparation technique (with and without H dilution of the source gases), a dense phase with volume fractions of about 90% and with Ge-enrichments only slightly higher with respect to the entire alloy were observed. These denser regions with average sizes between 10 and 23 nm can be interpreted as a phase containing slightly enhanced numbers of homopolar Ge-bonds, surrounded by a small volume fraction phase of low density, H-rich regions containing much less Ge (sometimes none) with averages sizes from 0.6 to 1.6 nm [41].

More recent ASAXS research has compared a-$Si_{1-x}Ge_x$:H alloys made by HWVCD at NREL with PECVD high-efficiency solar cell material made at USSC [43]. The results from the HWCVD alloys reveal clear evidence of non-uniformly distributed Ge with correlation lengths between 0.8 and 1.1 nm. For these alloys the amount of separated scattering shows a systematic increase with Ge concentration due to increasing Ge inhomogeneity. From the comparison of HWCVD and PECVD material it was found for similar x that the HWCVD technique causes a larger amount of inhomogeneity on a length scale smaller than 20 nm and the opposite for larger inhomogeneities. Details of this study can be found in. ref. 43.

Since we have always typically observed strong SAXS from the a-$Si_{1-x}Ge_x$:H alloys, it is of interest to examine how much of the SAXS total signal comes from the Ge non-uniformity. Figure 31 documents this fraction for several of the alloys studied. These results make it clear that 30 to 50% of the SAXS signal is due to the Ge composition fluctuations. To our knowledge, near uniform alloys are made only by applying a bias to the substrate during deposition to induce ion bombardment and promote uniformity. Unfortunately, such bombardment also introduces other defects that apparently degrade the opto-electronic and device performance. However, a systematic optimization of such bombardment has not been done to our knowledge.

In an attempt to more directly detect the Ge non-uniformity in the a-$Si_{1-x}Ge_x$:H alloys, a novel annealing/crystallization experiment has been tried. Films were annealed to crystallization and then examined by XRD to search for evidence of different lattice parameters associated with crystals of different composition. Two distinct phases of c-$Si_{1-x}Ge_x$ (Si-rich and Ge-

rich) have been observed in several films, but this is attributed to a metallurgical reaction with the Al-foil substrate, details of which are still under study. One film on c-Si substrate showed no such evidence of two phases after crystallization. We suspect that the scale on which the non-uniformity occurs (~ 1nm) may prevent detection by XRD. High resolution TEM studies are in order.

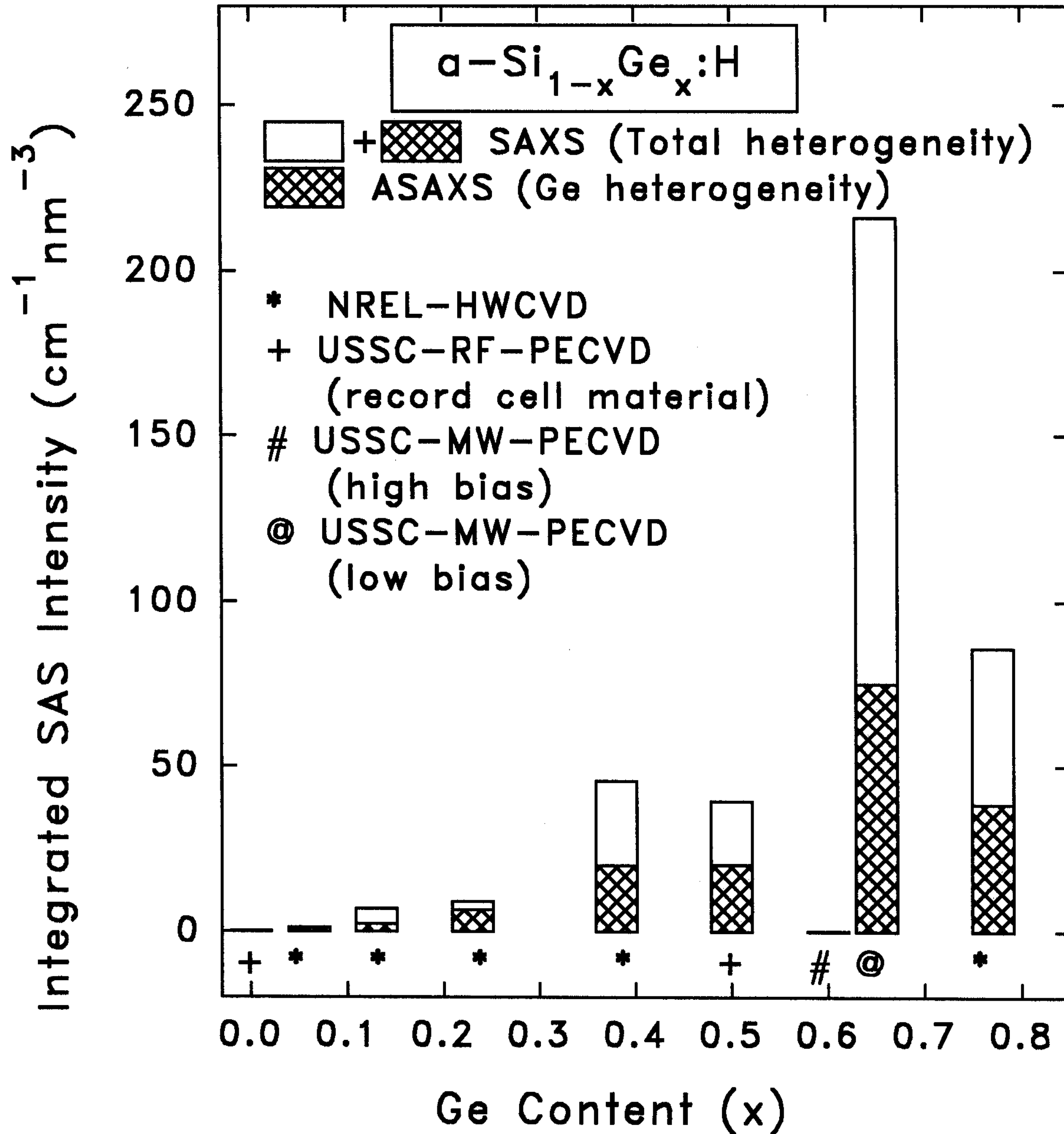

Fig. 31. Comparison of SAXS and ASAXS integrated intensities from several alloys made by different methods.

A novel method to search for the Ge non-uniformity was developed near the end of the project during the contract extension period. If the a-SiGe:H could be annealed to crystallization at a low enough temperature such that little or no diffusion of the Si and Ge occurs, then the resulting polycrystalline material should inherit the inhomogeneity. This might be detected by XRD via diffraction peaks that are shifted or broadened. The lattice parameters of c-Si and c-Ge are different enough that some resolution of peaks may occur due to different Ge contents in different crystals. This approach was tested with a set of six a-SiGe:H alloys that had previously been characterized either by SAXS, ASAXS or both. Four of the samples shown in Fig. 31 and two of the SANS samples (UH3 and NH5) were selected, with Ge contents as listed in Table XI.

Table XI. a-$Si_{1-x}Ge_x$:H samples for crystallization/XRD study.

Sample ID	Ge content (x)	Preparation Technique
U74 (NREL)	0.38	HWCVD on Al-foil
U104 (NREL)	0.79	HWCVD on Al-foil
MW2303 (USSC)	0.62	Microwave PECVD (high bias) on Al-foil
MW2304 (USSC)	0.64	Microwave PECVD (low bias) on Al-foil
UH3 (USSC)	0.405	PECVD on c-Si
NH5 (NREL)	0.15	HWCVD on c-Si

Each sample was annealed under flowing high-purity Ar in 50°C steps for one hour beginning at 400°C. XRD was done after each step to detect the onset of crystallization. All samples were fully amorphous in the as-deposited state. No crystallization was found in any of the samples after a 400°C anneal. Only the U104 sample showed partial crystallization after 450°C and all the films on Al-foil were crystallized after the 500°C anneal. The UH3 sample on c-Si did not show any crystallization until 600°C and the NH5 sample on c-Si was completely flaked off from the annealing and so was not investigated.

Interestingly, all the samples on Al foil showed evidence of two well-defined crystalline phases that were Ge-rich and Si-rich after crystallization. Figure 32 shows the series of XRD patterns obtained from U74.

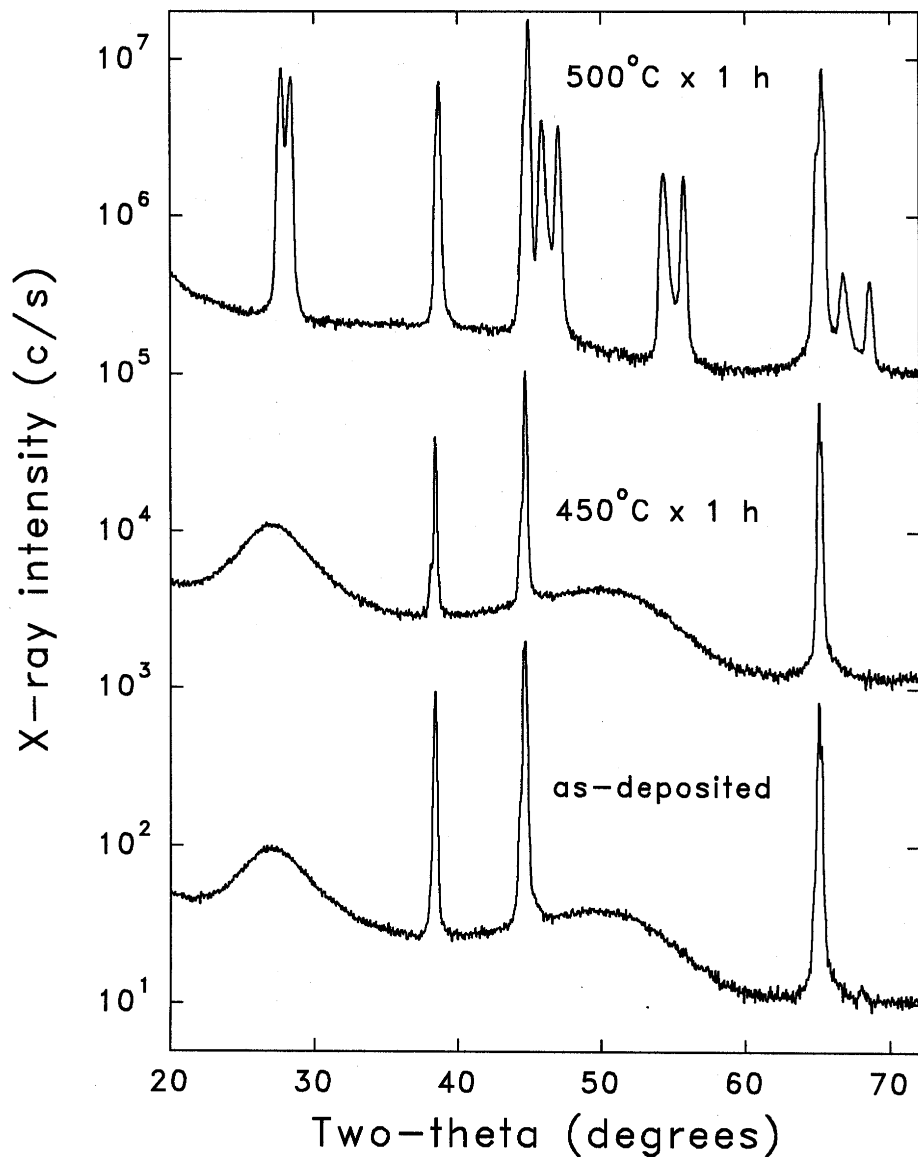

Fig. 32. XRD patterns from HWCVD a-SiGe:H alloy before and after annealing-induced crystallization.

From the as-deposited film data one can see the broad a-SiGe:H scattering peaks near 28° and 51°, together with the sharp Al-foil substrate peaks. There is no apparent change after the 450°C anneal. New peaks replace the a-SiGe:H pattern after the 500°C anneal but each appears as a "doublet" at about the positions expected for the (111), (220), (311), and (400) peaks of c-$Si_{1-x}Ge_x$ with x=0.38, the average Ge content in this sample. Detailed analysis of each of the peaks yields a Si-rich phase

with x=0.23 and a Ge-rich phase with x=0.83. At first this appear to be clear direct evidence of non-uniform Ge alloying in the amorphous state. However, all the results taken together make this evidence suspect. Here are the results causing suspicion: (i) all the XRD from the films crystallized on Al-foil show the phase separation as observed in Fig. 32, even for sample MW2303 which, according to the ASAXS, is *uniform* in Ge distribution due to the high bias during deposition [42]; (ii) the sample on c-Si (UH3) does not show the "doublet" structure after crystallization, but just somewhat broadened peaks at positions corresponding to average Ge content. Thus we conclude that there is some type of reaction with the Al-foil substrate that is inducing the phase separation. A careful study of the appropriate phase diagram is underway to help explain our observations. This reaction may be of interest in other applications of Si-Ge alloys with Al contacts. The Al-induced crystallization of a-Si:H is a well-known phenomena [44] and has recently received interest for producing poly-Si at low temperature [45]. There have been no studies to our knowledge of Al-induced crystallization of a-SiGe:H, the phenomena we apparently have observed here.

3.6 Polymorphous Si:H

SAXS measurements have been completed for a series of a-Si:H samples that are designated as "polymorphous" (pm) to describe an unusual type of a-Si:H made at the Ecole Polytechnique [46]. This material apparently contains significant amounts of crystalline clusters imbedded in the amorphous matrix and evidence is found for improved transport properties and enhanced stability [46-48]. Figure 33 shows the SAXS data and fits. The SAXS is mostly composed of a Porod term (A/q^3) and a diffuse term (I_D =constant vs q) for all samples. The Porod

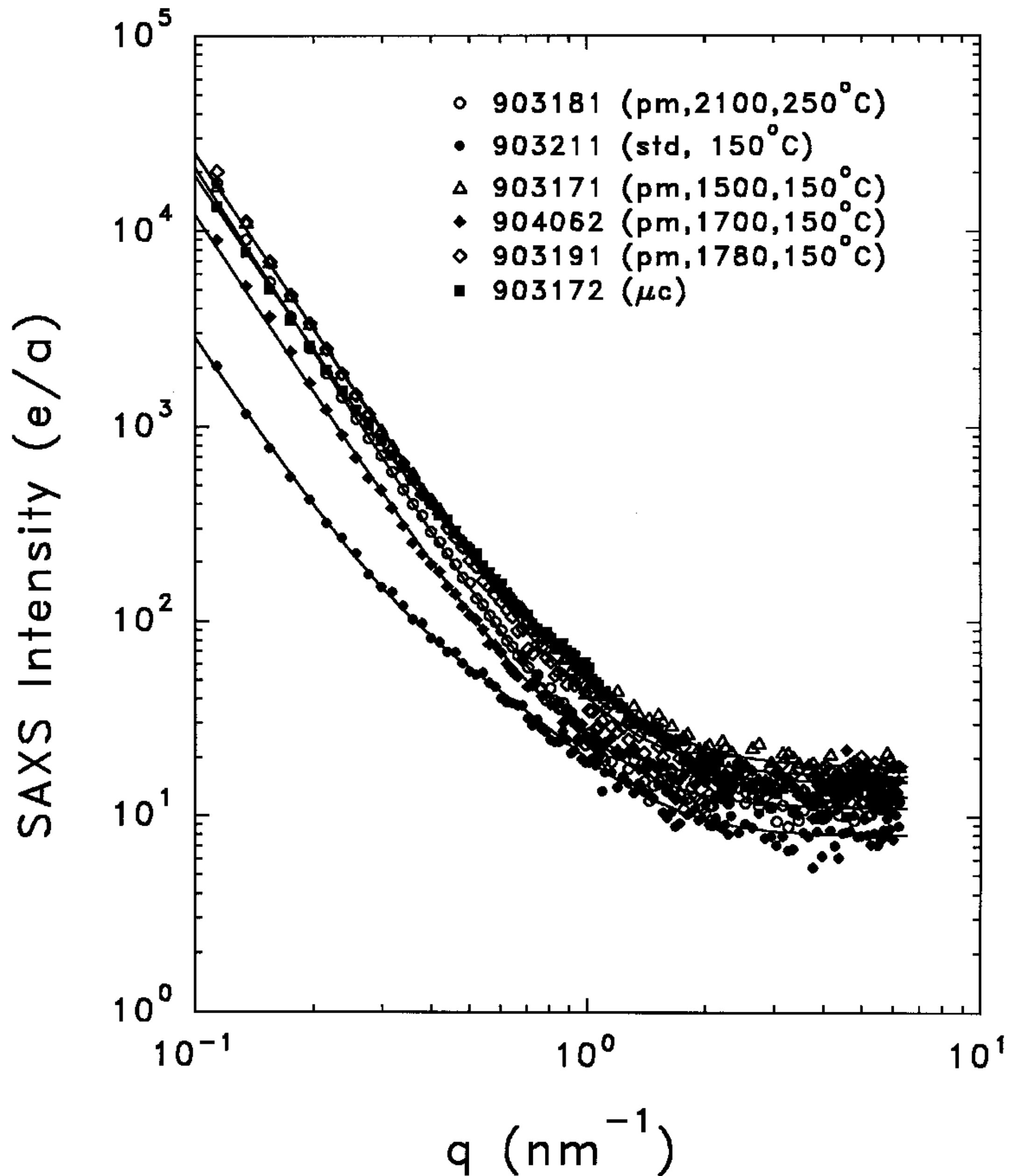

Fig. 33. SAXS data from Ecole-Polytechnique polymorphous (pm)-Si:H, standard a-Si:H, and partially microcystalline (μc)–Si:H.

scattering is due to some larger-scale structural features at least 20 nm in size. This could be surface-roughness related since the SAXS from the two samples deposited on c-Si substrate have much reduced A/q^3 terms. Differences in I_D (see range of intensity levels at high q) are likely related to differences in bonded H content. The SAXS due to any nanostructural features (< 10 nm) is extremely weak. Only samples 903171, 903211, and 903172 show a component (Q_N) slightly larger than the detection limit of $Q_N = \sim 2 \times 10^{22}$ eu/cm^3 (corresponding to 0.01 vol.% voids). Thus, it is very interesting that there is little or no scattering from the "polymorphous" nature of these films! This may be due to a very small electron density contrast between the incorporated nanocrystals that are seen by TEM [46,47] and the amorphous matrix, and/or due to a very small volume fraction of such nanocrystals (however, Ecole Polytechnique has pointed out that it expects the films to have large volume fractions). We measured XRD on all the polymorphous samples and did not detect any evidence of crystalline Si (111), (220), or (311) peaks. These peaks were detected in 903172 (the sample known to be partially μc) but it was still mostly amorphous.

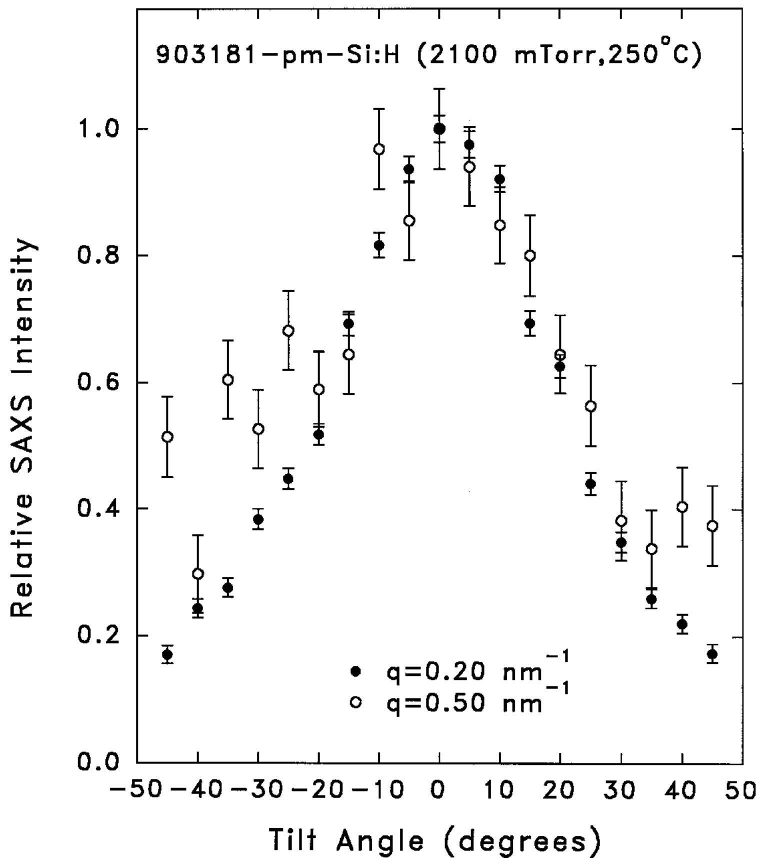

Fig. 34. Tilting data from a polymorphous Si:H film on Al-foil.

Detailed tilting experiments were done on one of the polymorphous samples that was deposited on both Al-foil and thin c-Si suitable for SAXS. Figure 34 shows a strong tilt effect for the film deposited on Al-foil. The intensity was measured at two values of q, one where the SAXS intensity is quite high ($q = 0.2$ nm^{-1}) and one where to intensity is quite low ($q = 0.5$ nm^{-1}). The symmetric drop of intensity by about a factor of 5 at $\pm 45^o$ is consistent with elongated scattering objects aligned with the growth direction (i.e., columnar-like features). This effect makes it difficult to attribute the small q

scattering to surface roughness. Based on ellipsoidal objects, the drop of a factor of 5 can be explained by objects with major-to-minor axis ratios of about 9 that are aligned with the long axis along the growth direction. This would correspond to rather large objects since the scattering is at relatively low q (>10 nm for the minor axis size!). These objects cannot be the nanocrystals expected in the polymorphous material since the TEM studies indicate 2 to 4 nm sizes [46,47] and such crystals would be detected by XRD. Surprisingly, the results from films on the c-Si substrates are quite different as illustrated in Fig. 35. The film on c-Si yields a much lower Porod scattering and there is no detectable tilting effect. This provides strong evidence of a significant substrate effect on the growth and microstructure of the polymorphous material.

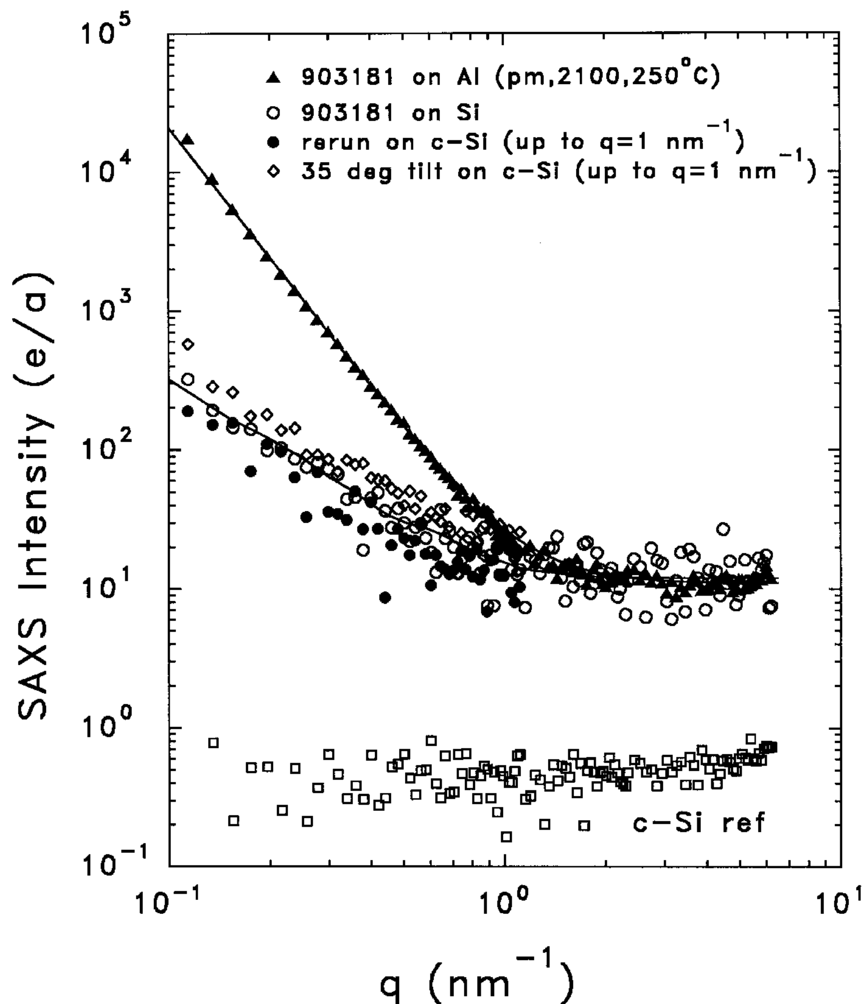

Fig. 35. SAXS data from polymorphous (pm)-Si:H co-deposited on Al-foil and on c-Si. Tilting at 35 degrees cause little change for the film on c-Si.

We also provide results on the density of the polymorphous Si:H. Table XII lists the values obtained by the flotation density method from the same samples used to obtain the SAXS data in Fig. 33. The polymorphous samples are only slightly less dense than the standard a-Si:H and this is likely due to a higher H content consistent with the larger diffuse scattering levels seen for the polymorphous films in Fig. 33. Note the increased density due to the higher substrate temperature used for sample 903181. The observed density deficit relative to c-Si (2.33 g/cm^3) is typical of a-Si:H with 8-15 at.% bonded H [49].

Table XII. Flotation densities of polymorphous, standard, and partially μc Si:H.

Sample	Structure (prep)	Density (g/cm^3)
903211	Standard, fully amorphous a-Si:H (Ts=150°C)	2.201
903172	Microcrystalline Si:H	2.177
903172	Polymorphous Si:H (1600 mTorr, Ts=150°C)	2.180
904062	Polymorphous Si:H (1700 mTorr, Ts=150°C)	2.180
903191	Polymorphous Si:H (1800 mTorr, Ts=150°C)	2.181
903181	Polymorphous Si:H (2100 mTorr, Ts=250°C)	2.228

Studies of polymorphous films have also been done by SANS as presented above in section 3.2. As noted, the combination of SAXS and SANS should lead to a model to explain the heterogeneity of this material. It will be useful to establish whether this material is similar to the "protocrystalline" materials prepared near the edge to micocrystallinity.

3.7 PECVD a-Si:H Prepared with Ar dilution

Device quality a-Si:H and uc-Si:H thin films are usually prepared by rf PECVD with H_2-diluted silane. Recently, by controlling deposition conditions, the group at IACS has been able to deposit improved quality a-Si:H thin films from silane-argon mixtures via 13.56 MHz rf PECVD [50] and to apply the material in single-junction solar cells [51,52]. The use of high power densities also led to good microcrystalline material [53] and a sharp increase in heterogeneity was observed by SAXS just before the onset of the microcrystalline growth [50]. Here we examine additional systematic sets of films prepared under different amounts of Ar dilution and with different plasma powers. Table XIII shows the list of samples and their deposition conditions. Figures 36, 37 and 38

show the SAXS data in various comparison plots. Figure 36 shows a systematic and dramatic increase in the SAXS with increasing plasma power at fixed dilution. Figure 37 shows a similar but less dramatic trend at a lower Ar dilution. Figure 38 shows the increase in heterogeneity with increasing Ar dilution at a fixed plasma power. Figure 39 compares the XRD patterns from several of the samples. The SAXS signals vary by over two orders of magnitude, with the two microcrystalline samples (PLA74 and 75) showing the strongest intensities. The presence of microcrystallinity was also detected in samples PLA71 and 73. Since PLA79 showed no evidence of microcrystallinity, the other (lower power) samples in this 90 sccm Ar series were not measured by XRD. Since PLA70 and 72 were fully amorphous, samples PLA80 and 81 (lower power) were not measured by XRD. Although PLA71 was prepared with less power than PLA73, it shows stronger SAXS and this correlates with a stronger degree of microcrystallinity in this sample. The degree of crystallinity was estimated from the relative areas of the amorphous (broad peaks at 27.5 and 51 deg) and crystalline peaks (for (111), (220) and (311) planes).

Table XIII. Deposition conditions for IACS Samples

Sample No.	Silane (sccm)	Argon (sccm)	Power (mW/cm^2)	Pressure (Torr)	Temp (^0C)
PLA70	5	95	82	0.2	250
PLA71	5	95	163	0.2	250
PLA72	5	95	109	0.2	250
PLA73	5	95	285	0.2	250
PLA74	1.5	98.5	82	0.2	250
PLA75	1.5	98.5	54	0.2	250
PLA76	10	90	27	0.2	250
PLA77	10	90	82	0.2	250
PLA78	10	90	163	0.2	250
PLA79	10	90	245	0.2	250
PLA80	5	95	33	0.2	250
PLA81	5	95	27	0.2	250

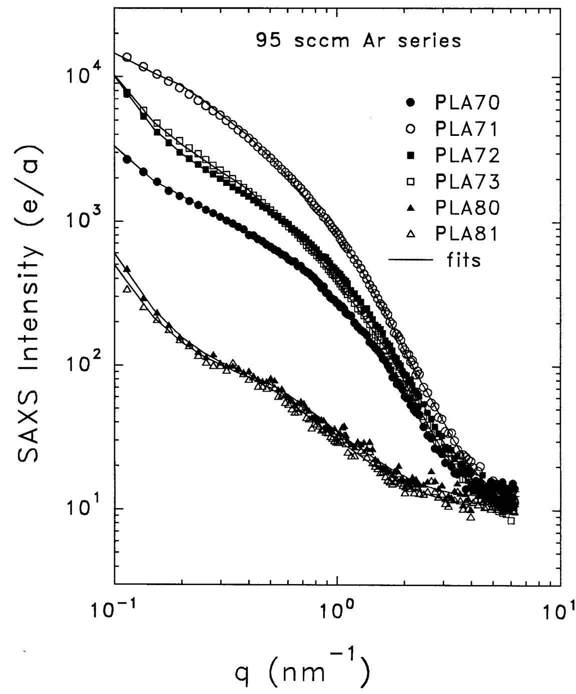

Fig. 36. SAXS from a-Si:H prepared at 95% Ar dilution at different plasma powers.

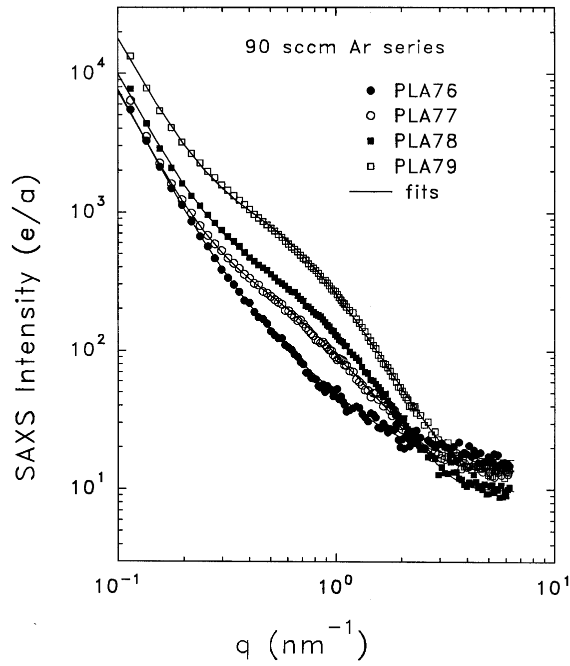

Fig. 37. SAXS from a-Si:H films prepared with 90% Ar dilution at different plasma powers.

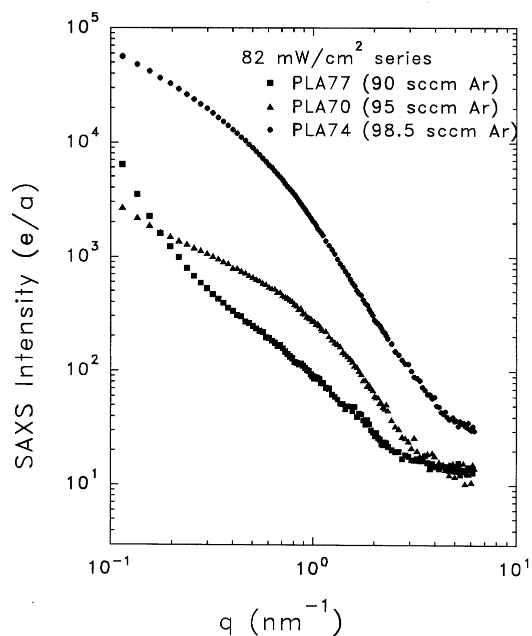

Fig. 38. Comparison of SAXS from Si:H prepared at different Ar dilutions but with the same plasma power.

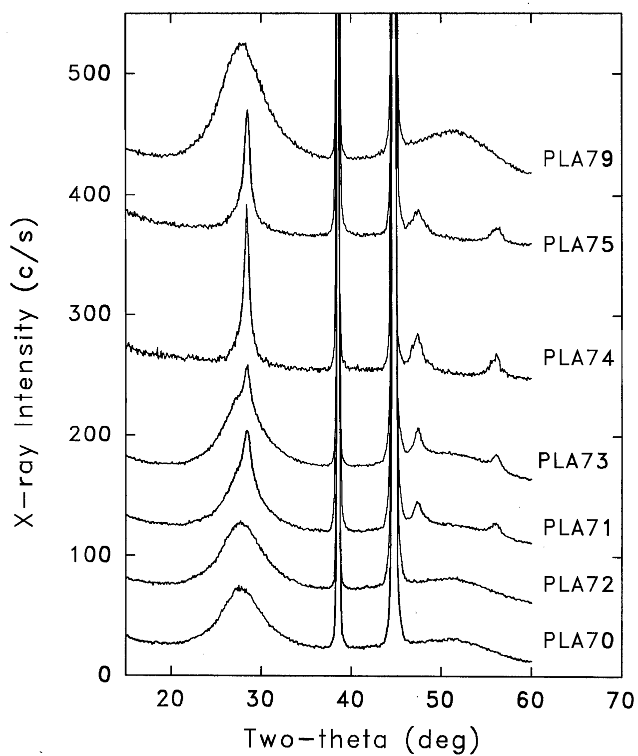

Fig. 39. XRD patterns from several Si:H films prepared by Ar-dilution showing different amounts of microcrystallinity. The strong peaks going off-scale in are due to the Al-foil substrate.

The table below summarizes the results of the SAXS and XRD measurements and analyses. Q_N is the integrated SAXS due to nanostructural features. F is the volume fraction of voids *assuming* all of Q_N is due to this type of feature. For the samples containing microcrystallinity, there may be additional scattering due to the contrast between the microcystals and the amorphous matrix. A is the Porod slope and is a measure of larger-scale features (>10 nm) that could be related to surface roughness or internal features. I_D is the q-independent diffuse scattering (typically proportional to H content but also related to SiH versus SiH_2 bonding). <D> is the average diameter of the distribution of spheres used to fit the data. NM signifies "not measured".

Table XIV. Quantitative SAXS and XRD results from Ar-diluted a-Si:H

Sample	Thickness via x-rays (μm)	Q_N (10^{23} eu/cm^3)	F (vol.%)	A (eu/nm^3)	I_D (eu)	<D> (nm)	XRD
PLA70	1.9	13.1	0.77	1.9	13	3.9	100% amorph
PLA71	1.8	62.3	3.8	4.5	9	5.2	Partly μc (24%)
PLA72	2.1	22.2	1.3	8	9.5	3.6	100% amorph
PLA73	3.0	20.4	1.2	7.5	9.5	4.3	Partly μc (17%)
PLA74	0.9	137	8.8	20	25	6.3	Strongly μc
PLA75	0.6	169	11	30	30	5.8	Strongly μc
PLA76	2.3	1.63	0.10	7.5	16	2.7	NM
PLA77	4.6	3.54	0.21	7.2	13.5	3.5	NM
PLA78	5.7	5.33	0.31	9.5	9.5	3.6	NM
PLA79	4.6	11.1	0.65	17	13	3.9	100% amorph
PLA80	3.7	1.10	0.064	0.5	12.5	3.6	NM
PLA81	4.9	1.01	0.060	0.4	11	3.8	NM

The formation of microcrystalline material and increases in void fractions can be clearly correlated with the deposition conditions. The transition from amorphous to microcrystalline material with increasing Ar dilution is analogous to that with H dilution. The results can be explained on the basis of bombardment of the growth surface by excited Ar atoms from the plasma. The latter were detected by optical emission spectroscopy. Further details and correlations with FTIR and Raman data are presented in ref. 54.

4. REFERENCES

1. D.L. Williamson, Mater. Res. Soc. Symp. Proc. **377**, 251 (1995) and references therein.
2. S. Guha, J. Yang, S.J. Jones, Yan Chen, and D.L. Williamson, Appl. Phys. Lett. **61**, 1444 (1992).
3. S. Guha, J. Yang, D.L. Williamson, Y. Lubianiker, J.D. Cohen, and A.H. Mahan, Appl. Phys. Lett. **74**, 1860 (1999).
4. D.L. Williamson, Mater. Res. Soc. Symp. Proc. **557**, 251 (1999) and references therein.
5. A.J. Leadbetter, A.A.M. Rashid, R.M. Richardson, A.F. Wright, and J.C. Knights, Solid State Commun. **33**, 973 (1980).
6. T.A. Postol, C.M. Falco, R.T. Kampwirth, I.K. Schuller, and W.B. Yelon, Phys. Rev. Lett. **45**, 648 (1980).
7. A.J. Leadbetter, A.A.M. Rashid, N. Colenutt, A.F. Wright, and J.C. Knights, Solid State Commun. **38**, 957 (1981).
8. R. Bellissent, A. Chenevas-Paule, and M. Roth, J. Non-Cryst. Solids **59&60**, 229 (1983); Physica B **117&118**, 941 (1983).
9. A. Chenevas-Paule, R. Bellissent, M. Roth, and J.I. Pankove, J. Non-Cryst. Solids **77&78**, 373 (1985).
10. C.A. Guy, A.F. Wright, R.N. Sinclair, R.J. Stewart, and F. Jansen, J. Non-Cryst. Solids **196**, 260 (1996).
11. T.P. Russel, P. Lambooy, J.C. Barker, P. Gallagher, S.K. Satija, G.J. Kellogg, and A.M. Mayes, Macromolecules **28**, 787 (1995).
12. D.L. Ho, R.M. Briber, R.L. Jones, S.K. Kumar, and T.P. Russel, Macromolecules **31**, 9247 (1998).
13. L.A. Feigin and D.I. Svergun, *Structure Analysis by Small-Angle X-ray and Neutron Scattering* (Plenum, New York, 1987).
14. D.W.M. Marr, M. Wartenberg, K.B. Schwatz, M.M. Agamalian, and G.D. Wignall, Macromolecules **30**, 2120 (1997).
15. A. Menelle, J. Non-Cryst. Solids **97&98**, 337 (1987).
16. R. Bellissent, in *Amorphous Silicon and Related Materials*, ed. H. Fritzche (World Scientific, 1988) p.93.
17. J. Yang, A. Banerjee, and S. Guha, Appl. Phys. Lett. **70**, 2975 (1997).

18. Q. Wang, E. Iwaniczko, Y. Xu, B.P. Nelson, and A.H. Mahan, Mater. Res. Soc. Symp. Proc. **557**, 163 (1999).
19. P. Roca i Cabarrocas, S. Hamma, S.N. Sharma, G. Viera, E. Bertran, and J. Costa, J. Non-Cryst. Solids **227-230**, 871 (1998).
20. C.J. Glinka, J.G. Barker, B. Hammouda, S. Krueger, J.J. Moyer, and W.J. Orts, J. Appl. Cryst. **31**, 430 (1998).
21. D.L. Williamson, D.W.M. Marr, B.P. Nelson, E. Iwaniczko, J. Yang, B. Yan, and S. Guha, Mat. Res. Soc. Symp. Proc. **609**, A16.2 (2001).
22. H. Fritzsche, Mater. Res. Soc. Symp. Proc. **467**, 19 (1997), and references therein.
23. A.A. Langford, M.L. Fleet, B.P. Nelson, W.A. Lanford, and N. Maley, Phys. Rev. **B45**, 13367 (1992).
24. L.S. Sidhu, T Kosteski, S. Zukotynski, and N.P. Kherani, J. Appl. Phys. **85**, 2574 (1999).
25. V.F. Sears, Neutron News **3**, 26 (1992).
26. Y. Wu, J.T. Stephen, D.X. Han. J.M. Rutland, R.S. Crandall, and A.H. Mahan, Phys. Rev. **B77**, 2049 (1996).
27. J. Baugh and D. Han, Mat. Res. Symp. Proc. **664**, A19.1 (2002).
28. D.L. Williamson, Y. Xu, and B.P. Nelson, in NCPV Photovoltaics Program Review, Proceedings of the 15th Conference, AIP Conf. Proc. **462**, edited by M. Al-Jassim, J.P. Thornton, and J.M. Gee (AIP, Woodbury, NY, 1999) p. 272.
29. Q. Wang, H. Antoniadis, and E.A. Schiff, Mat. Res. Soc. Symp. Proc. **258**, 881 (1992).
30. K. Lord, Yan, J.Yang, and S.Guha, preprint, submitted to Appl. Phys. Lett. (2001).
31. A.H. Mahan, J. Yang, S. Guha, and D.L. Williamson, Phys. Rev. **B61**, 1677 (2000).
32. A.H. Mahan, W. Beyer, D.L. Williamson, Y. Yang, and S. Guha, Phil. Mag. Lett. **80**, 647 (2000).
33. G. Yue, D. Han, D.L. Williamson, J. Yang, K. Lord, and S. Guha, Appl. Phys. Lett. **77**, 3185 (2000).
34. S.J. Jones, D.L. Williamson, T. Liu, X. Deng, and M. Izu, Mat. Res. Soc. Symp. Proc. **609**, A7.4 (2001).
35. S.J. Jones, R. Crucet, X. Deng, J. Doehler, R. Kopf, A. Myatt, D.V. Tsu, and M. Izu, Mat. Res. Soc. Symp. Proc. **557**, 567 (1999).

36. S.J. Jones, R. Crucet, X. Deng, D.L. Williamson, and M. Izu, Mat. Res. Soc. Symp. Proc. **609**, A4.5 (2001).
37. S.J. Jones, D.L. Williamson, T. Liu, X. Deng, and M. Izu, Mat. Res. Soc. Symp. Proc. **609**, A7.4 (2001).
38. B.P. Nelson, Y. Xu, A.H. Mahan, D.L. Williamson, and R.S. Crandall, Mat. Res. Soc. Symp. Proc. **609**, A22.8 (2001).
39. A.H. Mahan, Y. Xu, D.L. Williamson, W. Beyer, J.D. Perkins, M. Vanacek, L.M. Gedvillas, And B.P. Nelson, J. Appl. Phys. (2001, in press).
40. A.H. Mahan, Y. Xu, E. Iwaniczko, B.P. Nelson, Q. Wang, and D.L. Williamson, J. Non-Cryst. Solids (2001, in press).
41. G. Goerigk and D.L. Williamson, J. Non-Cryst. Solids **281**, 181 (2001).
42. G. Goerigk and D.L. Williamson, Solid State Commun. **108**, 419 (1998).
43. G. Goerigk and D.L. Williamson, J. Appl. Phys. **90** (Dec. 2001, in press).
44. S.J. Jones, A.B. Swartzlander-Franz, Y. Chen, and D.L. Williamson, Mat. Res. Soc. Symp. Proc. **297**, 1049 (1993).
45. O. Nast and S.R. Wenham, J. Appl. Phys. **88**, 124 (2000).
46. P. Roca i Cabarrocas, S. Hamma, S.N. Sharma, G. Viera, E. Bertran, and J. Costa, J. Non-Cryst. Solids **227-230**, 871 (1998).
47. J. Costa, P. Roura. P. Roca i Cabarrocas, G. Viera, and E. Bertan, Mat. Res. Soc. Symp. Proc. **507**, 499 (1998).
48. C. Longeaud, J.P. Kleider, M. Gauthier, R. Bruggemann, Y. Poissant, and P. Roca i Cabarrocas, Mat. Res. Soc. Symp. Proc. **557**, 501 (1999).
49. Y. Chen, Ph.D. Thesis, Colorado School of Mines (1994).
50. U.K. Das, A.R. Middya, J.K. Rath, C. Longeaud, D.L. Williamson, and P. Chaudhuri, J. Non-Cryst. Solids **276**, 46 (2000).
51. U.K. Das, J.K. Rath, D.L. Williamson, and P. Chaudhuri, Jpn. J. Appl. Phys.(Part 1) **39**, 2530 (2000).
52. P.P. Ray, P. Chaudhuri, and P. Chatterjee, ERMS Spring Meeting 2001, Strasbourg, France (to be published in Thin Solid Films).
53. U.K. Das, P. Chaudhuri, and S.T. Kshirsagar, J. Appl. Phys. **80**, 5389 (1996).

54. P. P. Ray, N.D. Gupta, P. Chaudhuri, D.L. Williamson, S. Vignoli, and C. Longeaud, J. Non-Cryst. Solids (2001, in press).

REPORT DOCUMENTATION PAGE

Form Approved
OMB NO. 0704-0188

Public reporting burden for this collection of information is estimated to average 1 hour per response, including the time for reviewing instructions, searching existing data sources, gathering and maintaining the data needed, and completing and reviewing the collection of information. Send comments regarding this burden estimate or any other aspect of this collection of information, including suggestions for reducing this burden, to Washington Headquarters Services, Directorate for Information Operations and Reports, 1215 Jefferson Davis Highway, Suite 1204, Arlington, VA 22202-4302, and to the Office of Management and Budget, Paperwork Reduction Project (0704-0188), Washington, DC 20503.

1. AGENCY USE ONLY (Leave blank)	2. REPORT DATE March 2002	3. REPORT TYPE AND DATES COVERED Final Technical Progress Report 22 May 1998 – 15 October 2001

4. TITLE AND SUBTITLE Nanostructure of a-Si:H and Related Alloys by Small-Angle Scattering of Neutrons and X-Rays, Final Technical Progress Report, 22 May 1998 – 15 October 2001 6. AUTHOR(S) D. L. Williamson	5. FUNDING NUMBERS CF: XAK-8-17619-31 PVP25001
7. PERFORMING ORGANIZATION NAME(S) AND ADDRESS(ES) Colorado School of Mines Golden, Colorado 80401	8. PERFORMING ORGANIZATION REPORT NUMBER
9. SPONSORING/MONITORING AGENCY NAME(S) AND ADDRESS(ES) National Renewable Energy Laboratory 1617 Cole Blvd. Golden, CO 80401-3393	10. SPONSORING/MONITORING AGENCY REPORT NUMBER NREL/SR-520-31908

11. SUPPLEMENTARY NOTES
NREL Technical Monitor: Bolko von Roedern

12a. DISTRIBUTION/AVAILABILITY STATEMENT National Technical Information Service U.S. Department of Commerce 5285 Port Royal Road Springfield, VA 22161	12b. DISTRIBUTION CODE

13. ABSTRACT *(Maximum 200 words)* This report describes work performed to provide details of the microstructure in high-quality hydrogenated amorphous and microcrystalline silicon and related alloys on the nanometer size scale. The materials studied were prepared by current state-of-the-art deposition methods as well as by new and emerging deposition techniques. The purpose is to establish the role of nanostructural features in controlling the opto-electronic and photovoltaic properties. The approach centered around the use of the uncommon technique of small-angle scattering of both x-rays (SAXS) and neutrons (SANS). SAXS has already been established as highly sensitive to microvoids and columnar-like microstructure. A major goal of this research was to establish the ability of SANS to detect hydrogen inhomogeneity in device-quality materials. This was demonstrated and new information on various materials have been provided. Conventional X-ray diffraction techniques were used to examine medium-range order and microcrystallinity, particularly near the boundary between amorphous and microcrystalline material.

SUBJECT TERMS: PV; small-angle neutron scattering; small-angle X-ray scattering; amorphous silicon solar cell; microcrystallinity; polymorphous Si:H; a-SiGe:H	15. NUMBER OF PAGES 16. PRICE CODE

17. SECURITY CLASSIFICATION OF REPORT	18. SECURITY CLASSIFICATION OF THIS PAGE	19. SECURITY CLASSIFICATION OF ABSTRACT	20. LIMITATION OF ABSTRACT
Unclassified	Unclassified	Unclassified	UL